DEVELOPMENT OF A NOVEL SEISMIC FORCE RESISTING SYSTEM: CONTROLLED ROCKING MASONRY WALLS WITH ENERGY DISSIPATION ACCESSIBLE CONSTRUCTED ATOP A STEEL BASE

DEVELOPMENT OF A NOVEL SEISMIC FORCE RESISTING SYSTEM: CONTROLLED ROCKING MASONRY WALLS WITH ENERGY DISSIPATION ACCESSIBLE CONSTRUCTED ATOP A STEEL BASE

BY

MATTHEW ALLEN EAST, B.Eng.

A THESIS

SUBMITTED TO THE DEPARTMENT OF CIVIL ENGINEERING

AND THE SCHOOL OF GRADUATE STUDIES

OF MCMASTER UNIVERSITY

IN PARTIAL FULFILMENT OF THE REQUIREMENTS

FOR THE DEGREE OF

DOCTOR OF PHILOSOPHY

Doctor of Philosophy (2022) McMaster University

(Civil Engineering) Hamilton, Ontario, Canada

TITLE:	DEVELOPMENT OF A NOVEL SEISMIC FORCE RESISTING SYSTEM: CONTROLLED ROCKING MASONRY WALLS WITH ENERGY DISSIPATION ACCESSIBLE CONSTRUCTED ATOP A STEEL BASE
AUTHOR:	Matthew Allen East B.Eng. & Mgmt. (Civil Engineering), McMaster University, Hamilton, Canada
SUPERVISOR:	Lydell Wiebe Mohamed Ezzeldin
NUMBER OF PAGES:	xix, 197

Lay Abstract

Modern buildings are designed to withstand earthquakes without collapsing by allowing for damage in specific parts of the structure that will not lead to collapse or loss of life. This design philosophy is effective at ensuring safety, but it allows damage even to high-importance buildings like schools and hospitals, and it can result in extensive economic losses where many buildings need to be repaired or demolished following an earthquake. This thesis works toward developing a novel structural system that will experience significantly less damage during an earthquake and be easily repairable. In this respect, the thesis first evaluates a new device that can be installed easily at the base of a wall designed to concentrate the damage and control the response of the wall during an earthquake. The thesis then develops a numerical model to predict the response of the new wall system, in order to optimize the design and ensure that low damage performance is obtained. Finally, a group of these novel walls are constructed and tested in a laboratory in order to demonstrate the expected performance.

Abstract

Conventional seismic design practices for reinforced masonry shear walls rely on ductility within the system, typically in the form of yielding of bonded reinforcement within the wall. While this is effective at dissipating energy, it comes at the expense of significant damage in the plastic hinge region, as well as substantial residual deformations. This results in costly repairs being required following a seismic event, and in some cases demolition.

Controlled rocking systems have been garnering considerable attention as a design approach that can mitigate these shortcomings. In a controlled rocking wall system, the wall is permitted to uplift from the foundation, reducing the lateral stiffness of the wall and producing a nonlinear response without relying on ductility within the wall. This response is typically controlled with the use of unbonded post-tensioning (PT) tendons within the wall to provide a restoring force to the system and eliminate residual drifts. These systems are considered favorable for resilient design as the repair costs and the corresponding service shutdowns are minimized.

In application to masonry systems specifically, the PT tendons impose additional compressive stresses on the rocking toes, resulting in damage in these regions of the wall. In addition to this, the construction process of a masonry wall with unbonded PT can have challenging detailing considerations. Meanwhile, previous studies have also indicated that controlled rocking masonry systems (CRMWs) have relatively low inherent damping. Recent studies have shown promising results by testing CRMWs that rely on gravity loading for a self-centering response, omitting PT, and

introducing energy dissipation inside the walls. However, as the devices are within the wall, they are difficult or impossible to repair if needed following a seismic event.

In this respect, the current thesis begins with an investigation of an externally mounted, replaceable energy dissipation device in the form of a flexural yielding cantilever arm. Experimental tests of the devices are analyzed, and the experimental results are used together with numerical modelling of the devices to develop design equations. Following this, a numerical study is conducted to evaluate the effectiveness of the proposed flexural arm devices within a new CRMW system. A new damage index for reinforced masonry walls is introduced and then applied to compare the effectiveness of innovative CRMW design alternatives. This work ultimately proposes a system that has Energy dissipation Accessible, constructed atop a Steel rocking base (EASt-CRMW), which has a desirable self-centering response relying on gravity loads, with the flexural arms adding supplemental energy dissipation to the system.

Building on these developments, two large-scale experimental studies on EASt-CRMWs are presented. The first study reports the results of six EASt-CRMWs with various parameters. The results display a highly favorable hysteretic response, able to withstand drifts as high as 5% with negligible damage and residual drifts of less than 0.1%. The study then proposes two procedures to predict the monotonic force-displacement response of the EASt-CRMW system. The second experimental study investigates the performance of two additional EASt-CRMWs in which the flexural yielding energy dissipation devices were replaced and the walls retested, showing that the system can produce nearly identical results upon

retesting. The study then validates the previously discussed numerical modelling approach for the further application of EASt-CRMWs, indicating that the model developed is indeed capable of capturing the actual response of the system and that the damage index accurately predicts the location and severity of damage within EASt-CRMWs.

Declaration of Academic Achievement

This thesis has been prepared to the requirements of a sandwich thesis format as stipulated by the School of Graduate Studies at McMaster Unirviersy. In accordance with the requirements of the manuscript-based sandwich thesis format, Chapters 2 through 5 have been either published, or submitted to be considered for publication in peer-reviewed journals. Mr. Jeff Li designed and conducted the experimental testing presented in Chapter 2, presenting the results in his MASc thesis. Dr. Ahmed Yassin assisted with the design and construction of the experimental setup in the lab outlined in Chapter 4. The conceptual development of EASt-CRMWs, all numerical analysis, and the design and implementation of the wall testing program that is presented in this thesis were all carried out solely by the author under the primary supervision, guidance, and review of Dr. Mohamed Ezzeldin and Dr. Lydell Wiebe. Information presented from outside sources, which has been used towards analysis or discussion, has been cited where appropriate. The manuscripts containing the chapters of this thesis have been co-authored and their status as of August 2022 is as follows:

Chapter 2: Development of a Flexural Yielding Energy Dissipation Device for Controlled Rocking Systems

Authors: Matthew East, Jeff Li, Mohamed Ezzeldin and Lydell Wiebe

Full Citation:

East, M., Li, J., Ezzeldin, M., Wiebe, L., In Press. "Development of a Flexural Yielding Energy Dissipation Device for Controlled Rocking Systems." *Journal of Structural Engineering.* https://doi.org/10.1061/(ASCE)ST.1943-541X.0003461.

Chapter 3: Strategies to Reduce and Quantify Seismic Damage in Controlled Rocking Masonry Walls

Authors: Matthew East, Mohamed Ezzeldin and Lydell Wiebe

Under review by ASCE Journal of Structural Engineering, submitted in July 2022.

Chapter 4: Development of Controlled Rocking Masonry Walls with Energy Dissipation Accessible in a Steel Base

Authors: Matthew East, Ahmed Yassin, Mohamed Ezzeldin, Lydell Wiebe

Under review by ASCE Journal of Structural Engineering, submitted in August 2022.

Chapter 5: Repairability and Damage Assessment of Controlled Rocking Masonry Walls with Energy Dissipation Accessible in a Steel Base

Authors: Matthew East, Mohamed Ezzeldin, Lydell Wiebe

Under review by ASCE Journal of Structural Engineering, submitted in August 2022.

Acknowledgements

First, I would like to express my appreciation and sincere gratitude to my co-supervisors, Dr. Lydell Wiebe and Dr. Mohamed Ezzeldin. The guidance, encouragement, patience, and support they provided dramatically impacted the overall quality of the thesis. I would also like to thank my supervisory committee members, Dr. Wael El-Dakhakhni and Dr. Cancan Yang for their insights during our meetings.

The lab work I conducted would not have been possible without the help of Paul Heerema and Kent Wheeler. Not only did they teach me the skills I needed to carry out all my experimental work, but they also both made the experience more fun and enjoyable than I could have imagined it being (even throughout a pandemic!). If not for Sam Richardson, Kelly de Chastelain Finnigan, Keegan Amy, Brenden Lie and Madona Gouda helping me in the lab over the summers, I would still be there today testing, so I owe them all a great deal of thanks. I would also like to thank Dr. Bennett Banting of the Canada Masonry Design Center (CMDC) for providing valuable comments regarding the masonry industry in Canada, and for the expert masons the CMDC provided.

Beyond the direct contributors to this work, I would also like to thank the many other people who indirectly contributed to this work, often unknowingly. Paul Steneker and Kevin McNamara were endlessly entertaining and supportive friends, and incredibly helpful examples to follow. Mariano Colicchio, Ricky Darlington, Trevor Reade, Mike Sucharda, Dan Lee Kim and Alex Dufault served as refreshing reminders that there is a

whole world to structural engineering that is not remotely related to controlled rocking masonry walls, keeping my research grounded in practicality towards the industry we are all devoting our careers towards. My parents were relentless with their kind words of support, even through the toughest times. Last, but certainly not least, I would like to extend my deep and sincere gratitude to Rachel Boyd. She was by my side through so many highs and lows over the years, and I can be confident in saying that I would not be writing this had it not been for her overwhelming love, support, and kindness.

Contents

List of Figures

List of Tables

Chapter 1

Introduction

1.1 Background

Masonry is one of the oldest construction materials and is still used extensively in low- and mid-rise structures for residential, commercial, and industrial applications. Modern seismic design requirements have significantly impacted the practicality of masonry buildings because they are considerably less ductile than comparable reinforced concrete or steel structures and thus, more at risk during seismic events.

Modern structures that are designed with the most recent building codes are often expected to sustain damage during severe seismic events. With this in mind, the design philosophy in practice is such that these structures are expected to sustain the safety of the occupants, despite being subjected to serious damage. The conventional approach for lateral force-resisting systems relies on dissipating energy through inelastic behaviour. To achieve this, special detailing is needed to meet strict codified ductility requirements. This approach suggests also that structures currently experience extensive damage during large earthquakes, resulting in expensive repairs, significant business downtime, and in some extreme cases complete building demolition.

A design approach that has been recently investigated to mitigate seismic risks is the concept of self-centering structures with a rocking mode as the

primary mode of deformation, rather than shear and flexural deformations. This design approach reduces the reliance on ductility while also adding the benefit of minimal drifts, as the structural system returns to its original position following a seismic event, unlike conventional ductility-based designs. The source of nonlinearity in the system arises when the base overturning moment caused by the applied lateral loads exceeds the decompression moment capacity, causing the wall to uplift and creating a single crack at the wall-foundation interface.

An early study on controlled rocking reinforced concrete walls was conducted as part of the Precast Seismic Structural Systems (PRESSS) initiative (Priestley 1991). This testing showed that this method of self centering was highly effective for use in concrete walls, with follow up studies by Hassanli et al. (2016a) further supporting the effectiveness of the system.

In application to masonry walls in particular, research studies have primarily investigated the use of unbonded post-tensioning tendons installed within the cells of the masonry units within ducts such that the grout does not interfere with the post-tensioning tendons (Laursen and Ingham, 2001, 2004a, 2004b; Rosemboom and Kowalsky, 2004; Wight et al. 2006; ElGawady et al. 2011; Ryu et al. 2014, Gheni et al. 2015; Hassanli et al. 2016b). This method of controlling the response was effective at producing a stable hysteretic response with very low residual drifts; however, the installation of the post-tensioning tendons complicates the construction process and ultimately can lead to poor performance in terms of the wall deformation capacity (Rosemboom and Kowalsky, 2004). The additional compressive stresses in the rocking toe of the wall led to damage due to the brittle nature of masonry in comparison to other materials, such as steel or concrete.

Furthermore, additional studies have shown that controlled rocking masonry systems have low inherent damping compared to conventional masonry systems with fixed bases (Hassanli et al. 2017).

Various energy dissipation devices have been developed for controlled rocking systems in general, with varying applicability to masonry systems in particular. Laursen and Ingham (2004), as well as Restrepo and Rahman (2007) embedded axial yielding steel bars within walls, anchored at the base. These studies demonstrated that the additional energy dissipation performed well to produce a flag-shaped hysteretic response characteristic of a controlled rocking system; however, due to responding in axial tension, they were prone to fracture at high displacement demands. Toranzo (2002) investigated the use of steel cantilever arms in controlled rocking walls to achieve a higher displacement capacity in order to match the displacement demands of controlled rocking masonry systems; however, the study proposed limited guidance on the design and performance of the device itself within the wall system. Related research efforts on similar cantilevered energy dissipators (e.g., steel slit dampers, butterfly fuses, and comb-teeth dampers) have demonstrated that a favorable, uniform distribution of yielding can be obtained from cantilevered flexural energy dissipation devices (Chan and Albermani, 2008; Ma et al., 2010; Garivani et al., 2016). While effective in application to controlled rocking steel braced frames (Deierlein et al., 2011), these devices were not applicable to masonry systems due to space constraints at the base of the wall. As such, further investigation into a flexural yielding energy dissipation device with corresponding design guidelines for practical applications to controlled rocking masonry systems is still needed.

Previous studies also reported the increased compressive stress demands on the rocking toes when dead and live loads are fully considered in addition to post-tensioning in controlled rocking masonry walls (CRMWs). One strategy to address this was investigated in a study by ElGawady *et al.* (2011) in which various materials of the rocking wall interface such as steel plates, rubber pads or pieces of wood were tested. The study demonstrated that a substantial amount of energy can be absorbed during a dynamic response when rubber pads are used. An alternative method for reducing compressive demands at the rocking toe was investigated by Yassin et al. (2022), in which CRMWs without PT were tested. A total of seven walls with embedded axial yielding energy dissipation devices were tested in the study. The walls performed well, where a stable hysteretic response was observed and a substantial amount of energy was dissipated. As there were still considerable compressive stresses on the rocking toes, and therefore, the damage was still observed within the lower courses of the walls. The study also indicated challenges in detailing and construction of the axial yielding energy dissipation devices inside the wall. As the devices relied on axial yielding to dissipate energy, they were unable to withstand sufficient deformation without failing, similar to the results reported by Laursen and Ingham (2004) and Restrepo and Rahman (2007). This limited the ultimate displacements the walls were able to reach, and also led to issues surrounding repairs, as the buckled or fractured energy dissipation devices were embedded within the wall, inaccessible. Stoppers are also required at the wall ends to prevent sliding at the rocking interface, which can lead to architectural issues with protrusions at the base of the walls. As such, a device that can resist the base shear of the system (eliminating the need for stoppers) while also having appropriate deformation capacity is needed. This device must also be

externally mounted (without substantially extending beyond the footprint of the wall for architectural reasons) and replaceable for practical implementation of a CRMW system.

In addition to experimentally investigating CRMWs, Laursen and Ingham (2004) developed and validated a numerical model using DRAIN-2DX (Prakash et al. 1993). The model contained fibre elements, with the result of simplifying the analysis to a single degree of freedom (SDOF) equivalent model (Laursen and Ingham, 2004). This modelling approach vastly underestimated the experimental shear forces by a factor of 2.1 to 2.6 and also was not able to capture the corresponding failure modes, particularly those of compression rocking toe failures at high drift ratios. Recently, Hassanli et al. (2017) developed a detailed finite element model using LS-DYNA (LSTC, 1978) to conduct a parametric study on post-tensioned, controlled rocking masonry walls. Notably, this work focused on post-tensioning tendons as a primary factor to generate governing equations that can predict the overall response of post-tensioned CRMWs (PT-CRMWs). Neither of these models was developed to capture the response of CRMWs without PT. Even more recently, Yassin et al. (2020) developed a model of PT-CRMWs to assess their seismic collapse risk. Notably, the macro-model was unable to quantify response at a local level within the walls. None of these models were able to assess damage throughout a numerical simulation, indicating a need to develop a new modelling technique that can capture the response of the novel CRMW systems and compare them in terms of damage to one another.

1.2 Motivation

The main motivation for this research study is to present a new CRMW system that mitigates damage and introduces externally attached, easily replaceable energy dissipation devices while remaining within the wall footprint. The system proposed incorporates newly developed energy dissipation devices, accessible within a steel base (EASt-CRMW). Figure 1.1 demonstrates the idealized hysteretic response of the proposed EASt-CRMW system.

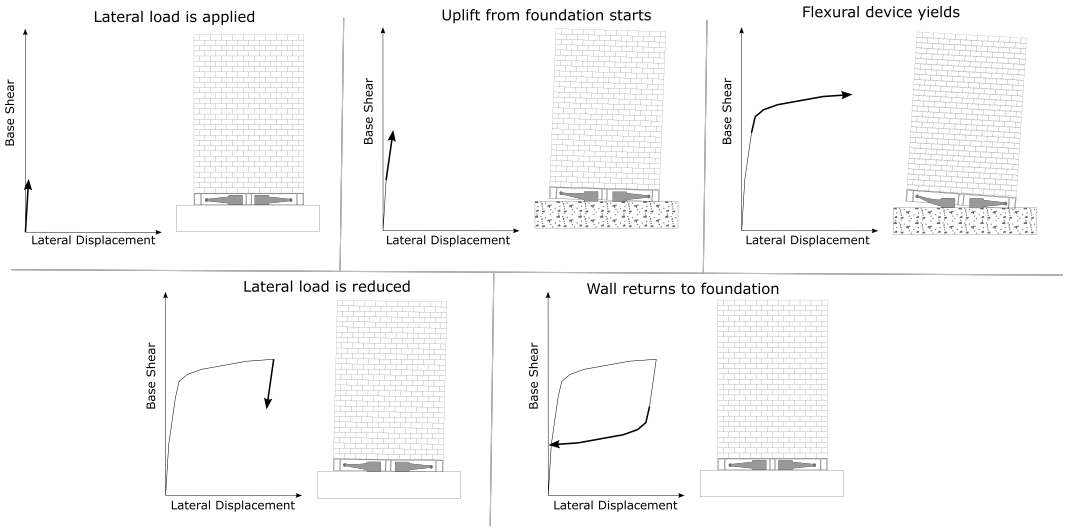

Figure 1.1: CRMW Force-Displacement Response

The study first evaluates the effectiveness of the new energy dissipation devices, and their ability to withstand the base sliding effects of the wall, while maintaining low damage and low residual drifts following seismic events. The study then provides design equations that can be used to practically design the devices for a CRMW.

Following this, a numerical model that addresses the gaps in previous

numerical modelling of CRMWs is essential to i) refine and optimize the overall design of the EASt-CRMW system; and ii) investigate ways to install the devices and evaluate their expected influence on the wall performance.

Ultimately, the EASt-CRMW system needs to be experimentally investigated, with consideration given to the practicality of the construction process, the performance of the walls relative to other CRMW systems, and the replaceability of the energy dissipation devices.

1.3 Research Objectives

Based on the literature review, and the research gaps identified above, the primary research goal is summarized with the following objectives:

1. Develop an energy dissipation device that is capable of being installed on the exterior of a CRMW, within the overall wall footprint, with the ability to be easily replaced following a seismic event.

2. Develop a numerical model capable of capturing the nonlinear static response of CRMWs with and without PT and ED devices, such that damage can be assessed between various design alternatives.

3. Develop a damage index that is cabable of predicting the location and severity of damage from numerical results.

4. Experimentally investigate the use of a CRMW system that omits PT, and utilizes a steel rocking base with externally mounted, replaceable energy dissipation devices at the base of the wall.

5. Develop a series of equations that can be used to predict the monotonic response of the novel CRMW system proposed.

6. Investigate the replaceability of the energy dissipation devices within walls and the repeated performance of the walls upon retesting.

1.4 Thesis Organization

This thesis consists of six chapters, starting with this introductory chapter, followed by four chapters covering the primary objectives of the research, and ending with a concluding chapter. The following is a brief description of each chapter.

Chapter 1 presents the motivation and objectives of the thesis, as well as some background information pertaining to the research program.

Chapter 2 contains the results of a study on developing externally mounted, flexural yielding energy dissipation devices for use in CRMW systems (Research Objective 1). The study includes experimental tests of 14 flexural arms in strong-axis bending, with and without axial loading to represent the base shear of the wall (i.e., this experimental work was conducted by another student, and is integrated into the chapter but not a contribution to this thesis). The chapter then develops a numerical model capable of capturing the response of the devices, such that additional future studies can incorporate the model into a larger model of CRMWs to predict the response of CRMWs with the proposed flexural yielding energy dissipation devices. Finally, design equations are proposed and validated for the devices to be used in design methodologies for CRMWs.

Chapter 3 presents the results of a numerical study aimed at quantifying

and minimizing damage in CRMW systems (Research Objectives 2 and 3). The chapter first examines the use of multi-layer shell elements to capture the response of previous experimental studies of CRMWs with and without post-tensioning. Following the development and validation of the model, a damage index for reinforced masonry is proposed and validated against available experimental data. Finally, a suite of 20 CRMWs is designed using various strategies to reduce damage and enhance the performance of CRMWs when subjected to a static, cyclic analysis. This results in a system incorporating accessible energy dissipation, within a steel base (EASt-CRMW) being proposed (Research Objective 4).

Chapter 4 experimentally investigates the EASt-CRMW system proposed in Chapter 3 (Research Objective 4). The construction process, material properties, loading protocol, instrumentation and energy dissipation are discussed in detail. Following the description of the experimental program, the results are discussed and evaluated in terms of the force-displacement response, damage sequence, self-centering, and energy dissipation. Following this, two procedures to predict the monotonic response of the walls are proposed (Research Objective 5). The first is an iterative procedure, while the second procedure utilizes an idealized stress block assumption to simplify the calculation and reduce the need for iterations in the solution.

Chapter 5 presents the results of a study on testing two additional EASt-CRMWs, with a focus on the performance after retesting the walls following replacing their energy dissipation devices. The damage response, hysteretic behaviour and self-centering capacity are evaluated and compared to the first wall test (Research Objective 6). Following this, the numerical model presented in Chapter 3 is validated against tests of the EASt-CRMW

system (Research Objective 2), with the damage index being further validated (Research Objective 3).

Chapter 6 provides a summary of the research, drawing out the main implications of the work and key findings that answer the primary research objectives as well as recommendations for future research studies.

Although each chapter presents a standalone journal manuscript, Chapters 2, 3, 4 and 5 collectively outline a single, cohesive research program aimed at developing the EASt-CRMW seismic force resisting system. Nonetheless, for completeness of the standalone individual manuscripts, some overlap is unavoidable, particularly in the introductions provided, experimental testing methods, and description of numerical modelling techniques used.

1.5 References

Chan, R. W. K. and Albermani, F. 2008. "Experimental study of steel slit damper for passive energy dissipation." *Engineering Structures*, 30(4): 1058-1066.

Deierlein, G., Krawinkler, H., Ma, X., Eatherton, M., Hajjar, J., Takeuchi, T., Kasai, K., Midorikawa, M. (2011). "Earthquake resilient steel braced frames with controlled rocking and energy dissipating fuses." *Steel Construction*, 4(3): 171-175.

ElGawady, M. A., Ma, Q., Butterworth, J. W., and Ingham, J. 2011. "Effects of interface material on the performance of free rocking blocks." *Earthquake Engineering and Structural Dynamics*. 40(4): 375-392.

ElGawady, M. A., and Sha'lan, A. 2011. "Seismic behaviour of self-centering

precast segmental bridge bents." *ASCE Journal of Bridge Engineering*. 16(3): 328-339.

Garivani, S., Aghakouchak, A. A., and Shahbeyk, S. 2016. "Numerical and experimental study of comb-teeth metallic yielding dampers." *International Journal of Steel Structures*, 16(1): 177-196.

Gheni, A., ElGawady, M. A., and Myers, J. 2015. "Cyclic in-plane behaviour of unbonded post-tensioned masonry walls." *12th North American Masonry Conference*. Colorado, USA.

Hassanli, R., M. A. ElGawady, and J. E. Mills. 2016. "Experimental Investigation of In-Plane Cyclic Response of Unbonded Posttensioned Masonry Walls." *Journal of Structural Engineering*, 142 (5): 04015171. https://doi.org/10.1061/(asce)st.1943-541x.0001450.

Hassanli, R., M. A. ElGawady, and J. E. Mills. 2016a. "Force Displacement behaviour of unbonded post-tensioned concrete walls." *Engineering Structures*, 106:495-505

Hassanli, R., M. A. ElGawady, and J. E. Mills. 2017b. "In-plane flexural strength of unbonded post-tensioned concrete masonry walls." *Engineering Structures*. 136: 245-260. https://doi.org/10.1016/j.engstruct.2017.01.016.

Laursen, P. 2002. "Seismic analysis and design of post-tensioned concrete masonry walls." Doctoral Dissertation, University of Auckland.

Laursen, P. T., and J. M. Ingham. 2004. "Structural Testing of Large-Scale Posttensioned Concrete Masonry Walls." *Journal of Structural*

Engineering, 130 (10): 1497. https://doi.org/10.1061/(asce)0733-9445(2004)130:10(1497).

Livermore Software Technology Corporation, "LS DYNA." *LSTC*, 1978.

Ma, X., Borchers, E., Pena, A., Krawinkler, H., Billington, S., and Deierlein, G. G. 2010. "Design and behaviour of steel shear plates with openings as energy-dissipating fuses." *The John A. Blume Earthquake Engineering Center*, Report No.173.

Prakash, V., Powell, G. H., and Campbell, S. 1993. "DRAIN-2DX base program description and user guide." *University of California, Berkeley*, California.

Priestley, M. N. 1997. "Overview of presss research program," PCI journal, 36(4): 50-57.

Restrepo, J. I. and Rahman, A. 2007. "Seismic performance of self-centering structural walls incorporating energy dissipators." *Journal of Structural Engineering*, 133(11): 1560-1570.

Rosenboom, O. A., and M. J. Kowalsky. 2004. "Reversed In-Plane Cyclic Behavior of Posttensioned Clay Brick Masonry Walls." *Journal of Structural Engineering*, 130 (5): 787-798. https://doi.org/10.1061/(asce)0733-9445(2004)130:5(787).

Ryu, D. Wijeyewickrema, A. ElGawady, M. A., and Madurapperuma, M. 2014. "Effects of tendon spacing on in-plane behaviour of posttensioned masonry walls." *Journal of Structural Engineering*. 140(10): 1061.

Toranzo, L. A. 2002. "The use of rocking walls in confined masonry structures: a performance-based approach." *Doctoral Dissertation*, Department of Civil Engineering, University of Canterbury, New Zealand.

Wight, G. D. 2006. "Seismic performance of a post-tensioned concrete masonry wall system." *Doctoral Dissertation.* University of Auckland.

Yassin, A., Ezzeldin, M., Steele, T., and Wiebe, L. (2020). "Seismic collapse risk assessment of post-tensioned controlled rocking masonry walls." *Journal of Structural Engineering*, 146(5), 04020060-1-16.

Yassin, A., M. Ezzeldin, and L. Wiebe. 2022. "Experimental Assessment of Controlled Rocking Masonry Shear Walls without Post-tensioning." *Journal of Structural Engineering*, 148 (4): 1–14. https://doi.org/10.1061/(asce)st.1943-541x.0003307.

Chapter 2

Development of a Flexural Yielding Energy Dissipation Device for Controlled Rocking Systems

2.1 Abstract

Controlled rocking systems in a variety of materials have been demonstrated to be highly effective in resisting seismic forces. In a controlled rocking system, uplift of the wall or frame from the foundation is allowed in a way that can localize damage and minimize post-earthquake residual drifts. However, the limited inherent damping of the system can lead to excessive displacements. As such, energy dissipation devices have been developed and evaluated to add supplemental damping to the system. These devices have often been embedded within the wall system or have been otherwise unrepairable following seismic events. Therefore, the development of an easily replaceable energy dissipation device is expected to maintain the overall performance of controlled rocking systems, while also enhancing their post-earthquake repairability. In this respect, steel flexural yielding arms can

be an effective energy dissipation device for controlled rocking systems. In addition to adding supplemental energy dissipation to the system, the device can eliminate the need for using mechanical stoppers to prevent sliding if the devices are designed to withstand the expected sliding demands. As such, the objective of the current study is to experimentally and numerically investigate the behaviour of steel flexural yielding arms with and without axial load demands in order to propose practical design equations for implementation of these devices. Specifically, the study first presents a description of the experimental program, test setup, instrumentation, and results. Based on these experimental results, an OpenSees model is developed and validated to evaluate the performance of these devices for a wide range of geometrical configurations. Subsequently, new design equations that account for axial forces are proposed and verified against both experimental and numerical results. Finally, recommendations are presented for the further development of externally attached and replaceable flexural yielding arms for controlled rocking systems.

2.2 Introduction

The hysteretic response of a conventional concrete or masonry wall typically causes cracks to form in the tensile regions of the wall due to lateral loading, thus leading to damage. Alternatively, controlled rocking wall systems with vertical unbonded post-tensioning strands have been researched with success through the Precast Seismic Structural Systems project (PRESSS) (Priestley et al., 1999). These wall systems performed well by localizing damage only in the rocking toe region of the wall. Following the success of these studies,

several researchers have demonstrated that controlled rocking walls with energy dissipation devices (EDDs) and/or post-tensioning strands can be an effective and economic alternative to replace conventional walls (e.g., Rahman and Restrepo-Posada 2000; Toranzo, 2002; Holden et al. 2003; Toranzo et al., 2004; Laursen and Ingham, 2004; Perez et al. 2007; Hassanli et al. 2017; Kalliontzis et al. 2017; Yassin et al. 2020). This is mainly due to the unique ability of controlled rocking systems to uplift from their foundation when subjected to lateral loads. In general, a controlled rocking mechanism yields a seismic force-resisting system with high self-centering ability and low residual drifts, thus minimizing damage following seismic events. This is characterized by a desirable flag-shaped hysteretic response, as shown in Figure 2.1.

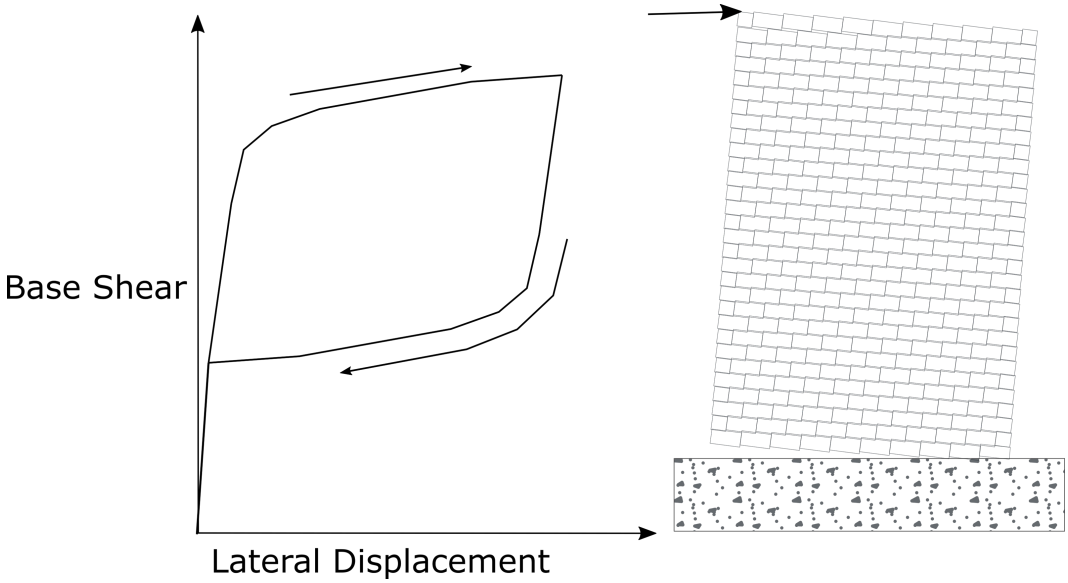

Figure 2.1: Hysteretic response of a controlled rocking system

Free rocking walls (i.e., without post-tensioning strands or EDDs) are associated with limited overturning moment resistance and hysteretic energy dissipation capacity. Conversely, controlled rocking systems use

post-tensioning strands and/or supplemental EDDs to control lateral drifts and minimize structural damage (Priestley et al., 1999; Holden et al., 2002; Laursen and Ingham, 2004; Toranzo et al., 2004; Restrepo and Rahman, 2007, Ponzo et al., 2017; Pampanin et al., 2019; Ponzo et al., 2019; Di Cesare et al., 2020; Granello et al., 2020). In response to a lateral load, the rocking is initiated when the moment demand exceeds the overturning moment resistance created due to gravity loads and any post-tensioning. During this stage (i.e., decompression), the dissipators start to engage due to the imposed displacement demand caused by the wall uplift. In this respect, the use of replaceable EDDs is favored for facilitating rapid recovery of seismic performance after an earthquake, thus complementing the enhanced performance that can be achieved when such rocking systems are adopted (Erochko et al. 2015; Zheng et al. 2020).

A limited number of devices have been investigated and adopted for rocking walls. A common example of EDDs for use in controlled rocking systems is steel axial yielding bars anchored at the base of the walls (Holden et al., 2002; Laursen and Ingham, 2004; Restrepo and Rahman, 2007). These axial yielding devices are typically made with reinforcement bars to ensure their yielding in a well-defined region; however, they are still prone to fractures at high displacement demands (Holden et al., 2002; Laursen and Ingham, 2004; Restrepo and Rahman, 2007). In general, relevant studies demonstrated that steel axial devices performed well to achieve a flag-shaped hysteretic response by adding supplemental energy dissipation to controlled rocking walls. However, due to the embedded nature of these devices, they cannot be assessed or replaced if severely damaged by a seismic event. To address this issue, Toranzo (2002) adopted an externally attached version in

the form of a device similar in concept to a miniature buckling restrained brace (BRB), but the device was unable to sustain the desired deformations without unintended buckling. This buckling led to an unpredictable response in the compression region due to the development of large friction forces between the body of the steel dissipator and the grout in the case (Toranzo, 2002). Other devices that have been used with success include friction energy dissipation devices (Wiebe et al. 2013), U-shaped flexural plate dampers (Pampinin, 2002; Iqbal et al., 2015) and various hysteretic and viscous energy dissipators (e.g. Kam et al. 2010, Tremblay et al. 2008, and Sarti et al. 2017).

Conversely, few studies have explored the viability of externally attached steel cantilever arms as EDDs in rocking walls (Toranzo, 2002; Toranzo et al., 2009). These devices aim to dissipate energy through strong-axis flexural yielding as the rocking structure lifts and imposes displacements on the cantilevered section. In these previous studies, two cantilever arm designs were proposed and validated under quasi-static cyclic loading and were then tested in rocking walls under dynamic loading (Toranzo, 2002). In addition to their accessibility and repairability following a seismic event, the experimental results showed that steel cantilever arms can achieve reliable performance with no complications. Specifically, the planar geometry of the cantilever arms makes them more suitable for space-constrained applications (Ma et al., 2010). The pure flexural yielding behaviour of such arms was also observed to be more reliable than that of steel axial yielding bars in medium to large displacement cycles, corresponding to 2-3% roof drift of rocking walls. However, the design requirements of these cantilever arms were not clearly outlined and no guidance was presented regarding the influence of key

geometrical parameters (e.g., length and aspect ratio) on the performance of such arms (Toranzo, 2002).

While limited research has been conducted on steel cantilever arms as EDDs, many studies have demonstrated the effect of different parameters on the performance of other flexural yielding steel energy dissipation devices with similar geometry (e.g., Chan and Albermani, 2008; Ma et al., 2010; Garivani et al., 2016). For example, steel slit dampers, comb-teeth dampers, and butterfly fuses were designed to yield uniformly through the configurations of triangular/rectangular/parabolic steel plates when subjected to strong-axis bending (Chan and Albermani, 2008; Ma et al., 2010; Garivani et al., 2016). However, these previous studies focused on in-plane assemblies of multiple smaller links, which may not be feasible in further space-constrained applications. Alternatively, added damping and stiffness (ADAS) and triangular-ADAS (TADAS) devices were designed to yield uniformly throughout the assemblies of X-shaped or triangular steel plates when subjected to weak-axis bending (Bergman and Goel, 1987; Xia and Hanson 1992; Aiken et al., 1993; Tsai et al., 1993; Eldin et al. 2017, Garivani et al., 2016; Saeedi et al., 2017). These previous studies have demonstrated that triangular-like configurations were superior to other configurations by facilitating a more uniform distribution of yielding, thus minimizing stress concentrations, although notably these devices relied on flexure about the weak axis (Kobori et al., 1992; Chan and Albermani, 2008; Ma et al., 2010). Previous studies have also produced promising results regarding EDDs for out-of-plane modes in masonry structures using LICORD seismic dissipators (D'Ayala and Paganoni, 2014; Giresini et al., 2021; Nochebuena-Mora et al., 2021).

Although several configurations of flexural devices have been studied in the past, there is still a lack of experimental and numerical data for the performance of simple tapered cantilever arms. In addition, since multiple studies have recommended that axial compression on flexural devices should be avoided by-design to prevent premature buckling, all previous studies did not include axial compression demands on their corresponding devices (Chan and Albermani, 2008; Ma et al., 2010; Garivani et al., 2016). As such, the main objective of the current study is to experimentally and numerically investigate the behaviour of externally attached flexural arms, designed specifically for newly constructed rocking walls, as shown in Figure 2.2, under simultaneous cyclic displacement and axial compression loadings that simulate seismic demands. Although these flexural arms are expected to be subjected to displacements in only one direction when adopted in controlled rocking walls as shown in Figure 2.2, the current study considered investigating the performance of such arms under cyclic displacement loading in two directions as this loading protocol facilitates their adoption in a wide range of structural engineering applications. As the forces that these devices experience in a wall system are expected to vary based on the installation, geometry and anticipated displacements, this study focuses conservatively on the worst-case scenario by simulating a maximum expected axial compression force on the flexural arms. The study first describes the experimental program, test apparatus, and test results for the tested devices. Following the experimental results, a numerical model is developed, validated and used to assess the performance of several flexural arms when different geometrical configurations are adopted. Finally, new design equations are proposed and verified using both experimental and numerical results.

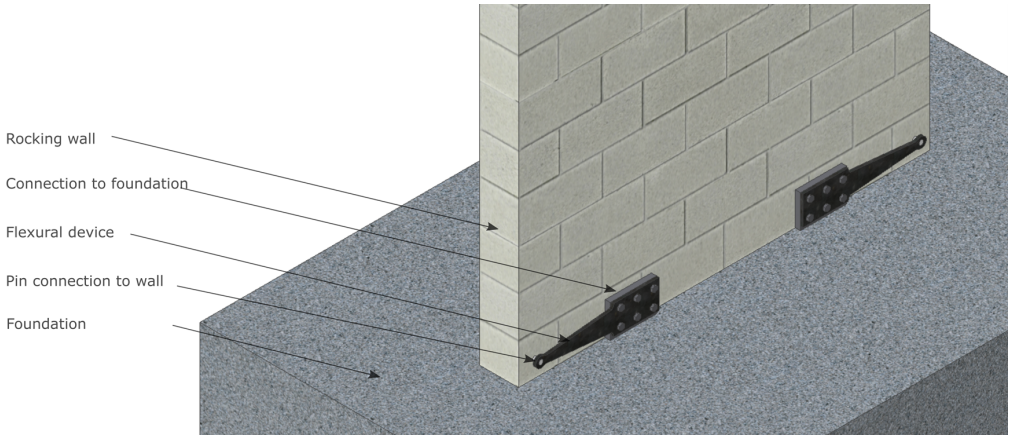

Figure 2.2: Flexural arms connected to a controlled rocking masonry wall

2.3 Experimental Program

2.3.1 Test Program Overview

As can be seen in Table 2.1, the test matrix aims at investigating the influence of the aspect ratio, b/t, and the length, L, on the performance of the arm either with or without axial compression demands. Specimen SL-L315-6.0A was used as a reference specimen for the development of the test program, and as such the test matrix presented in Table 2.1 changes to the length were made holding the aspect ratio constant to assess the effect of changing the length independently. Figure 2.3 shows the geometrical configuration of specimen SL-L315-6.0, which was initially designed for the reference wall and then selected in the current study as the control arm, as will be discussed in the following sections. Fourteen half-scale steel flexural arms were tested under displacement-controlled quasi-static fully-reversed cyclic loading. These geometrical parameters were selected herein as they significantly contributed to the displacement and force capacities of related devices as reported by Ma

et al. (2010). As shown in Table 2.1, arms used to investigate the effect of the aspect ratio are identified with S as the first letter, while those used to investigate the effects of the arm length are denoted by L. The identification SL means that the same data point was used for both datasets. Similarly, A as the last letter indicates the presence of axial compression forces. All specimens in both S and L series were tested without axial compression forces in Phase I, while specimens in Phase II were tested with applied axial compression forces. The tested arms were fabricated from 50W steel plates using water jet cutting technology to avoid residual stresses caused by heat cutting methods. In addition, two coupons were cut from each plate and used for uniaxial tests following ASTM Standard E8 (ASTM, 2003) and the results are summarized in Table 2.1.

Table 2.1: Test matrix with geometrical parameters and mean coupon test data

	ID	L (mm)	b/t	t (mm)	Fy (MPa)	Fu (MPa)
Aspect Ratio (Phase I)	S-L315-4.3	315	4.3	22.23	400	563
	S-L315-5.0	315	5.0	19.05	400	562
	SL-L315-6.0	315	6.0	15.88	400	555
	S-L315-7.5	315	7.5	12.70	508	545
Aspect Ratio (Phase II)	S-L315-4.3A	315	4.3	22.23	399	563
	S-L315-5.0A	315	5.0	19.05	392	552
	SL-L315-6.0A	315	6.0	15.88	390	539
	S-L315-7.5A	315	7.5	12.70	380	480
Length (Phase I)	L-L440-6.0	440	6.0	15.88	392	542
	L-L380-6.0	380	6.0	15.88	392	551
	SL-L315-6.0	315	6.0	15.88	400	555
	L-L255-6.0	255	6.0	15.88	385	480
Length (Phase II)	L-L440-6.0A	440	6.0	15.88	392	549
	L-L380-6.0A	380	6.0	15.88	395	555
	SL-L315-6.0A	315	6.0	15.88	390	539
	L-L255-6.0A	255	6.0	15.88	395	549

2.3.2 Flexural Arm Design

In general, flexural arms dissipate energy through strong-axis flexural yielding because wall uplifts impose shear displacements, leading to reaction force/moment demands on the arms. The boundary conditions of the flexural arms are defined by the pinhead (pinned) and the bolt group (fixed).

The initial design of the device considered in the current study extrapolated the recommendations from previous studies on analogous strong-axis flexural devices. Specifically, designs that can result in plastic hinges closer to regions of curvature change (i.e., closer to a or b in Figure 2.3) should generally be avoided by changing a and b values, which alters the point of maximum bending stress along the length of the yielding fuse (Ma et al., 2010). Taking the desired location of the maximum bending stress (or the desired location of the plastic hinge formation) at $x = 0.5L$, results in an ideal ratio a/b=1/3, (Ma et al., 2010) which was kept constant for all specimens in this study. Previous studies have also shown that if the aspect ratio of the arm (b/t) is between 2 and 9, a stable hysteretic behaviour (i.e., before buckling initiation) can be achieved up to a shear deformation (Δ/L) of 30% (Chan and Albermani, 2008; Ma et al., 2010). Therefore, the baseline design of flexural arms for this study used an aspect ratio of 6.0, near the middle of the range recommended previously. The geometry of the flexural arms considered herein resembles that of the cantilever arms tested by Toranzo (2002) as well as half of a single cut-out of the butterfly fuses investigated by Ma et al. (2010) but with different boundary conditions. Thus, similar procedures as used by Ma et al. (2010) were first used to design the fuse shape for the current device. In addition, the flexural arm

would ideally be proportioned such that all points along the outer extreme fiber of the device yield simultaneously, based on the stress at the extreme fiber. Ma et al. (2010) highlighted that although this would require an hourglass-shaped fuse with parabolic edges, straight fuse edges provided a response close to the ideal while simplifying the overall design and fabrication processes.

The current study aims at developing a device for a reference wall experiencing 3% drift, associated with a target displacement of 47 mm and yield force of 22.5 kN. This reference wall is a half-scale two-story controlled rocking masonry wall that is being investigated as a part of an ongoing research program at McMaster University to develop resilient masonry systems, and serves as just one example of the application of these devices in a controlled rocking system. The flexural arms are intended to be attached at the foundation and pinned into the wall, such as the configuration presented in Figure 2.2. Additionally, the flexural arms could be attached at rocking joints at other locations if implemented within a controlled rocking system with multiple rocking sections (e.g., Wiebe et al. in 2009). The flexural arms were designed such that the moment contribution of the restoring force remained less than one based on guidance from Kurama et al. (2005). Additionally, the design followed ITG 5.2 (2009) recommendations that limit the force developed from the flexural devices to be less than the restoring gravity force to ensure rocking joint gap closure after loading. Additional details on the design of this reference wall can be found in Yassin et al. (2021).

The yield and plastic strength prediction equations derived by Ma et al. (2010) were used to design the current devices are presented in Eqs. (2.3.1)

and (2.3.2), respectively.

$$Q_{yt} = \frac{4}{27} b^2 t \sigma_y L \tag{2.3.1}$$

$$Q_{pt} = \frac{6}{27} b^2 t \sigma_y L \tag{2.3.2}$$

where b is the width of fuse link start section, t is the thickness of fuse plateσ_y is the yield stress of steel, and L is the length of the fuse link. These equations will be revisited at the end of the current study using the experimental results to validate their predictions.

For the initial design, an approximate method was used to estimate the effects of axial loads on the response of the flexural arms, as shown in Eqs. (2.3.3) and (2.3.4). These equations first assume that the additional axial stress would cause the flexural arm to yield first in the compression fiber assuming the axial load is constant in compression across the cross section. Second, the nominal plastic strength Q_{pt} $(1.5Q_y)$ is assumed to be reached at $1.5\Delta_y$, where the yield displacements were obtained experimentally from the specimens tested in Phase I (without axial load). Furthermore, the yielding location is assumed to stay at $x = 0.5L$ by keeping the a/b ratio at 1/3. These assumptions will be compared to the experimental findings of the current study to check their validity.

$$Q_{yt,axial} = \frac{4}{27} b^2 t \sigma_{y,a} L - \frac{P\Delta_y}{L} \tag{2.3.3}$$

$$Q_{pt,axial} = \frac{6}{27} b^2 t \sigma_{y,a} L - \frac{1.5P\Delta_y}{L} \tag{2.3.4}$$

where $\sigma_{y,a}$ = yield stress, P = axial load, and Δ_y = yield displacement, obtained experimentally from testing a device without axial load.

For an aspect ratio of $b/t = 6$, the preliminary arm length ($L = 335$ mm) was determined by using 47 mm as a target displacement before buckling initiation, conservatively selected to be much less than the maximum proposed shear displacement of 30% proposed by Ma et al. (2010). Furthermore, using Eq. (2.3.1) and assuming a yield stress of 345 MPa, the remaining geometrical variables were determined ($b = 95$ mm, $a = 32$ mm, and $t = 15.875$ mm) based on readily available steel thicknesses and the desired ratio between a and b for optimal yielding initiation. All geometrical values were rounded to facilitate manufacturing, material acquisition, and force capacity. For example, the arm length was adjusted from 335 mm to 315 mm to achieve the target yield strength requirement of 22.5 kN, while all strength capacity checks and limiting areas of curvature change are satisfied. Figure 2.3 shows the geometrical configuration of specimen SL-L315-6.0, which was selected as the control arm in the current study, as will be discussed in the following sections.

The pinhead and bolt group of the flexural arm were designed not to yield under the expected loads. As such, the pinhead was detailed primarily to resist bearing failure, net section fracture, and block shear. Meanwhile, six one inch ASTM A490 bolts were designed to avoid bolt shear, bearing, net section, and block shear failures from the designed loading conditions. The typical layout of the bolts can be seen with their dimensions in Figure 2.3, and was identical for all specimens. This was conservatively over designed to ensure that the connection itself was not the limiting factor on the response of the arms, and the response of the devices was observed even at extreme limits

of performance. In actual implementation, the connection could be redesigned as needed to ensure a fixed connection based on the expected force demands on the flexural arms. Overall, the design prioritized minimal size in the connection details in order to be applied in space constrained locations of a wall or frame in practice. Finally, the curvature of the transition areas between the pinhead, yielding portion, and bolt group was selected to minimize abrupt curvature changes, as recommended by previous studies (Chan and Albermani, 2008; Ma et al., 2010; Garivani et al., 2016), to improve the ductility and minimize unintended stress concentrations.

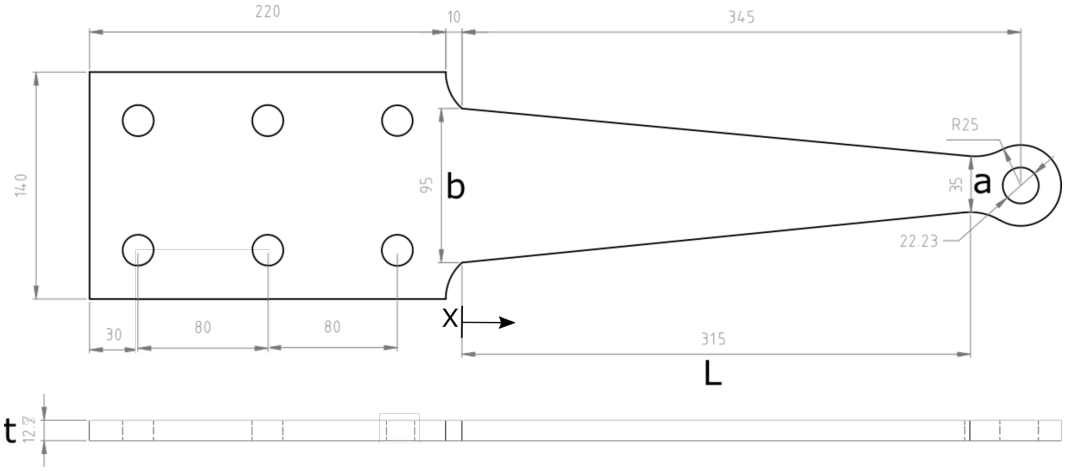

Figure 2.3: Flexural arm parameters (units in mm), parameters t and L vary (Table 2.1)

2.3.3 Test Setup

The test setup used in the current study is shown in Figures 2.4 and 2.5. The cyclic displacement was applied using a hydraulic actuator with a capacity of 120 kN and a maximum stroke of 90 mm in each direction, located at the North side of the pinhole. Axial compression forces were applied using a hydraulic actuator with a capacity of 120 kN, located at the East side of the pinhole.

The two actuators were supported vertically at both ends to avoid unintended out-of-plane loading on the specimen.

The out-of-plane system comprised a stiff reaction beam and a roller assembly to permit the in-plane displacements of the actuators, while restraining their out-of-plane displacements. The setup was inspected for damage after each test and no damage was observed at any time, except for slight elongation of the six bolt holes on the testing platform due to local bearing stresses. Lastly, eight additional mechanical stoppers were added after testing the S series specimens in Phase I, when noticeable rotations and bolt slip occurred during testing. This also prevented further deformation of the bolt holes in subsequent tests in Phase II.

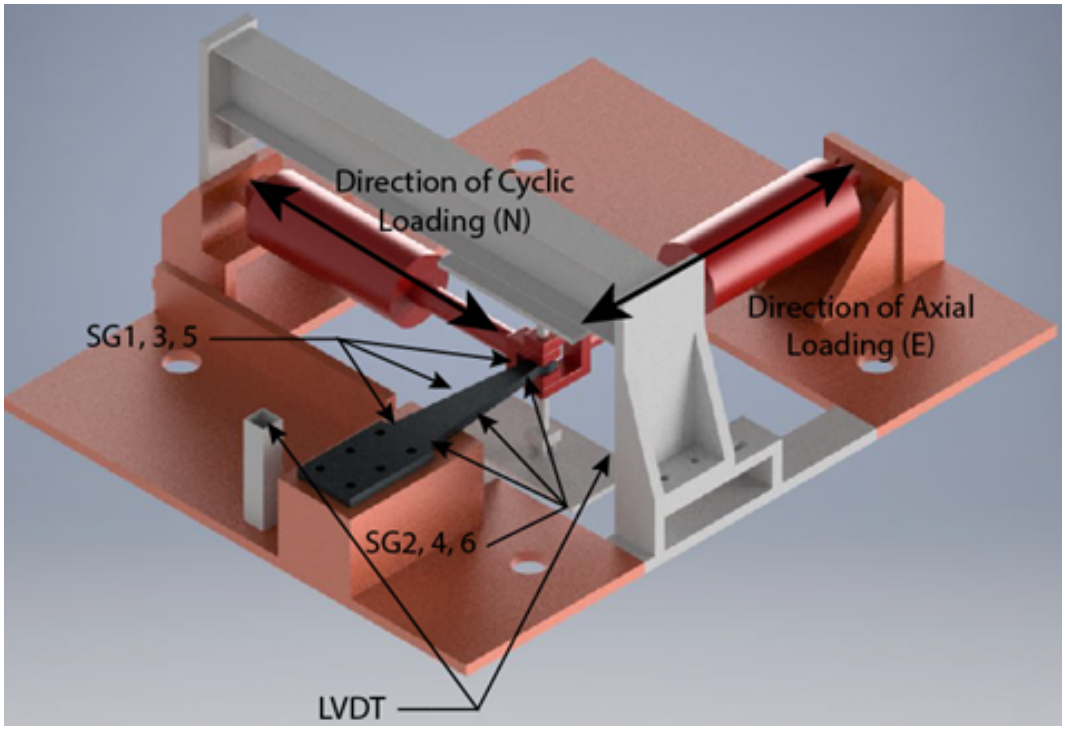

Figure 2.4: Test setup and instrumentation

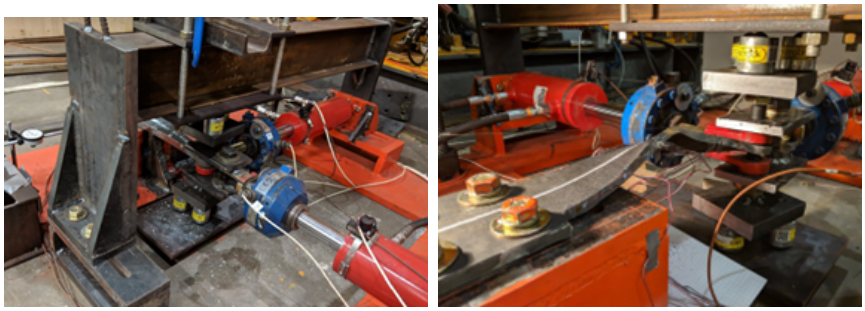

Figure 2.5: Test setup before and after testing

2.3.4 Instrumentation

Figure 2.4 shows the instrumentation used throughout the test. The two actuators were connected to their own sets of LVDTs and load cells for the control system. Two additional LVDTs were attached to the roller assembly to verify the displacements of the pinhead in both in-plane directions. As shown in Figure 2.4, six strain gauges (SG1 to SG6) were attached at mid thickness of the specimen extreme fibers at each side (SG1 and SG2 at $x = 0L$; SG3 and SG4 at $x = 0.5L$; SG5 and SG6 at $x = 1.0L$) to obtain strain profile data which was used to monitor the yielding propagation of the tested arms.

2.3.5 Loading Protocol

The displacement loading protocol shown in Figure 2.6 was defined based on FEMA 461 (FEMA, 2007). The target displacement was set to be 47 mm, which corresponds to a 3% drift of the reference wall discussed earlier, the design of which can be found in more detail in Yassin et al. (2021). The displacement protocol followed the FEMA 461 guidelines until the maximum stroke of the North displacement-controlled actuator was reached at ±90 mm

(5.75% drift). Specimens were then subjected to maximum displacement cycles until 80% strength degradation or fracture was observed. Although the application presented herein for the flexural arms involves displacements in only one direction, it was considered a more comprehensive experimental assessment to investigate the response in both directions so the devices could be used in a wider range of applications in future research studies. A constant axial force of 30 kN (38.6 – 67.5 MPa at smallest section, depending on thickness) was used for Phase II as it represented the maximum base shear that these devices would resist based on the use of four flexural arms at the base of the reference wall (see Figure 2.2). This corresponds to a maximum of 20% of the yield stress of the flexural arms from the presence of the axial load. In the configuration shown in Figure 2.2, one pair of arms would be in tension while the other would be in compression, and second-order effects could reduce the compressive stresses or possibly even lead to tensile stresses. Therefore, the worst-case scenario of a constant maximum axial compression was applied in order to assess the implications of such loading on the potential buckling and failure of the tested devices.

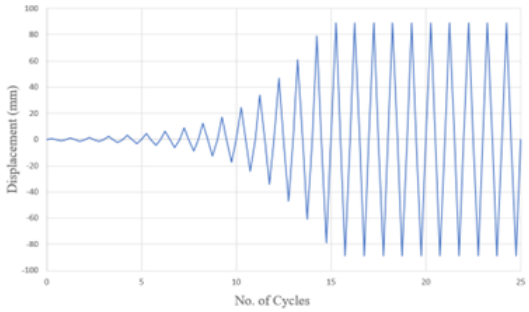

Figure 2.6: Displacement loading protocol

2.4 Experimental Program Results

2.4.1 Damage Sequence

All specimens without axial load exhibited a similar damage sequence characterized by: 1) yielding, identified by the mounted strain gauges (i.e. SG3 and SG4 were placed at the intended location of plastic hinges from design) and/or the flaking of whitewash; 2) buckling initiation, determined by visual identification; and 3) failure, defined here as 80% strength degradation or fracture.

Figure 2.7 shows the damage sequence of specimen SL-L315-6.0 from the top and side profiles. Based on the mounted strain gauges, the yield strain was first reached at a displacement of 5.44 mm. The extent of yielding at the target displacement cycle of 47 mm is shown in Figures 2.7c and 2.7d, where no buckling is visible. Signs of buckling initiation were observed at the 61 mm displacement cycle, as shown in Figure 7f. This buckling behaviour was dominated by localized buckling in the compression zone around the midpoint of the arm length, leading to progressively larger out-of-plane deflections, as shown in Figures 2.7i-j. Ultimately, the specimen failed in the fifth cycle of 90 mm displacement, as shown in Figure 2.7k-l.

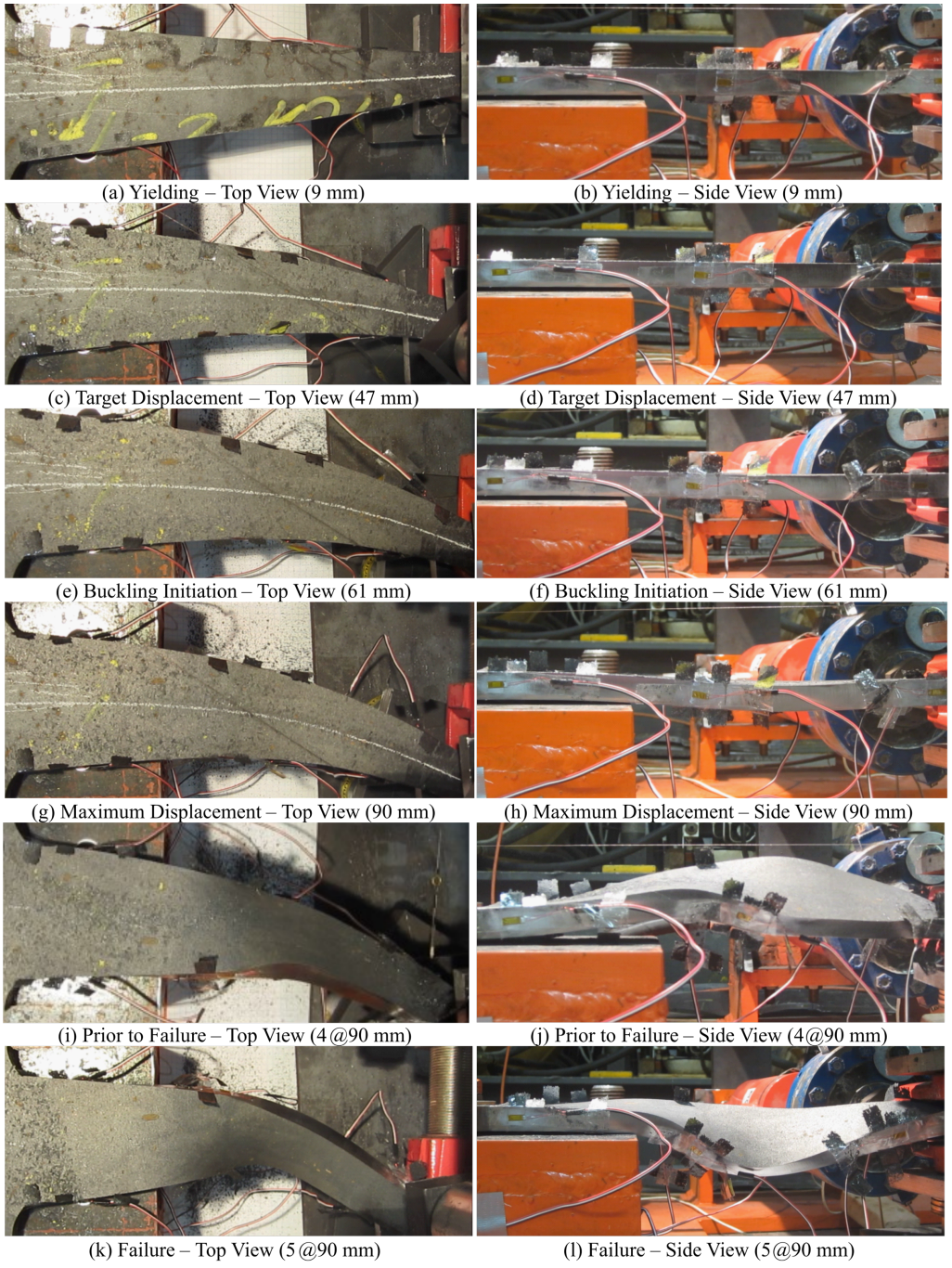

Figure 2.7: Photos of specimen SL-L315-6.0

In general, most specimens tested in Phase I experienced yielding at approximately $x = 0.5L$, where yielding/plastic hinging was originally

designed to occur, as shown in Figure 2.8 for specimen L-L380-6.0 for a clearer illustration. In addition, Figure 2.8 also shows that although exactly simultaneous yielding of the extreme outer fibers was not achieved because of the linear profile, strain hardening led to significant yielding of essentially the whole arm at large displacement demands.

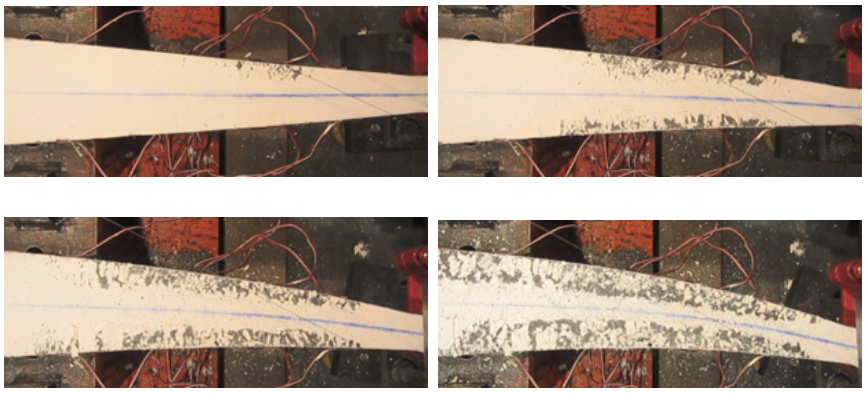

Figure 2.8: Yielding progression in specimen L-L380-6.0: (a) Yielding (6.4 mm); (b) target displacement (47 mm); (c) maximum displacement (90 mm); (d) maximum displacement prior to failure (4@90 mm)

For a direct comparison between Phase I (without axial load) and Phase II (with axial load), Figure 2.9 shows the damage sequence of specimen SL-L315-6.0A. This specimen had the same geometrical configuration of specimen SL-L315-6.0 shown earlier in Figure 2.7, but with an axial load throughout the test. From the experimental results of both specimens, the axial load accelerated the onset of yielding from 5.44 mm in Phase I to 3.25 mm in Phase II (Figures 2.7a, 2.7b, 2.9a and 2.9b), and subsequently more yielding was observed at the target displacement cycle in Phase II (with axial load) (Figures 2.7c, 2.7d, 2.9c and 2.9d). It was also observed that the actual location of yielding and buckling initiation for Phase II specimens is closer to around $x = 0.7L$, as seen in Figure 2.9a. Furthermore, although the two specimens experienced

buckling initiation at the same displacement cycle (61 mm), the 30 kN of axial compression played a major role in propagating the rapid transition of buckling behaviour as shown in Figures 2.9e, 2.9f, 2.9g, 2.9h. In addition, as shown in Figures 2.9k and 2.9l, specimen SL-L315-6.0A failed after a single displacement cycle at 90 mm, while specimen SL-L315-6.0 was able to sustain five displacement cycles at 90 mm before failure, as shown in Figures 2.7k and 2.7l. This failure pattern was the dominant behaviour in Phase II, where the axial load mainly governed the buckling behaviour as the out-of-plane deflections increased, whereas most specimen failures in Phase I were caused by lateral torsional buckling. Overall, the behaviour of the fuse under axial load can be characterized by more rapid progression through the stages of yielding, buckling initiation, and then failure.

Most specimens in Phase II (with axial load) had a greater extent of buckling compared to those in Phase I, resulting in lower displacement ductility capacities. Most tests ended when 80% strength degradation was reached, except for three specimens (S-L315-4.3, S-L315-4.3A, S-L315-5) that fractured due to low cycle fatigue. Of these three, only the thickest specimens (S-L315-4.3 and S-L315-4.3A) did not experience any buckling initiation. No cracks or visible damage aside from yielding occurred in the non-fractured specimens.

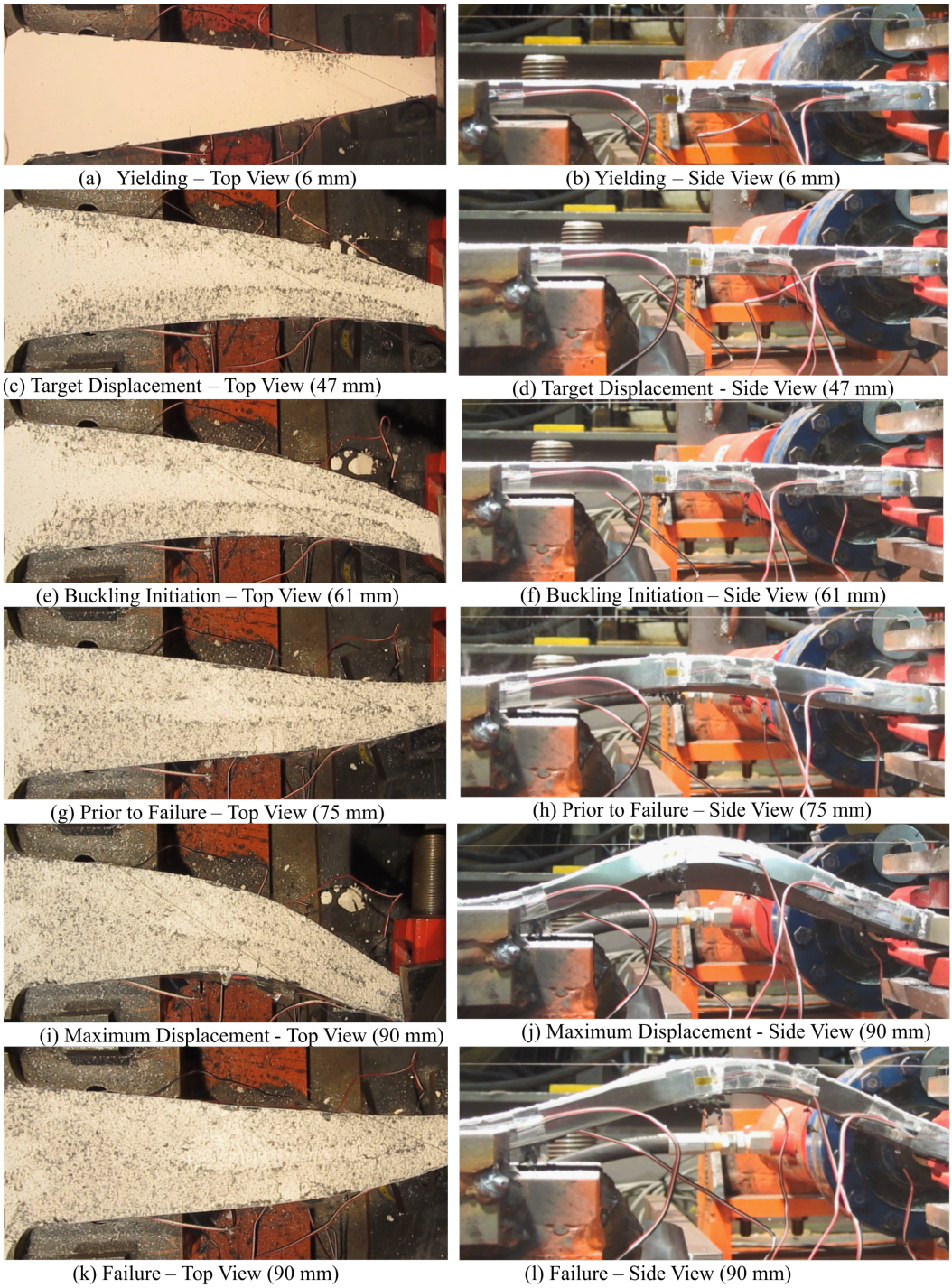

(a) Yielding – Top View (6 mm)
(b) Yielding – Side View (6 mm)
(c) Target Displacement – Top View (47 mm)
(d) Target Displacement - Side View (47 mm)
(e) Buckling Initiation – Top View (61 mm)
(f) Buckling Initiation – Side View (61 mm)
(g) Prior to Failure – Top View (75 mm)
(h) Prior to Failure – Side View (75 mm)
(i) Maximum Displacement - Top View (90 mm)
(j) Maximum Displacement - Side View (90 mm)
(k) Failure – Top View (90 mm)
(l) Failure – Side View (90 mm)

Figure 2.9: Specimen SL-L315-6.0A

2.4.2 Load-Displacement Response

Figure 2.10 shows the forces and displacements of the specimens during testing. The figure shows the influence of the length and the aspect ratio of the device on the cyclic response. As can be seen in the figure, all specimens in Phase I (without axial load) were able to reach 90 mm displacement (20-35% shear deformation) without any signs of strength degradation, with the exception of specimen S-L315-7.5, which experienced buckling failure before reaching the 90 mm displacement. As can also be seen in Figure 2.10, all specimens tested in Phase I showed positive post-yield stiffnesses and subsequently, they experienced their peak forces at peak displacements. Due to limitations in the actuator stroke, the true peak displacement capacities were not reached for all specimens in Phase I with the exception of specimen S-L315-7.5, indicating higher peak forces could also have been applied.

Most specimens tested in Phase II (with axial load) generally showed similar performance up to the maximum stroke of 90 mm, except that the presence of axial compression negatively influenced the post-yield stiffness as well as the overall peak force capacities of these specimens when compared to their counterparts in Phase I. Specimen S-L315-7.5A in particular experienced a premature buckling failure resulting in lower peak force and displacement than specimen S-L315-7.5. In addition, the peak force for most specimens in Phase II was experienced before the 90 mm displacement, unlike in Phase I. This behaviour can be attributed to the introduction of axial forces and elastic deformations/slack in the system. The inclusion of axial forces contributed to the overall instability of the flexural device leading to buckling initiation.

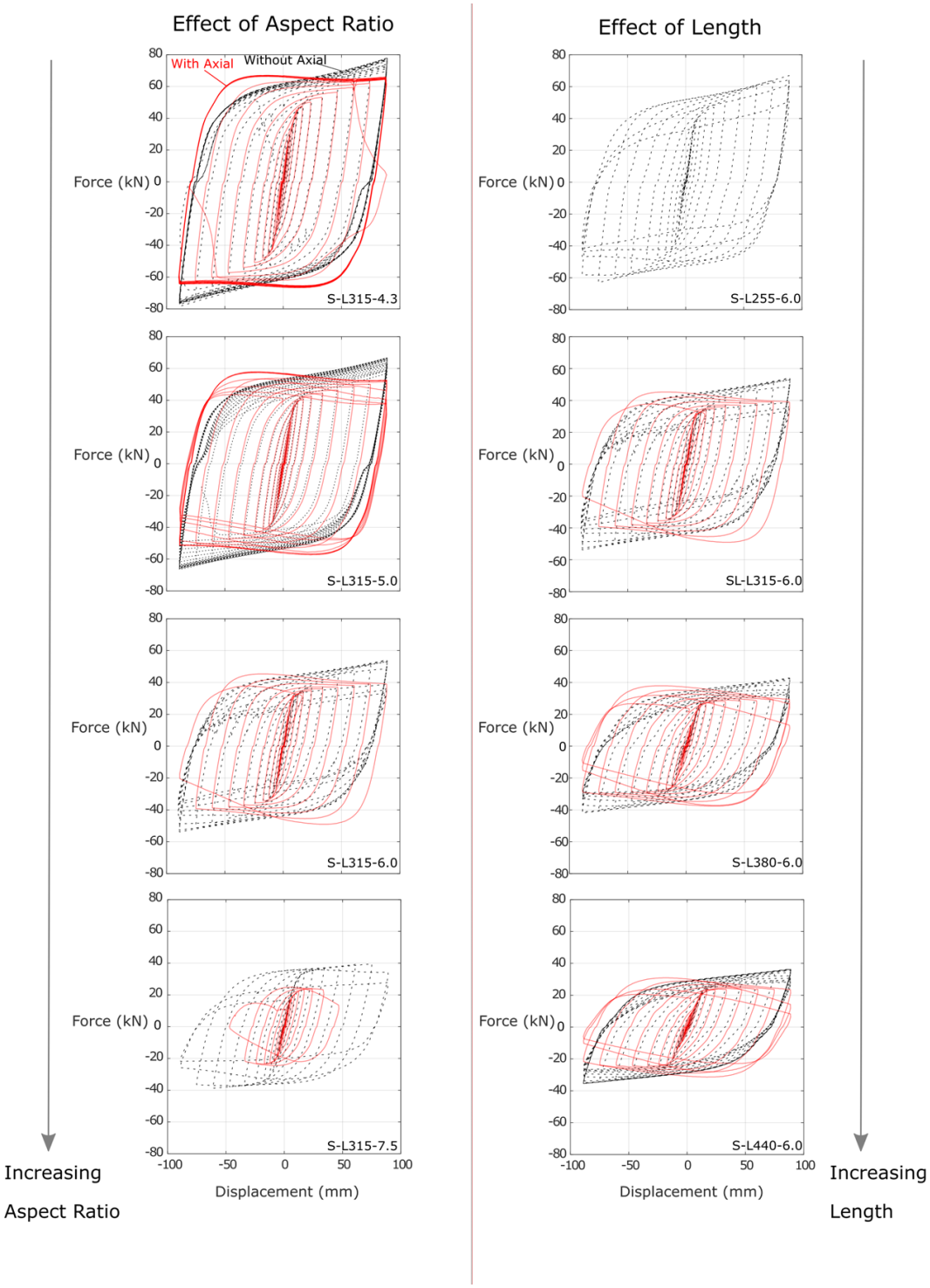

Figure 2.10: Experimental load-displacement responses

However, almost all specimens achieved the target displacement of 47 mm,

and most specimens reached peak displacements corresponding to 28.5% shear deformation, very close to the 30 that had been assumed in design, before reaching the 90 mm displacement limit of the actuator stroke.

2.5 Numerical Modelling

Figure 2.11a shows a schematic of the 3D nonlinear model that was developed using OpenSees (Mazzoni et al. 2006). The model is constructed from eight displacement-based beam-column elements of equal length with fiber sections connected through 9 nodes spaced evenly apart, with P-Delta geometric transformations assigned. Each fiber element consisted of rectangular fibers, 6 across the thickness of the cross section and 24 deep, as illustrated in Figure 2.11. The fiber elements make up the span of L (shown in Figure 2.3), as this is the portion of the device that experiences yielding. Sensitivity analysis showed that eight elements were sufficient to capture the observed results, as shown in Figure 2.11b. The depth of each fiber section matches the average depth of the flexural arm over the length of that element, and the thickness of the fiber section matches the thickness of the flexural arm.

Coupon tests were conducted for each specimen in order to calibrate the developed numerical model. Based on these tests, Steel02 with a strain-hardening ratio, b, of 0.007 was used. Other parameters that control the transition from elastic to plastic zone, *R0*, *cR1*, and *cR2* were taken as 19, 0.925, and 0.15, respectively, while isotropic hardening parameters, *a1*, *a2*, *a3*, and *a4*, were taken as 0.02, 1, 0.02 and 1, respectively, as recommended by McKenna (2011). Low cycle fatigue was included through

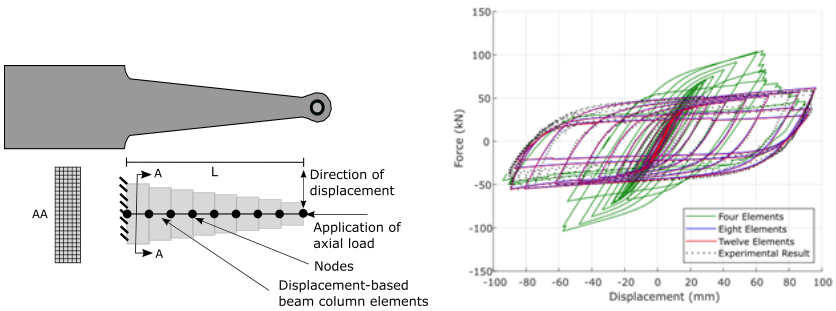

Figure 2.11: a) Model schematic (bottom) compared to flexural energy dissipation device (top) b) sensitivity of the model to the number of the elements (specimen SL-L315-6.0)

the Fatigue model developed by Uriz (2005) within OpenSees and the maximum strain obtained from the coupon tests was also included to account for fracture of the devices (Ballio et al., 1995). As seen in Table 2.1, the material properties were consistent for nearly all specimens with the exception of S-315-7.5/S-315-7.5A. Due to this, a constant value of -0.354 was used for the Coffin-Manson curve slope, even though the response of each specimes could be captured more accurately by adjusting this parameter. For specimens S-315-7.5 and S-315-7.5A a value of -0.458 was used.

2.5.1 Comparison Between Numerical and Experimental Results

Figure 2.12 shows that there is good agreement between the hysteretic response of the developed OpenSees model and the experimental results. The model peak forces are within 1.5% of the peak forces obtained experimentally. The model adequately captures the influence of the axial load and failure initiation due to low cycle fatigue. The good agreement in Figure 2.12 is consistent even varying the aspect ratio and the length of the devices.

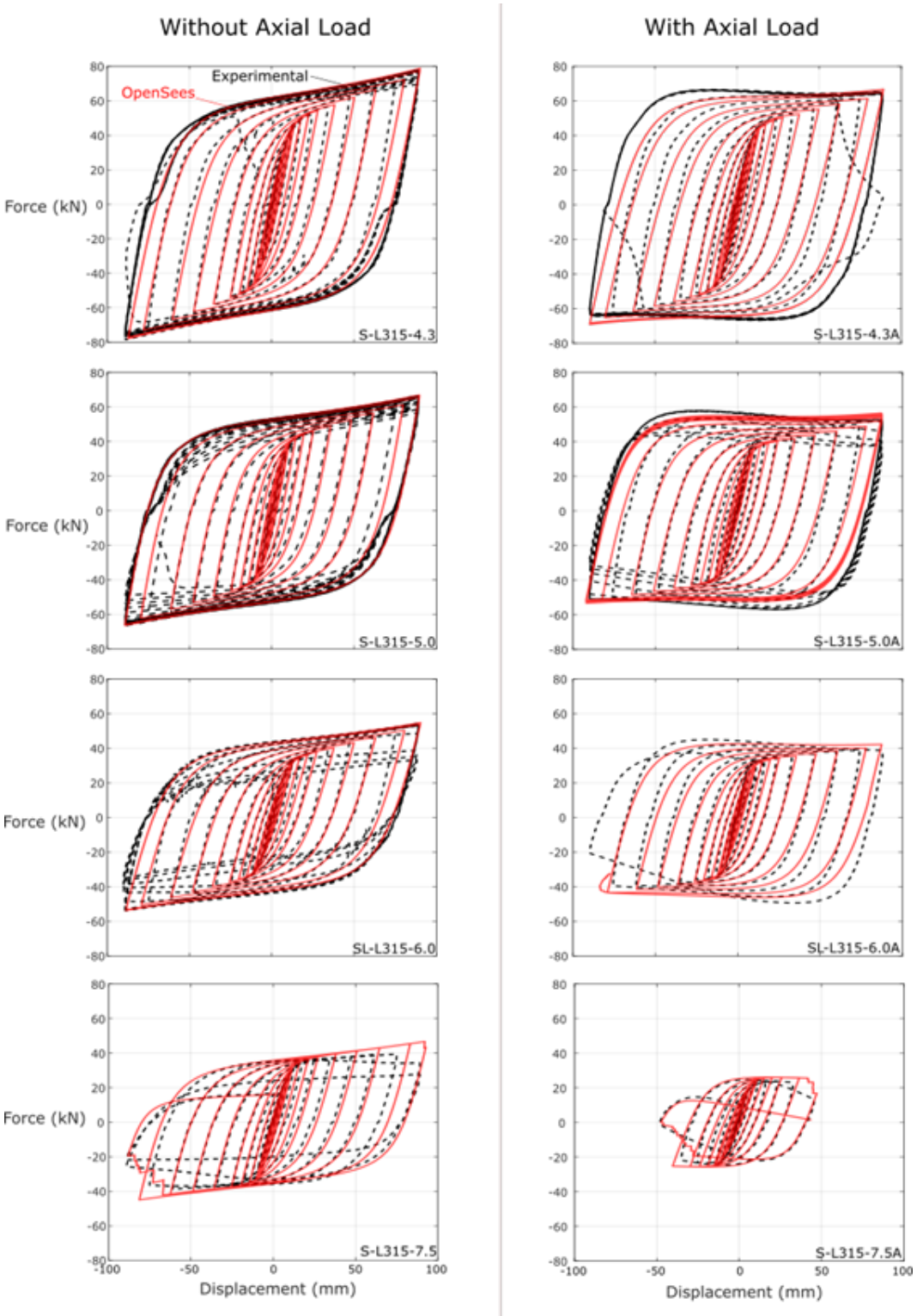

Figure 2.12: Experimental and numerical hysteresis loops

2.6 Energy Dissipation and Displacement Capacity

Figure 2.13a shows the relationship between the cumulative energy dissipated per volume of yielding steel and both b/t and L, with and without axial forces. The developed model was used to numerically evaluate arms with aspect ratios from 4.3 to 7.5 at increments of 0.1, and lengths from 250 to 450 mm at 10 mm increments. The yield and ultimate stress for these models was taken as 400 MPa and 550 MPa respectively, and the Coffin-Manson fatigue parameter was taken as -0.354, based on the typical material properties of the experimental specimens. Figure 13b plots the relationship between cumulative displacement at failure and b/t and L, with and without axial forces, both from experimental and numerical results. Each subplot of Figure 2.13 includes 15 experimental data points, representing all of the elements in the test matrix (Table 2.1) except for specimen L-L255-6.0A, for which no useful measurements were recorded during testing due to a laboratory error.

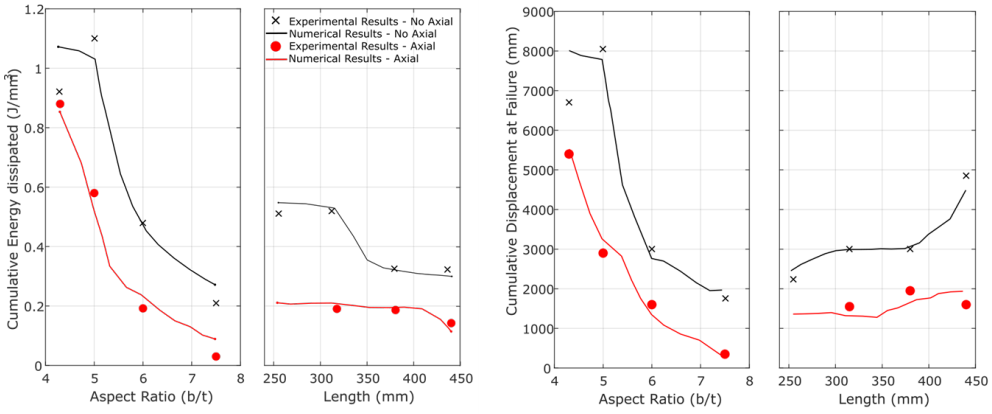

Figure 2.13: a) Cumulative Energy Dissipated per Volume of Yielding Steel and b) Cumulative Displacement compared to Aspect Ratio and Length

As seen in Figure 2.13, the axial compression forces negatively influenced the performance of flexural arms in terms of both the normalized cumulative energy dissipation and the cumulative displacement capacity before failure. Specimens with lower aspect ratios (b/t) had higher cumulative energy dissipation capacities than those with higher aspect ratios. The high energy dissipation capacities of the specimens with lower aspect ratios were primarily due to the delayed failure, which allowed for more stable hysteretic behaviour at larger and additional displacement cycles.

Although flexural arms with larger lengths (L) were able to sustain higher cumulative displacements compared to other flexural arms with smaller lengths (Figure 2.13b), the longer flexural arms showed lower normalized energy dissipation capacities (Figure 2.13a). This is because longer specimens have more steel volume and have lower stiffness and strength capacities compared to shorter specimens. This trend was observed in the experimental and numerical results when no axial load is applied. Conversely, with axial load, specimens with different lengths showed relatively similar normalized cumulative energy dissipation and cumulative displacement capacity regardless of length.

2.7 Proposed Design Equations

Theoretical yield and plastic forces ($Q_{yt},\ Q_{pt}$) for specimens tested in Phase I (without axial load) and Phase II (with axial load) were predicted by using the nominal strength design equations (Eqs. 2.3.1, 2.3.2, 2.3.3 and 2.3.4) and subsequently compared against the experimental results to assess their accuracy. For Phase II specimens, the values of Δ_y used to calculate $Q_{yt,axial}$,

and $Q_{pt,axial}$ were the measured displacements for each corresponding specimen obtained from Phase I when a strain gauge first measured 2000 µm/m. In the numerical model, the strain of each of the fibers in each of the elements was recorded in order to determine when yielding was first initiated.

As shown in Table 2.2, the yield forces for Phase I specimens, predicted using Eq. (2.3.1) are within +9% to +15% of the experimental values, except for specimen S-L315-7.5, which is attributed to the different material properties observed in the coupon tests, with a less pronounced yielding plateau and lower ultimate strain at fracture. For all other specimens in Phase I, the experimental plastic forces (Q_y) were higher than their predicted counterparts (Q_{pt}), with underpredictions between 19% and 31%.

Table 2.2: Summary of experimental results to original and proposed design equations

ID	Qy (kN)	Qp (kN)	Qyt/Qy (Original)	Qyt/Qy (Proposed)	Qpt/Qp (Original)	Qpt/Qp (Proposed)
S-L315-4.3	33.7	78.0	1.12	1.02	0.73	0.93
S-L315-5.0	28.3	68.0	1.14	1.04	0.71	0.92
SL-L315-6.0	24.3	55.0	1.11	1.01	0.74	0.93
S-L315-7.5	18.7	39.0	1.46	1.34	1.05	1.03
S-L315-4.3A	32.9	66.9	1.14	1.04	0.84	1.08
S-L315-5.0A	27.2	57.9	1.15	1.05	0.81	1.05
SL-L315-6.0A	23.2	45.3	1.11	1.01	0.86	1.08
S-L315-7.5A	15.0	24.8	1.32	1.20	1.20	1.39
L-L440-6.0	17.4	35.0	1.09	1.02	0.81	1.05
L-L380-6.0	19.0	43.0	1.15	1.07	0.76	1.00
SL-L315-6.0	24.3	55.0	1.11	1.01	0.74	0.93
L-L255-6.0	28.6	69.0	1.12	1.00	0.70	0.78
L-L440-6.0A	16.5	30.9	1.11	1.04	0.89	1.18
L-L380-6.0A	20.1	37.5	1.07	0.99	0.86	1.13
SL-L315-6.0A	23.2	45.3	1.11	1.01	0.86	1.08
Mean			1.15	1.06	0.84	1.04
C.o.V. (%)			8.61	8.42	15.64	13.08

The yield values that were predicted for specimens tested in Phase II using Eq. (2.3.3) were within +5% to +11% of the experimental findings, while the predicted peak values using Eq. (2.3.4) were within -12% to -32% of the experimental results, as presented in Table 2.3.

To enhance the accuracy of the design equations, the following two changes are proposed based on the experimental observations. First, L as presented in Eqs. 2.3.1, 2.3.2, 2.3.3 and 2.3.4 is proposed to be changed to the parameter h, as shown in Figure 2.3. This change is based on the mechanical derivations which take the yield/plastic force as the yield/plastic moment, divided by the moment arm, which is captured more accurately by the parameter h than L based on the geometry of the devices. Second, σ_y in Eqs. (2.3.2) and (2.3.4) (the equations for plastic force) is proposed to be changed to the ultimate stress σ_u to provide a better estimate of the plastic strength. These changes result in Eqs (2.7.1) and (2.7.2) for $Q_{yt,axial}$ and $Q_{pt,axial}$ respectively. In Eq. (2.7.1) and (2.7.2), Δ_y is obtained either experimentally, with the proposed numerical model, or with Eq. (2.7.3) derived from an Euler Bournoulli beam element. Eq. (2.7.3) neglects the axial force, as in practical application this force would be variable and not applied constantly to the device as was done in the experimental tests. As the devices yield at relatively low displacements in comparison to the displacement capacity, it was assumed that the influence of the axial load on the yield displacement would be negligible.

$$Q_{yt,axial} = \frac{4}{27} b^2 t \sigma_{y,a} h - \frac{P\Delta_y}{h} \tag{2.7.1}$$

$$Q_{pt,axial} = \frac{6}{27} b^2 t \sigma_{u,a} h - \frac{1.5P\Delta_y}{h} \tag{2.7.2}$$

$$\Delta_y = \frac{6h^3 Q_y}{Et(b-a)^3}\left(\frac{b}{a} - \frac{a}{b} - 2ln\left(\frac{b}{a}\right)\right) \tag{2.7.3}$$

As can be seen in Table 2.3, the proposed design equations are more accurate in calculating the yield and peak strengths for both Phase I and Phase II specimens. The proposed yield strength equation obtained an error of -1% to +7% (when omitting specimen S-L315-7.5A as discussed previously), while the proposed peak strength equation obtained an error within -8% to +18%.

The validated numerical model was used to simulate the performance of a wide range of flexural arms with different lengths (from 250 mm to 700 mm) and aspect ratios (from 3.0 to 7.5) to further investigate the accuracy of the proposed design equations. Figure 2.14 compares the proposed yield displacement equation to the experimental and numerical results, while Figures 2.15 and 2.16 compare the yield and plastic forces obtained from the proposed equations to those from the numerical model and experimental tests. The proposed design equations show very close agreement to the yield displacements, yield forces, and plastic forces of the numerical results, including beyond the range of the experimental tests. There is less agreement between the experimental results and the proposed equations and numerical results for specimens S-L315-7.5 and S-L315-7.5A because of the different material properties for these specimens as discussed earlier. The yield displacement equation underpredicts the yield displacement by around 20% due to the assumptions made in the formulation of Eq. (2.7.3) of an Euler Bournoulli beam element.

The addition of axial load has very little influence on the yield displacement and force in the experiments, the model and the equations. While there is some

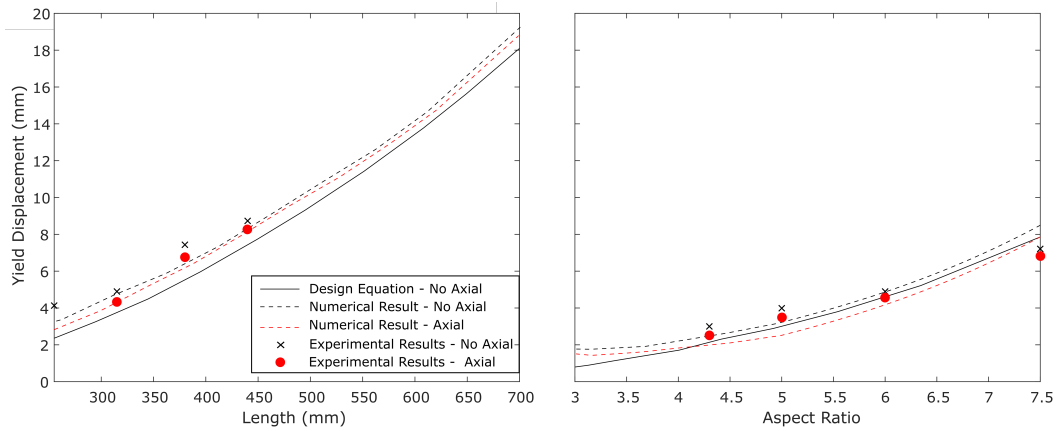

Figure 2.14: Comparison of yield displacements (Δ_y) from design equation 7, numerical model and experimental results

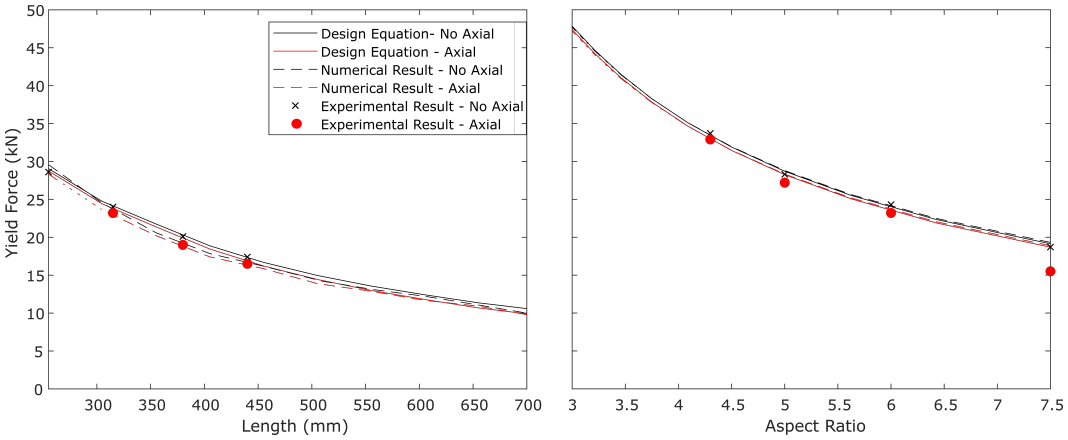

Figure 2.15: Comparison of yield forces (Q_y) from design equations, numerical model, and experimental results

influence on the plastic force, the axial force on the device within an actual wall or frame system would not be constant as they were in this study. When the axial force is known, the proposed design equations incorporating axial load still seem accurate enough to be used for capacity design purposes.

These design equations are intended to be used both to calculate the force contribution from the flexural arms and to quantify key points in the response of the arms. Depending on where the devices are located, the geometry of the installation (such as the distance from the rocking point), and the required

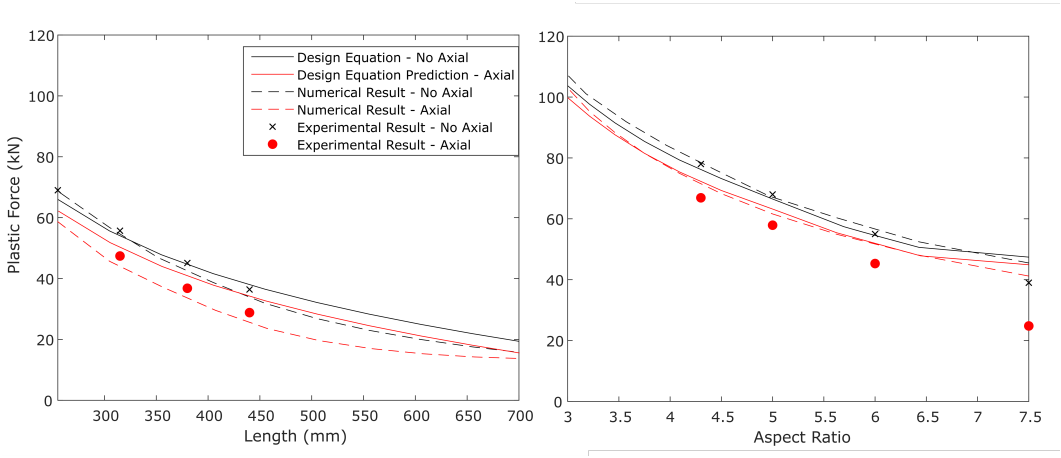

Figure 2.16: Comparison of plastic forces (Q_p) from design equations, numerical model, and experimental results

force and displacement capacity, Eq. 2.7.1 - 2.7.3 can be used as part of the design process for a multitude of different controlled rocking systems.

2.8 Conclusions

The current paper presented the experimental results of fourteen flexural arms which were designed and tested for use as energy dissipation devices for controlled rocking systems. The energy dissipation mechanism of these arms is based on the strong-axis bending of a cantilever arm. Unlike previous studies, the performance of these flexural arms was investigated in the current study under both cyclic displacement and axial compression forces simultaneously to see if the devices could eliminate the need for mechanical stoppers to prevent sliding by withstanding the base shear themselves. The fourteen test specimens were used to investigate the influence of key design parameters, namely the length, the aspect ratio, and the inclusion of axial compressive force. The results of these tests were subsequently used to

develop and validate a numerical model to capture the response of such devices. The developed numerical model and the experimental results were then used to propose and validate new design equations for yield and plastic strengths, and yield displacement.

The aspect ratio was found to have the greatest impact on the performance of the tested devices, both with and without the application of axial load. The experimental results showed stable, desirable hysteretic performance for the devices with lower aspect ratios (thicker weak axis), and favorable results for a wide range of different lengths (80% to 140% of the initial design length). The axial load was found to decrease the peak strength of the devices at large displacements, while only having a minor influence on the yield force and displacement. The axial load was found to reduce the yield force between 2.4% and 5.4%, while the energy dissipated was reduced by a range of 6% to 53%. The validated numerical model showed that the proposed design equations are highly accurate within aspect ratios ranging from 3 to 7.5 and lengths ranging from 80% to 220% of the reference device length.

The relevant design parameters and equations investigated, developed and recommended by this study are:

- A ratio of dimensions a/b of 1/3 for the desirable location of first yielding
- An aspect ratio (b/t) between 3 and 7.5 to ensure stable hysteretic performance in the presence of axial load
- Equations 2.7.1, 2.7.2 and 2.7.3 (yield force, plastic force and yield displacement respectively) to be used for design within the limits noted above

- The devices can be designed to withstand an axial load, eliminating the need for stoppers to prevent sliding, provided the axial force in the flexural arm remains below the recommended level of 15% of the yield stress at the smallest cross section

In summary, this study furthers the development of a cost-efficient, replaceable, easy-to-use flexural energy dissipation device with a desirable performance that can be quantified by the proposed design equations. Notably, this study did not examine the implementation of these devices in wall systems, and as such, future research studies are still needed to compare the performance of the devices as described herein with their performance when installed and tested within controlled rocking systems, as well as to better understand the performance of these devices under variable types of axial loading demands.

2.9 Acknowledgements

The financial support for this project was provided through the Canadian Concrete Masonry Producers Association (CCMPA), the Canada Masonry Design Centre (CMDC), the Natural Sciences and Engineering Research Council (NSERC), and the Ontario Centres of Excellence (OCE).

2.10 Data Availability Statement

All data, models, and code generated or used during the study appear in the submitted article.

2.11 References

ACI ITG-5.2 (American Concrete Institute). (2009). "Requirements for Design of a Special Unbonded Post-Tensioned Precast Shear Wall Satisfying ACI ITG-5.1 & Commentary." *ACI ITG-5.2-09*, Farmington Hills, MI

Aiken, I., Nims, D., Whittaker, A., and Kelly, J. (1993). "Testing of passive energy dissipation systems." *Earthquake Spectra*, 9(3), Earthquake Engineering Research Institute, California.

ASTM Standard E8. (2003). "Standard test methods for tension testing of metallic materials." *American Society for Testing and Materials.* pp. 62-79.

Ballio, G. and Castiglioni, C. A., (1995). "A Unified Approach for the Design of Steel Structures under Low and/or High Cycle Fatigue." *Journal of Constructional Steel Research*, 34, 75-101

Bergman, D. M. and Goel, S. C. (1987). "Evaluation of cyclic testing of steel plate devices for added damping and stiffness." *Report No. UMCE87-10*, the University of Michigan.

Chan, R. W. K. and Albermani, F. (2008). "Experimental study of steel slit damper for passive energy dissipation." *Engineering Structures*, 30, pp. 1058-1066.

D'Ayala, D. F., and Paganoni, S. (2014). "Testing and design protocol of dissipative devices for out-of-plane damage". *Proceedings of the Institution of Civil Engineers-Structures and Buildings*, 167(1), 26-40.

Di Cesare, A., Ponzo, F. C Pampanin, S. Smith, T., Nigro, D., and Lamarucciola, N. (2019). "Displacement based design of post-tensioned timber framed buildings with dissipative rocking mechanism", *Soil Dynamics and Earthquake Engineering*, 2019, 116, pp. 317-330.

Di Cesare, A., Ponzo, F., Lamarucciola, N. and Nigro, D. (2020). "Dynamic Seismic Response of Nonlinear Displacement Dependent Devices versus Testing Required by Codes: Experimental Case Studies". *Applied Sciences*, 10(24), 8857.

Eldin, S., and Galal, K. (2017). "In-plane seismic performance of fully routed reinforced masonry shear walls." Journal of Structural Engineering, 143(7), 04017054.

Erochko, J., Christopoulos, C., and Tremblay, R. (2015). "Design, testing, and detailed component modeling of a high-capacity self-centering energy-dissipative brace." *Journal of Structural Engineering*, 141(8), 04014193.

Ezzeldin, M., El-Dakhakhni, W., and Wiebe, L. (2017). "Experimental assessment of the system-level seismic performance of an asymmetrical reinforced concrete block–wall building with boundary elements." *Journal of Structural Engineering*, 143(8), 04017063

FEMA 461. (2007). "Interim testing protocols for determining the seismic performance characteristics of structural and non-structural components." Federal Emergency Management Agency.

Garivani, S., Aghakouchak, A. A., and Shahbeyk, S. (2016). "Numerical and experimental study of comb-teeth metallic yielding dampers." *International Journal of Steel Structures*, 16, pp. 177-196.

Iqbal, A., Pampanin, S., Palermo, A., and Buchanan, A. H. (2015). "Performance and design of LVL walls coupled with UFP dissipaters". *Journal of Earthquake Engineering*, 19(3), 383-409.

Giresini, L., Solarino, F., Taddei, F., Mueller, G. (2021) "Experimental estimation of energy dissipation in rocking masonry walls restrained by an innovative seismic dissipator (LICORD)", *Bulletin of Earthquake Engineering* 9, pp. 2265-2289

Granello, G., Palermo, A., Pampanin, S., Pei, S., and Van De Lindt, J. (2020). "Pres-lam buildings: state-of-the-art". *Journal of Structural Engineering*, 146(6), 04020085.

Gray, M. G., Christopoulos, C., and Packer, J. A. (2014). "Cast steel yielding brace system for concentrically braced frames: concept development and experimental validations." *Journal of Structural Engineering*, 140(4), 04013095.

Holden, T., Restrepo, J. I., and Mander, J. B. (2002). "Seismic performance of precast reinforced and prestressed concrete walls." *Journal of Structural Engineering*, ASCE, 129(3), pp. 286-296.

Kalliontzis, D., and Schultz, A. E. (2017). "Characterizing the in-plane rocking response of masonry walls with unbonded posttensioning." *Journal of Structural Engineering*, 143(9), 04017110.

Kam, W. Y., Pampanin, S., Palermo, A., and Carr, A. J. (2010). "Self-centering structural systems with combination of hysteretic and viscous energy dissipations." *Earthquake Engineering & Structural Dynamics*, 39(10), 1083-1108.

Kobori, T., Miura, Y., Fukusawa, E., Yamada, T., Arita, T., and Takenake, Y. (1992). "Development and application of hysteresis steel dampers." Proc. 11th World Conference on Earthquake Engineering, pp. 2341-2346.

Kurama, Y. (2005). "Seismic Design of Partially Post-Tensioned Precast Concrete Walls." PCI Journal, 50(4), 100–12

Laursen, P. T. and Ingham, J. M. (2004). "Structural Testing of Enhanced Post-Tensioned Concrete Masonry Walls." *Journal of Structural Engineering*, 130(10), pp. 1497-1505.

Ma, X., Borchers, E., Pena, A., Krawinkler, H., Billington, S., and Deierlein, G. G. (2010). "Design and behaviour of steel shear plates with openings as energy-dissipating fuses." The John A. Blume Earthquake Engineering Center, Report No.173.

McKenna, F. (2011). OpenSees: a framework for earthquake engineering simulation. Computing in Science & Engineering, 13(4), 58-66.

Nochebuena-Mora, E., Mendes, N., Lourenço, P. B., and Covas, J. A. (2021). "Vibration control systems: A review of their application to historical unreinforced masonry buildings". *Journal of Building Engineering*, 44, 103333.

Pampanin, S. (2002) "Innovative seismic connections for precast concrete buildings". ELITE - *The International Journal of Precast Art*, 4, pp. 53-60.

Perez, F. J., Sause, R., and Pessiki, S. (2007). "Analytical and experimental

lateral load behavior of unbonded posttensioned precast concrete walls." *Journal of Structural Engineering*, 133(11), 1531-1540.

Ponzo, F. C. , Di Cesare, A., Lamarucciola, N., Nigro, D., and Pampanin, S. (2017). "Modelling of post-tensioned timber-framed buildings with seismic rocking mechanism at the column-foundation connections", *International Journal of Computational Methods and Experimental Measurements*, 5(6), pp. 966-978

Ponzo, F. C. , Di Cesare, A., Lamarucciola, N., and Nigro, D. (2019) "Seismic Design and Testing of Post-tensioned Timber Buildings With Dissipative Bracing Systems", *Frontiers in Built Environment*, 5, pp. 104

Priestley, M. J. N., Sritharan, S., Conley, J. R., and Pampanin, S. (1999). "Preliminary results and conclusions from the PRESSS five-story precast concrete test building." *PCI Journal*, 44(6), pp. 42-67.

Rahman, A. M., and Restrepo-Posada, J. I. (2000). "Earthquake resistant precast concrete buildings: seismic performance of cantilever walls prestressed using unbonded tendons." *Ph.D. Dissertation*, Department of Civil Engineering, University of Canterbury, New Zealand.

Restrepo, J. I. and Rahman, A. (2007). "Seismic performance of self-centering structural walls incorporating energy dissipators." *Journal of Structural Engineering*, 133(11), pp. 1560-1570.

Saeedi, F., Shabakhty, N., and Mousavi, S. (2016). "Seismic assessment of steel frames with triangular-plate added damping and stiffness devices." *Journal of Constructional Steel Research*, 125, pp. 15-25.

Sarti, F., Palermo, A., Pampanin, S., and Berman, J. (2017). "Determination of the seismic performance factors for post-tensioned rocking timber wall systems." *Earthquake Engineering & Structural Dynamics*, 46(2), 181-200.

Toranzo, L. A. (2002). "The use of rocking walls in confined masonry structures: a performance-based approach." *Ph.D. Dissertation*, Department of Civil Engineering, University of Canterbury, New Zealand.

Toranzo, L. A., Restrepo, J. I., Carr, A. J., and Mander, J. B. (2004). "Rocking confined masonry walls with hysteretic energy dissipators and shake-table validation." *Proc. 13th World Conference on Earthquake Engineering*, Paper No.248.

Toranzo, L. A., Restrepo, J. I., Mander, J. B., and Carr, A. J. (2009). "Shake-table tests of confined-masonry rocking walls with supplementary hysteretic damping." *Journal of Earthquake Engineering*, 13(6), pp. 882-898.

Tremblay, R., Lacerte, M., and Christopoulos, C. (2008). Seismic response of multistory buildings with self-centering energy dissipative steel braces. *Journal of Structural Engineering*, 134(1), 108-120.

Tsai, K. C., Chen, H. W., Hong, C. P., and Su, Y. F. (1993). "Design of steel triangular plate energy absorbers for seismic-resistance construction." *Earthquake Spectra*, 9, pp. 505-528.

Uriz, P. (2005). "Towards Earthquake Resistant Design of Concentrically Braced Steel Structures.". *Doctoral Dissertation*, Department of Civil

and Environmental Engineering, University of California, Berkeley, United States of America.

Wiebe, L., and Christopoulos, C. (2009). "Mitigation of higher mode effects in base-rocking systems by using multiple rocking sections". *Journal of Earthquake Engineering*, 13(S1), 83-108.

Wiebe, L., Christopoulos, C., Tremblay, R., and Leclerc, M. (2013). Mechanisms to limit higher mode effects in a controlled rocking steel frame. 2: large-amplitude shake table testing. *Earthquake Engineering & Structural Dynamics*, 42(7), 1069-1086.

Xia, C. and Hanson, R. (1992). "Influence of ADAS element parameters on building seismic response." Journal of Structural Engineering, ASCE, 118, pp. 1903-1918.

Yassin A, Ezzeldin M, Wiebe L. (2021). Under Review. "Experimental assessment of resilient controlled rocking masonry walls with replaceable energy dissipation". Submitted to ASCE *Journal of Structural Engineering*, STENG-11258.

Yassin, A., Ezzeldin, M., Steele, T., and Wiebe, L. (2020). "Seismic Collapse Risk Assessment of Posttensioned Controlled Rocking Masonry Walls." *Journal of Structural Engineering*, ASCE, 146(5), 04020060.

Zheng, J., Zhang, C., and Li, A. (2020). Experimental investigation on the mechanical properties of curved metallic plate dampers. *Applied sciences*, 10(1), 269.

Chapter 3

Strategies to Reduce and Quantify Seismic Damage in Controlled Rocking Masonry Walls

3.1 Abstract

Controlled rocking systems have been used in numerous structures around the world as a seismic force-resisting system. In a controlled rocking wall system, the wall is allowed to uplift from the foundation during seismic events, thus reducing the wall's lateral stiffness and minimizing its corresponding seismic force demands. This rocking mechanism is often controlled using post-tensioning (PT) tendons, resulting in negligible residual deformations compared to conventional walls (i.e., with fixed bases). For these reasons, promising strides have been taken to apply the concept of controlled rocking systems to masonry walls; however, several issues have been encountered when using PT tendons due to the brittle nature of the masonry material in compression. To address this, the current study aims to reduce damage and improve performance of controlled rocking masonry walls

(CRMWs) by omitting PT, instead relying on gravity loads and energy dissipation to control the seismic response. Three strategies to achieve this improved performance are proposed and investigated. The first strategy involves using externally mounted, replaceable energy dissipation devices; the second strategy introduces a steel base for the rocking wall; and the third strategy considers confinement plates in the rocking toe region of the wall. To assess these strategies, the study develops and validates a numerical model to capture the performance of previously tested CRMWs. The model is then used to develop and experimentally validate an index for masonry walls to quantify their damage based on numerical results. Next, a suite of 20 CRMWs is designed, 5 of which incorporate PT tendons while the remaining 15 walls omit PT and incorporate one or more of the proposed strategies to reduce damage. Numerical models of all of the archetype walls are subjected to reversed cyclic loading protocols, and the amount of damage incurred is compared across each archetype wall. The results demonstrate that the proposed modelling technique and damage index are effective at capturing the response and quantifying damage in CRMWs, and that the proposed strategies result in a lower damage alternative to post-tensioned CRMWs (PT-CRMWs).

3.2 Introduction

Masonry is one of the world's oldest construction materials still used extensively for low- to mid-rise residential, commercial, and industrial structures. However, modern seismic design requirements have significantly affected the practicality of masonry structures as relevant standards consider

them less ductile than their counterparts constructed from reinforced concrete or steel, and thus more vulnerable during seismic events. The seismic vulnerability of masonry structures has been also observed in many earthquakes, notably Northridge in 1994 (Eguchi et al. 1998). A design concept that has recently been investigated to mitigate such a vulnerability is the use of self-centering structures with rocking as the primary mode of deformation, as opposed to typical shear- and flexurally-dominated deformations (ACI Innovation Task Group 5 2009). In a controlled rocking system, the wall is unbonded from the foundation and is subsequently allowed to uplift from the foundation during seismic events. Adopting such a design concept allows controlled rocking systems to have almost zero residual deformations and less damage compared to conventional systems with fixed bases.

Several research studies have applied the concept of controlled rocking to masonry walls, such as Laursen and Ingham (2004), Rosenboom and Kowalsky (2004), Hassanli et al. (2017), and Yassin et al. (2020). These studies relied on post-tensioning (PT) tendons to provide restoring forces that return the wall to its original vertical alignment following a seismic event. When these walls are subjected to in-plane lateral loading, a single major crack forms at the wall-foundation interface. By further increasing this in-plane loading, the wall uplifts from the foundation. When the load is released, the PT tendons return the wall to its initial position.

The above studies reported that damage was localized to the lowest masonry courses in the rocking toe region, and a high self-centering ability was achieved by controlled rocking masonry walls (CRMWs) (Laursen and Ingham 2004; Rosenboom and Kowalsky 2004; Hassanli et al. 2017; Yassin et

al. 2020). However, these studies also demonstrated that there are key issues that still need to be addressed to further mitigate damage and maintain low residual deformations. For example, the installation of PT tendons complicates construction and ultimately can lead to poor performance in terms of the wall deformation capacity due to a combination of PT losses and premature compressive failure of the masonry due to the additional compression placed on the rocking toe (Rosenboom and Kowalsky 2004). In addition, a study by Hassanli et al. (2017) reported that CRMW systems have low inherent damping compared to conventional masonry systems as the CRMWs remain mostly elastic.

A recent study by Yassin et al. (2022a) investigated the performance of CRMWs that do not use PT but instead rely on gravity loads for self-centering, together with internal axial yielding energy dissipation devices to control the peak displacement response. While these CRMWs produced a favorable hysteretic response with minimal damage, the irreplaceability of devices installed inside the wall leads to issues surrounding the repair and replacement of the energy dissipation (Yassin et al. 2022a). To address this, additional studies have been conducted to develop an externally mounted energy dissipation device (i.e., a steel flexural arm) that can be easily replaced following a seismic event (Li 2019; East et al. 2020; East et al. 2022). The studies experimentally and numerically investigated the performance of such external devices and established design equations that can be used to incorporate them into CRMW systems (East et al. 2022). A second study by Yassin et al. (2022b) tested a single wall incorporating these flexural yielding energy dissipation devices within a CRMW. However, more CRMWs incorporating these devices still need to be investigated to evaluate

their seismic response when different design parameters are adopted (e.g., aspect ratio, axial load ratio, amount of energy dissipation).

The current study proposes three strategies to further enhance the performance and reduce the damage of CRMWs without PT. The three strategies that are adopted are: (1) externally attached energy dissipation devices, (2) the use of a steel section at the base of the wall, and (3) confining plates at the bed joints within the rocking toe region. A system that incorporates all three strategies addresses the low inherent damping of CRMWs and mitigates damage at the rocking toe of the wall. In this respect, a nonlinear finite element model is developed and validated against previous experimental studies to simulate the behavior of CRMWs. To quantify the damage and assess the improvements associated with each of the proposed strategies, a damage index is then introduced for reinforced masonry walls throughout reversed cyclic analyses. This damage index is validated through a comparison of the numerical results to damage reported in previous experimental programs. Next, five different geometrical configurations of CRMWs are selected to examine the impacts of different aspect ratios, construction details, axial loads, and material properties. Each configuration is designed in four distinct ways, resulting in a total of 20 walls. First, the walls are designed using PT as a reference. The second set incorporates external energy dissipation devices (i.e., the first strategy) without the use of PT. The third set includes the first strategy, while also constructing atop a steel rocking component (i.e., the second strategy). The fourth set considers strategies one and two, while also adding confinement plates in the rocking toe (i.e., the third strategy). The developed damage index is used to indicate damage states throughout the analysis, thus

quantifying the enhancements of the proposed system compared to a post-tensioned CRMW (PT-CRMW) system.

3.3 Numerical Model

3.3.1 Selection of Elements

Figure 3.1 shows the schematic that outlines the various components of the OpenSees model developed in the current study. As can be seen in the figure, the masonry was modelled using a series of 4-node, multi-layered shell elements with smeared layers to account for the vertical and horizontal reinforcement present in the wall, atop a base of compression-only springs, all assigned nonlinear corotational coordinate transformations. The PT tendons were modelled separately as truss elements, along with the energy dissipation devices at the base of the wall, when necessary, as not all modelled walls used PT and energy dissipation devices.

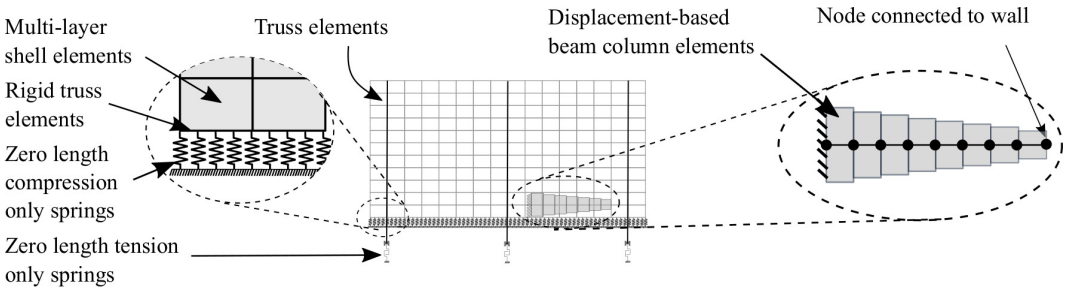

Figure 3.1: Model schematic for CRMWs

The multi-layered shell elements indicated in Figure 3.1 are based upon the work by Dvorkin et al. (1995) regarding the theory of mixed interpolation of tensorial components (MITC). This element was originally implemented in OpenSees (Mazzoni et al. 2006) by Lu et al. (2015) to model

the seismic response of reinforced concrete shear walls in super tall buildings. The element (ShellMITC4 in OpenSees) was then used by El-Hashimy et al. (2019) to simulate the out-of-plane behavior of fully-grouted reinforced masonry shear walls. The ShellMITC4 element is a four-node composite element that simplifies the three-dimensional behavior of the composite section into several fully-bonded layers in the thickness direction. The calculated stresses over a layer of thickness are assumed to be consistent with those at the mid-surface point of that layer, such that the element can predict the stress distribution over the thickness of the wall (Guan and Loo 1997; Hallinan and Guan 2007; Lu et al. 2013, 2015). A nonlinear material behavior in the form of cracking and aggregate interlocking is also incorporated in the planar concrete constitutive model.

The rocking interface shown in Figure 3.1 at the base of the wall is modelled with a series of zero-length, compression-only springs. The spacing between the springs was limited to a maximum of 12 mm in order to avoid convergence issues within the model. As there are significantly more springs than shell elements at the wall base, the nodes that align with the shell elements are connected directly to the springs, while the remaining springs are connected to the shell elements through a series of rigid truss elements, as shown in Figure 3.1. The PT tendons (when necessary) are modelled using truss elements with a tension-only spring to prevent developing compression in the tendons.

The flexural yielding energy dissipation device is modelled following the technique that was developed and validated by East et al. (2022) based on a set of 14 experimental device tests by Li et al. (2019). The devices (when necessary) are modelled using a series of displacement-based fiber elements in OpenSees. Figure 3.1 shows the flexural arm model incorporated into the

CRMW model. Full detail regarding the modelling approach and validation can be found in East et al. (2022).

3.3.2 Material Models

The multi-layer shell elements described above incorporate several material models using an nDMaterial in OpenSees called PlaneStressUserMaterial. The masonry fibers follow a modified Kent-Scott-Park stress-strain material model that is available as Concrete01 in OpenSees (Mazzoni et al. 2006). The parameters specified for the masonry material layers are defined by the compressive strength, tensile strength, crushing strength, strain at maximum strength, strain at crushing strength, ultimate tensile strain, and shear retention factor. To confirm that the multi-layer shell element could capture the behavior of reinforced, confined and fully-grouted masonry, a series of nine half-scale, fully-grouted concrete block masonry assemblages were tested. The first three assemblages were constructed as ordinary, fully-grouted, reinforced masonry. To reflect the proposed strategies described in the current study, the next three assemblages were constructed with a steel base, and the final three were constructed with a steel base and confining plates, as shown in Figure 3.2a. Each of the assemblages had two vertical 10M reinforcing bars (welded to the steel base when present), in addition to one D4 bar of transverse reinforcement every other course. It was noted during assemblage testing that the failure of the unconfined specimens was governed by vertical splitting of the concrete masonry and buckling of the vertical reinforcement (East et al. 2020). This caused premature failure at an average strain of 0.00163 mm/mm for the unconfined assemblages, with

no post-peak performance observed. The confinement prevented this brittle failure in the confined assemblages, with peak strength at an average strain of 0.00196 mm/mm. The stress-strain response of the assemblage tests can be seen in Figure 3.2b.

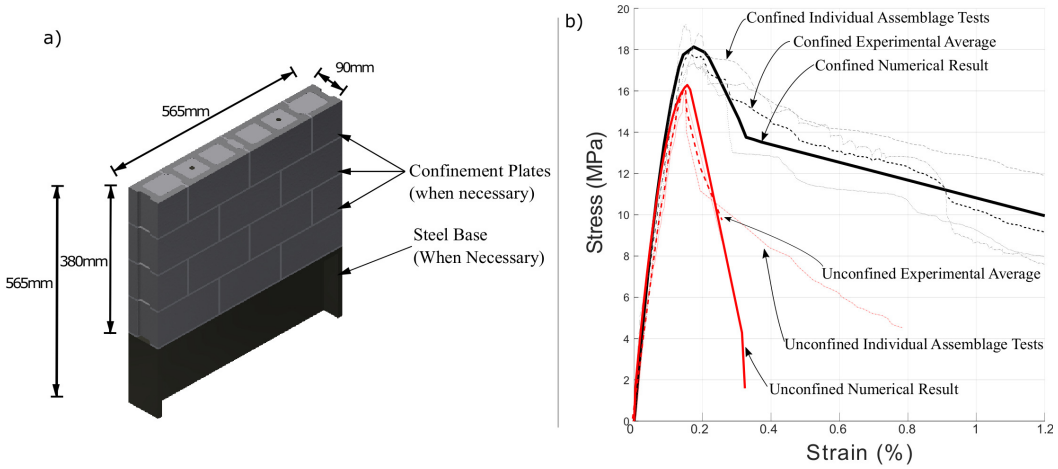

Figure 3.2: Masonry assemblage component-level testing a) assemblage details; and b) experimental and numerical results for confined and unconfined assemblages

Different constitutive relationships were defined for each portion of the cross-section for each of the various layers defined in the element. As the Kent-Park stress-strain relationship is based on an idealized compressive strength (f'_{mi}) corresponding to peak stress at a strain of 0.002 (Priestley and Elder 1983), the expression was modified to reflect the premature failure at 0.00163 mm/mm. The ratio between the idealized compressive strength (f'_{mi}) and the observed compressive strength (f'_{m}) was calculated as 1.035, and this coefficient was used to alter the Kent-Park model. Specifically, the rising curve of the Kent-Park model was modified using Eq. 3.3.1 to incorporate this coefficient, where ε_m represents the compressive strain, and f'm is the ultimate compressive stress (Priestley and Elder 1983). The

strength enhancement coefficient, K, is 1 for unconfined masonry assemblages.

$$\epsilon_m \leq 0.00163K : f_m = 1.035Kf'_m(\frac{2\epsilon_m}{0.002} - (\frac{\epsilon_m}{0.002})^2) \tag{3.3.1}$$

Likewise, the falling branch was modified using Eq. 3.3.2 to reflect the shift in strain from 0.002 to 0.00163 as

$$\epsilon_m > 0.00163K : f_m = 1.035Kf'_m(1 - Z_m(\epsilon_m - 0.00163)) \tag{3.3.2}$$

where Z_m is defined in Eq. 3.3.3 (Priestley and Elder 1983)

$$Z_m = \frac{0.5}{\frac{3+0.29f'_m}{145f'_m-1000} + \frac{3}{4}\rho_s\sqrt{\frac{h"}{s_h}} - 0.00163K} \tag{3.3.3}$$

where ρ_s is the volumetric ratio of the confining steel, while $h"$ and s_h represent the lateral dimension of the confined core and the longitudinal spacing of the confining steel, respectively (Priestley and Elder 1983).

The reinforcing bars were modelled as smeared layers of equivalent thicknesses, designated as PlateRebar following the Giuffre-Menegotto-Pinto model with isotropic strain hardening (referred to as Steel02 in OpenSees). The elastic modulus was taken as 200 GPa, while the strain hardening ratio was set to 1% unless it was otherwise specified (i.e., when using experimental results). The remaining constants of *R0*, *CR1* and *CR2* were set to 18.5, 0.925 and 0.15, respectively.

The model calibration results in Figure 3.2b show that the model can capture the compressive behavior of the confined and unconfined masonry assemblages to a high degree of accuracy, considering the inherent variability

in masonry as a material, with the average peak of the experimental tests being within 2% of the model results for both confined and unconfined masonry assemblages.

In later models developed in this study incorporating PT, the PT bars were modelled using the same Giuffre-Menegotto-Pinto material model, with an initial prestressing force applied. A constant strain hardening ratio of 1.6% was assumed for the PT bars to be consistent with the material properties used in a previous study (Yassin et al., 2020), with *MinMax* material assigned to limit the maximum strains developed in the PT and the reinforcement to 0.15. For PT-CRMWs, the elastic modulus was taken as 190 GPa, while the remaining constants of *R0, CR1* and *CR2* were set as 18, 0.925 and 0.15, respectively.

3.3.3 Material validation

The numerical model developed in the current study was validated against two PT-CRMWs tested by Hassanli et al. (2017), one PT-CRMW tested by Laursen et al. (2004) and one CRMW with flexural yielding energy dissipation devices (ED-CRMW) tested by Yassin et al. (2022b). In the latter, a steel block was used in place of an ordinary concrete masonry unit to allow the ED device to be pinned to the wall. The four walls were selected from a variety of different studies so that the accuracy of the modelling technique could be evaluated across walls with different aspect ratios, loading protocols, PT properties and energy dissipation. The dimensions and details of these four walls are summarized in Table 3.1. For each wall, the initial PT force and the gravity loads (if applicable) were applied, followed by reversed cyclic

horizontal displacements being applied at the top of the wall according to the loading protocol of the experimental program.

Table 3.1: Summary of wall dimensions and PT details used for model validation

Specimen	Thickness (mm)	Length (mm)	Height (mm)	Number of PT bars	PT bar spacing (mm)	PT initial force (kN)	PT Area (mm^2)	ED
W2 (Hassanli et al. 2017)	190	1400	2300	3	600	120	942	No
W3 (Hassanli et al. 2017)	190	1400	2300	4	400	90	1256	No
W3-2 (Laursen et al. 2003)	140	2400	5250	3	400	142	420	No
ED-CRMW (Yassin et al. 2022b)	90[a]	1895	2660	None	N.A.[b]	N.A.	N.A.	Yes[c]

[a]Half scale units were used
[b]N.A.: Not Applicable
[c]Four flexural yielding energy dissipation devices were used

The element size in finite element modelling has a strong impact on the accuracy of the analysis solution. The current study incorporates the crack band theory that was proposed by Bažant (1984) and Jirásek and Bauer (2012) to minimize the effect of the element size. The theory was also used by Lu et al. (2015) with success to model the cyclic response of reinforced concrete shear walls. To utilize this theory, the slope of the softening branch of cracked masonry is proportionally adjusted according to the element size selected, thus leading to identical fracture energy for all elements. To verify the effectiveness of adopting this theory in the current study, models with 128, 288 and 512 elements were constructed and compared to the experimental results of wall W3 tested by Hassanli et al. (2017) as an example. Figure 3.3 shows that this theory was successful in producing nearly identical results for different numbers of elements. The element size that was ultimately used was 87.5 mm wide by 71.875 mm tall, corresponding to the 512-element model in Figure

3.3, as this allowed the unaltered softening branch of the Kent-Park model to be used. This element size was altered by no more than 5% in all models to fit the required geometry of the underlying walls as needed throughout this study.

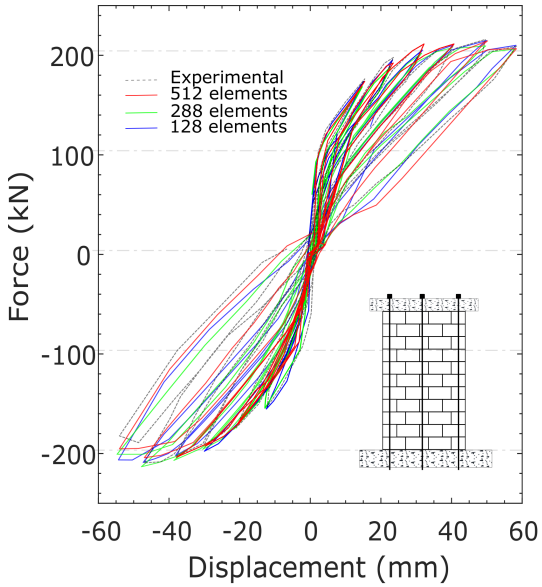

Figure 3.3: Element discretization of Wall W3 (Hassanli et al. 2017)

For all four validation examples, Figure 3.4 shows that there is good agreement between the experimental hysteresis loops, lateral loads, energy dissipation and residual drift when compared to the corresponding OpenSees results. For example, the model is able to capture the peak strength of each cycle within a maximum deviation of 7% for all walls. The deviations observed between the experimental and the model results might be attributed to the inherent variability of the masonry material. Notably, the model maintains comparable accuracy to similar recent studies of PT-CRMWs for hysteretic performance (Hassanli et al. 2017; Kalliontzis and Schultz 2017; Yassin et al. 2020).

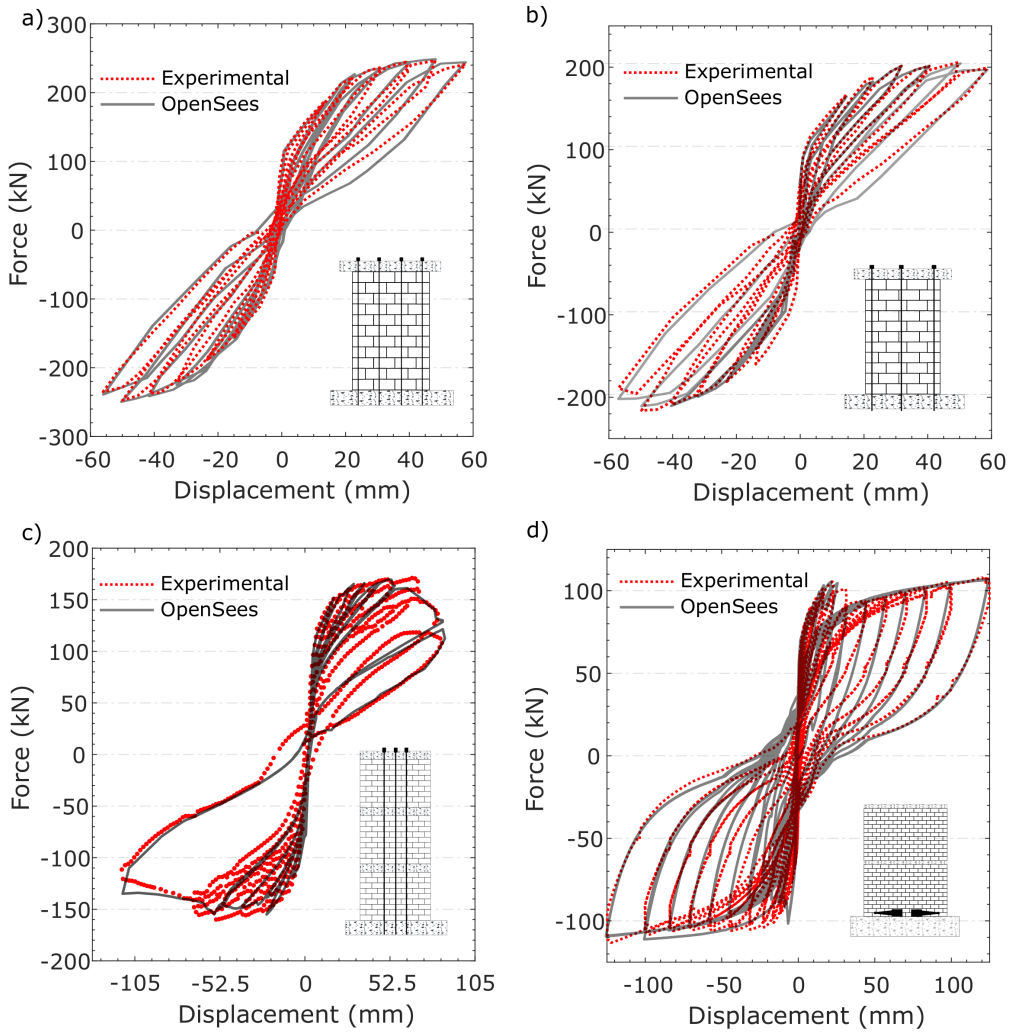

Figure 3.4: Model validation a) W2 (experimental data from Hassanli et al., 2017); b) W3 (experimental data from Hassanli et al., 2017); c) W3-2 (experimental data from Laursen et al., 2002); and d) ED-CRMW (experimental data from Yassin et al., 2022b)

3.4 Damage Index Definition

A damage index was introduced and calibrated by Kim et al. (2005) for reinforced concrete structures based on parametric studies of compression failure modes. The damage index can be extended to all of the walls

considered in this study as they are fully-grouted reinforced masonry walls that behave similarly to reinforced concrete walls. This damage index has been used in further studies for PT-controlled rocking concrete systems by Jafari and Dugnani (2018) but is yet to be used for masonry walls. Therefore, this index was selected in the current study as limited studies have been conducted to develop a damage index for masonry structures. In the damage index, the failure criterion is evaluated using the principal compressive strains as presented in Eq. 3.4.1:

$$DI_c = 1 - f_{tg}\left(\frac{2\epsilon_{mu} - \epsilon_m}{2\epsilon_{mu}}\right)^2 \tag{3.4.1}$$

The damage index ranges from 0 to 1, based on the compressive strains (ϵ_m), the ultimate compressive strain (ϵ_{mu}), and a fatigue parameter (f_{tg}). A damage index value of zero indicates no damage, while a value of one corresponds to maximum damage. The ultimate compressive strain for masonry (ϵ_{mu}) was assumed to be 0.003 (CSA 2014). In cases where confinement is present, the value was assumed to be 0.012 based on recommendations by Priestley et al. (1983) and the tests conducted in this study, as shown earlier in Figure 3.2.

The fatigue parameter in Eq. 3.4.2, f_{tg}, is defined as:

$$f_{tg} = 1 - 0.3b_c \tag{3.4.2}$$

where b_c is the accumulated fatigue damage of masonry based on the number of complete cycles to failure (N_{fc}), as presented in Eqs. 3.4.3 and 3.4.4, these parameters are updated with each step in the analysis, with n

being the most recent analysis step.

$$b_c = \sum_{i=1}^{n} \frac{1}{N_{fci}} \tag{3.4.3}$$

$$log\frac{N_{fc}}{k_c} = \begin{cases} \frac{1}{b}[1 - \frac{(\epsilon_m - \epsilon_{min})^2 - (\epsilon_m - \epsilon_{max})^2}{(\epsilon_m - \epsilon_{min})^2}] & \epsilon_{max} < 0.7\epsilon_m \\ \frac{0.09\epsilon_{mu}}{\epsilon_{mu} - 0.7\epsilon_m} \frac{1}{b} \frac{\epsilon_{max} - \epsilon_{min}}{\epsilon_m - \epsilon_{min}} & \epsilon_{max} \geq 0.7\epsilon_m \end{cases} \tag{3.4.4}$$

where $\epsilon_{max/min}$ are the maximum and minimum cyclic strains obtained up to load step n, b is a material constant that was assumed as 0.0588 (Kim et al. 2005), and k_c was taken as 2 for unconfined masonry and calculated for confined masonry using Eq. 3.4.5 (Kim et al. 2005).

$$k_c = 2\frac{f'_{mconfined}}{f'_{munconfined}} \tag{3.4.5}$$

Kim et al. (2005) also proposed a tensile damage index; however, it was not applicable to the modelling technique used in the current study due to the smeared steel layers in the multi-layer shell element model. For this reason, a new tensile damage index is defined herein to capture shear cracks and tensile splitting damage effects. The tensile DI is defined by Eq. 3.4.6, with ε_{mu} in tension being defined as 0.0002 (CSA (Canadian Standards Association) 2014).

$$DI_T = 1 - \left(\frac{2\epsilon_{mu} - \epsilon_m}{2\epsilon_{mu}}\right) \tag{3.4.6}$$

The total damage index for each element was defined as the larger of the two damages indices presented in Eqs. 3.4.1 and 3.4.6, as shown in Eq. 3.4.7:

$$DI = max(DI_C, DI_T) \tag{3.4.7}$$

3.4.1 Damage state identification

Previous uses of the damage index proposed by Kim et al. (2005) have indicated three primary damage states, as presented in Table 3.2. The three damage states are considered to correspond to the largest damage index defined by Eq. 3.4.7 for every element in the model throughout the loading protocol. Table 3.2 links the damage states proposed by Kim et al. (2005) relating to the damage observed in reinforced concrete structures to the terminology of those proposed in FEMA P-58 (Federal Emergency Management Agency 2018) for masonry structures.

Table 3.2: Damage State Definitions

Damage State	Damage Index Value	Description
DS1 – Minor/repairable damage	$0.1 \leq \text{DI} \leq 0.4$	Hairline cracks, aesthetic compressive damage
DS2 – Moderate damage	$0.4 < \text{DS2} \leq 0.7$	Tensile cracks exceeding 0.1mm, but less than 1 mm, repairable but not insignificant compression failure (face shell spalling/ cracking)
DS3 – Severe damage	$\text{DI} \geq 0.7$	Complete failure (compressive crushing, large tensile cracks exceeding 1 mm in width)

3.4.2 Damage state validation

The damage index described above was validated against the experimental results of the walls outlined earlier in Table 3.1. The highest DI value reached was taken and plotted on the surface of the model to be compared

with the damage reported during the tests. As shown in Figure 3.5, the damage index captures the initiation of crushing at the wall toes (governed by DI_c), as well as the development of diagonal shear cracks (governed by DI_T) at the end of the loading protocol for the walls tested by Hassanli et al. (2017). The exact locations of the diagonal cracks observed based on the damage index model are different than those observed in the tests due to the idealized nature of the smeared multi-layered shell elements used. In the tests, the cracks started at one face joint and propagated through the head and bed joints, whereas the cracks in the model are seen spreading at a diagonal angle from the rocking corners of the wall. This is expected as the bed and head joints are not explicitly modelled. The model also produces much more symmetric results than the experimental tests due to the variability in the experimental specimens resulting in non-symmetric damage as cracks in experimental tests initiate where imperfections are found, while the model lacks such imperfections. In the test by Laursen et al. (2003), wall 3-2 was subjected to unsymmetrical displacements. This can be seen in the hysteretic response shown in Figure 3.4c with one direction exceeding 105 mm of displacement. The damage reported by Laursen et al. (2003) indicated that more damage was observed in one of the wall toes as a result of this. As can be seen in Figure 3.5, the damage index appropriately captured the increased damage in this rocking toe due to the unsymmetrical loading. In the test reported by Yassin et al. (2022b), the outer masonry block was entirely crushed in early cycles, and for the remainder of the test, the wall rocked on the steel block to which the energy dissipation was connected, with no further damage along the wall base. Figure 3.5 shows a similar result from the numerical model, with the outer block being crushed

and no subsequent spread of damage.

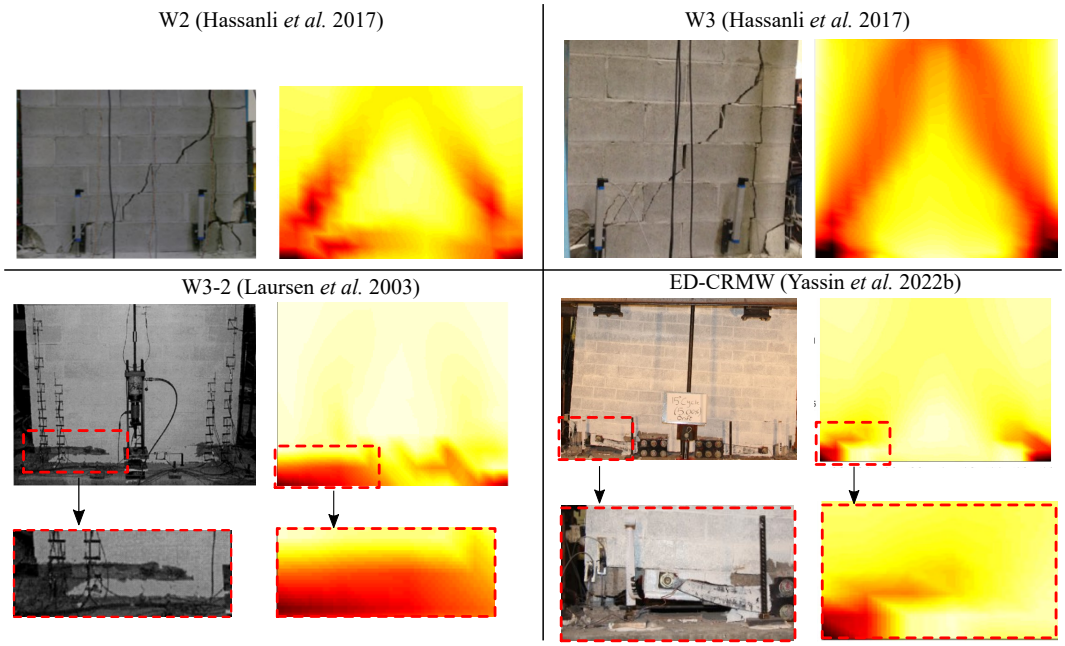

Figure 3.5: Damage index validation compared to the four reference walls at the end of testing

3.5 Enhanced System for Reduced Damage

Following the development and validation of the numerical model to capture various types of CRMWs, the current study proposes a new system that incorporates the three strategies described below and shown in Figure 3.6.

3.5.1 Strategy 1: Externally Mounted Flexural Arms for Energy Dissipation

The first strategy incorporates the flexural arms used in one wall by Yassin et al. (2022b). The device is based on the strong axis bending of a steel cantilever arm. The devices have been tested and modelled under both cyclic

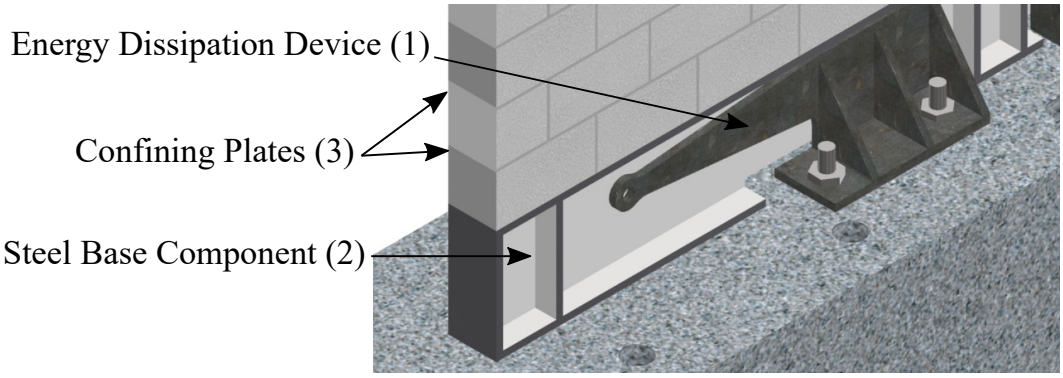

Figure 3.6: Wall construction atop steel base

displacement and axial loading demands to determine key design parameters such as the yield and ultimate strengths, the yield displacement, and how geometric variables influence these parameters. The devices provide supplemental damping to the system, while also resisting the base shear of the wall, thus eliminating the need to provide stoppers at the wall ends or rely on friction between the wall and the foundation. East et al. (2022) and Li (2019) proposed and validated a set of design equations to predict the performance of these devices. Such equations were used in the current study to design archetype walls, as will be discussed later.

3.5.2 Strategy 2: Steel Base

The second strategy involves a steel base to be constructed upon as opposed to the steel block that was used by Yassin et al. (2022b). Constructing atop a steel base component greatly facilitates detailing and installing the proposed energy dissipation device, because bolting the device to steel is more practical than masonry units, as shown in Figure 3.6. The steel base component replaces the bottom few courses of masonry in the proposed walls, thus leaving space for the energy dissipation devices to be installed within the wall footprint, thus

mitigating any architectural issues. In addition, the steel base is expected to reduce damage by selectively providing a stiffer and stronger material than masonry in the highly stressed region of the rocking toe, thereby distributing the compressive stress over a larger area of masonry. Figure 3.6 presents an example of the proposed steel base component along with the flexural yielding energy dissipation device. In this example, the device is pinned to the steel base component, while the other side of the device is bolted to the foundation.

3.5.3 Strategy 3: Toe Confinement

The use of confining plates (also known as Priestley plates) has been shown to enhance the compressive strain capacity of reinforced fully-grouted masonry walls (Priestley & Elder, 1983). These plates have also been used in tests of CRMWs by Laursen et al. (2004) and Yassin et al. (2022b). Including such plates is expected to enhance the performance of the wall by reducing damage in the critical toe region of the wall by significantly increasing the compressive strain capacity. The plates within CRMWs are placed at all bed joints within the rocking toe region, to a depth of 0.2 L_w (wall length) or 1.5 times the neutral axis depth, whichever is larger, based on recommendations by Hassanli et al. (2017).

3.6 Archetype Walls

The current study adopted five buildings from the NIST GCR 10-917-8 study that investigates the FEMA P695 methodology (NIST, 2010). The archetypes were selected to cover a wide range of building heights and design variables. Full details about the structure plans with all dimensions can be found in

Appendix A of GCR 10-917-8 (NIST 2010). Four different versions of each of the five selected archetypes were designed. The first set of walls matched modifications to the NIST designs that incorporated PT tendons outlined by Yassin et al. (2020), classified as PT-CRMWs, and shown in Figure 3.7. The remaining archetypes relied on gravity loads for self-centering and incorporated the proposed energy dissipation devices. The second set of walls, classified as ED-CRMWs in Figure 3.7, incorporates strategy 1. The third set, classified as EDS-CRMWs in Figure 3.7, incorporates strategies 1 and 2. The fourth set, classified as EDSC-CRMWs in Figure 3.7, incorporates strategies 1, 2 and 3.

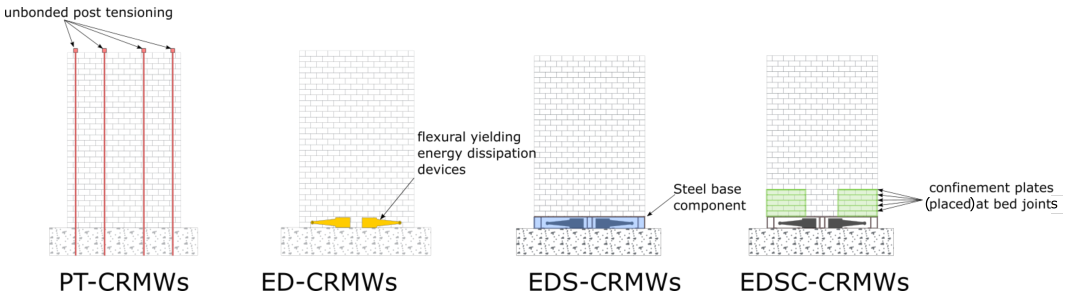

Figure 3.7: Archetype walls

3.6.1 Design criteria

The PT-CRMWs were detailed in accordance with the requirements of TMS (MSJC 2013). A minimum amount of vertical reinforcement (ρ_v) was used over the height of each wall to maintain engineering practice requirements according to TMS (MJSC 2013). The horizontal reinforcement (ρ_h) was identical for all walls to satisfy shear strength requirements as per the design outlined in the NIST GCR 10-917-8 study (NIST 2010). All the walls were designed to self-center while having the PT remain elastic at the ultimate stage outlined in detail by Yassin et al. (2020). The one- and two-story PT-CRMWs used

strands with a yield stress of 850 MPa and a prestress ratio of 0.25, while the 4-, 8- and 12-story PT-CRMWs used bars with a yield stress of 1680 MPa and a prestress ratio of 0.5.

For the design of ED-CRMWs, EDS-CRMWs and EDSC-CRMWs, the design equations presented by Hassanli et al. (2017) for PT-CRMWs were modified to incorporate the expressions regarding the flexural energy dissipation devices that were developed by East et al. (2022), resulting in Eq. 3.6.1 - 3.6.3.

$$a = \frac{F_y + P_u/\phi}{0.8 f'_m t_w} \tag{3.6.1}$$

$$F_y = \frac{4}{27}\frac{b^2 t \sigma_y}{h} \tag{3.6.2}$$

$$M_n = F_y(d - \frac{a}{2}) + \frac{P_u}{\phi}(L_w - \frac{a}{2}) \tag{3.6.3}$$

where a is the equivalent stress block depth, φ is the strength reduction factor (0.8), f'_m is the compressive strength of the masonry, and t_w is the wall width; b, t and h are the maximum depth, thickness and engaged length of the flexural arm, respectively, while σ_y is the yield stress of the steel used for the flexural arms; L_w and d are the length of the wall and the distance of the flexural arm from the end of the rocking toe of the wall. Tables 3.3 and 3.4 summarize the key design parameters of the PT and ED archetype walls used in the current study, respectively. The wall designs and IDs in Table 3.3 are the same as those used by Yassin et al. (2020). For the ED archetype walls, the relevant design parameters outlined in Table 3.4 were selected to achieve

the same ultimate lateral strength as the PT archetype of the same height to facilitate direct comparison. When 8 ED devices are used, the additional devices are placed closer to the centerline of the wall, resulting in multiple d values being used in Eq. 3.6.3.

Table 3.3: PT-CRMW archetype walls

Archetype ID	Height (mm)	Length (mm)	Thickness (mm)	PT Area (mm^2)	ρ_v (%)	ρ_h (%)
PT1	3657	7315	203	5x124	0.046	0.085
PT2	6096	9754	203	4x140	0.041	0.180
PT3	12192	9754	203	2x251	0.041	0.127
PT4	24384	9754	203	4x1018	0.041	0.082
PT5	36576	9754	305	7x1018	0.026	0.107

Table 3.4: Alternative CRMW archetypes

Archetype ID	Height (mm)	Length (mm)	Thickness (mm)	ρ_v (%)	ρ_h (%)	b (mm)	t (mm)	h (mm)	F_y (kN)	d (mm)
ED/EDS/EDSC1	3657	7315	203	0.046	0.085	145	25.4	450	141	7165
ED/EDS/EDSC2	6096	9754	203	0.041	0.180	145	25.4	550	115	9600
ED/EDS/EDSC3	12192	9754	203	0.041	0.127	145	25.4	550	115	9600
ED/EDS/EDSC4	24384	9754	203	0.041	0.082	200	38.1	400	452	9604/8954[a]
ED/EDS/EDSC5	36576	9754	305	0.026	0.107	235	38.1	315	792	9604/9039[a]

[a]Indicates 8 flexural arms were used, with the second set placed closer to the center of the wall

3.6.2 Numerical modelling

The model presented earlier in Figure 3.1 was used to model the archetype walls presented in Tables 3.3 and 3.4. For the EDS-CRMW and EDSC-CRMW models, the bottom masonry elements were instead modelled as ElasticMembranePlateSection shell elements with assigned linear elastic steel properties. For the EDSC-CRMW models, the confined core of the cross-section was updated in accordance with Eqs. 3.3.1 – 3.3.3.

3.6.3 Loading protocol

The archetype walls were all subjected to the same cyclic loading protocol based on ASTM E2126 method B (ASTM 2009), as shown in Figure 3.8. Five single fully-reversed cycles at displacement amplitudes of 1.25, 2.5, 5, 7.5 and 10% of the ultimate displacement of the wall were initially applied (as obtained from a pushover analysis). Then, two fully-reversed cycles at displacements of 20, 40, 60, 80 and 100% of the ultimate displacement were applied until failure occurred when the wall reaches 20% strength degradation. The loading protocol was completed to the load cycles shown in Figure 3.8, unless failure was recorded in elements due to strain exceedance using *MinMax* material.

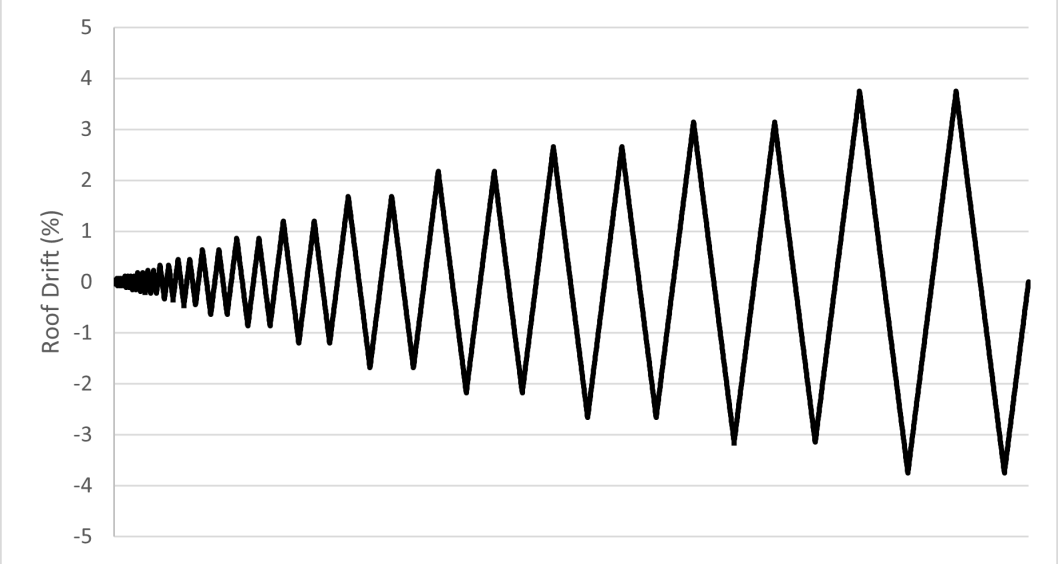

Figure 3.8: Loading Protocol

3.7 Application of Damage Index to Archetype Walls

To illustrate the analysis results, Figures 3.9 and 3.10 show the damage index of archetype walls 2 (two stories) and 3 (four stories), respectively. Each of the design alternatives is included, namely PT, ED, EDS and EDSC, following the IDs that were identified in Tables 3.3 and 3.4. The top plot displays the backbone envelopes from the cyclic pushover analysis. Below that graph, the damage index is plotted on each wall's surface at three critical drift levels, taking the PT-CRMW archetypes as a reference point: a drift of 0.32% (representative of the first complete drift cycle following the uplift of the PT wall), the drift corresponding to the peak force of the PT wall (1.35% for archetype 2 and 0.85% for archetype 3), and the drift associated with a 20% strength degradation of the PT wall (3.03% for archetype 2 and 3.38% for archetype 3).

3.7.1 Two-Story archetype

At the first drift level presented in Figure 3.9 (0.32%), wall PT2 is observed to have a considerable amount of toe crushing already, characterized by DIC values exceeding 0.7 (DS3) concentrated at the rocking toes, due to the high compressive loads imposed by the PT tendons. Wall PT2 also exhibits zones of high diagonal tension at the first drift level, characterized by the diagonal DIT values exceeding 0.7 (DS3) spreading at a 45-degree angle from the rocking toes into the center of the wall. At the same drift level, wall ED2 has evidence of toe crushing initiation (with a peak DIc exceeding 0.7) though

considerably less than that of wall PT2. Both EDS2 and EDSC2 experience negligible damage at the first drift level. As shown in Figure 3.9, the second drift level (1.35%) shows a progression of toe crushing in wall PT2 as the rocking point shifts inward, accompanied by more prominent diagonal tension damage that would correspond to diagonal shear cracks propagating through the joints (maximum DI_T of 0.61). Conversely, wall ED2 experiences significant toe crushing (DI_C exceeds 0.7 in multiple elements), but considerably less diagonal tension damage. The steel base included in EDS2 avoids any of the elements reaching an overall DI of 0.39 or higher; however, minor damage (DI between 0.1 and 0.4) is visible at this stage. Wall EDSC2, with confining plates, has slightly less damage than wall EDS2, with the largest DI recorded being 0.34. At the final stage, corresponding to 20% strength degradation in wall PT2, Figure 3.9 shows that the diagonal shear cracks have increased in wall PT2; however, only a slight increase in damage is observed between the peak load and the load corresponding to 20% strength degradation, with a peak DI_T of 0.66. This drift level corresponds to 27% strength degradation of ED2, so increased damage and complete crushing of the entire rocking toe region are observed. EDS2 and EDSC2 showed only a minor increase in observed damage relative to the previous stage, with the toe region of wall EDS2 reaching a DI of 0.42 (crossing the threshold for moderate damage), while the toe region of wall EDSC2 remains below 0.4 at a value of 0.39. A reduction in strength of only 3.5 and 6.8% is observed at this drift level for EDS2 and EDSC2, respectively, attributed to the large displacement capacity of the devices, and the slight decrease in capacity at larger displacements due to the compressive load carried by the devices.

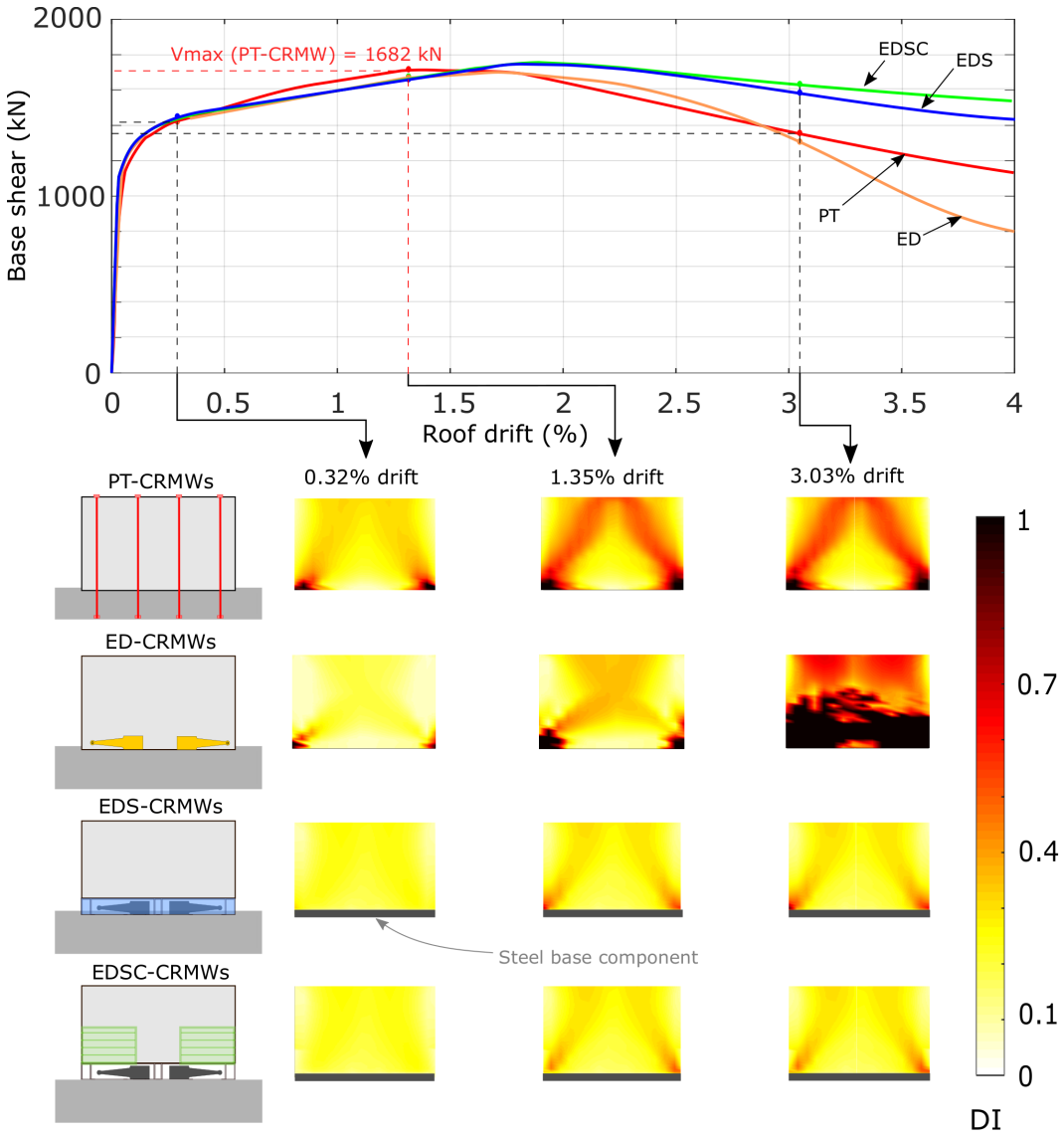

Figure 3.9: Damage Index for archetype wall 2 at various cumulative cyclic drift levels

3.7.2 Four-Story archetype

Figure 3.10 displays generally similar trends across the 4-story archetype as was observed in Figure 3.9 with the 2-story archetype. At the first drift level, wall PT3 has moderate damage at the rocking toes (DIC values reaching 0.51), while walls ED3, EDS3 and EDSC3 all display minor damage at this drift level,

with maximum DI values of 0.32, 0.29 and 0.29 respectively. At the peak drift level (0.85%), PT3 experiences increased crushing in the rocking toe region, while diagonal cracks have started forming in the corners, with DI_T and DI_C exceeding 0.4 and 0.7, respectively. Reduced toe crushing is observed in ED3, with DIC remaining below 0.4, but with moderate diagonal cracks comparable to PT3 being visible as well, corresponding to DI_T exceeding 0.4. In EDS3 and EDSC3, an increase in damage at the rocking toes is observed at the peak drift level relative to lower drifts of the same walls, but no signs of crushing, with all DI values remaining well below 0.4. The final drift level shows increased damage in PT3 and ED3, with 20% and 16% strength degradation observed at this drift, respectively. Both walls have a crushed rocking toe (DI_C exceeding 0.7), whereas EDS3 and EDSC3 experience moderate damage (DI_C less than 0.39) and only experience a strength degradation of 2% and 7%, respectively.

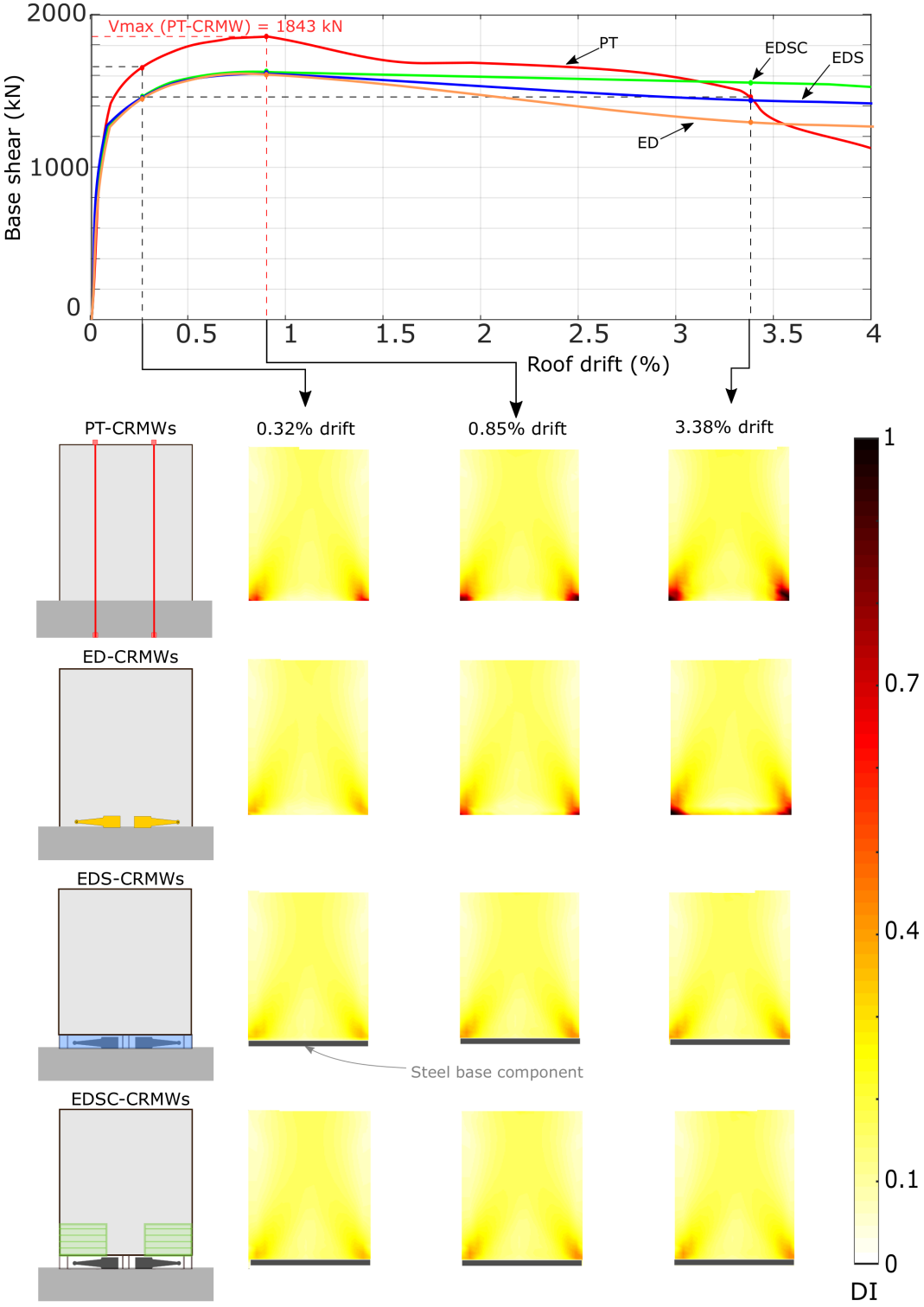

Figure 3.10: Damage Index for archetype wall 3 at various cumulative cyclic drift levels

3.7.3 Overall Archetype Results

In both examples presented in Fig. 3.9 and 3.10, and in the other archetype walls examined with 1, 8 and 12 stories, most of the damage was observed in the first story of the wall. As such, Figure 3.11 displays the damage index of all the archetypes (i.e., 20 walls) at the ultimate force of each wall. In the single-story archetype walls, the PT and ED walls experience a similar degree of toe crushing and diagonal shear damage. The EDS and EDSC walls reduce the amount of toe crushing, with DI_C remaining below 0.7; however, the diagonal tension damage is not eliminated. In the 2- and 4-story archetype walls, the same trend is observed with respect to the reduction in toe crushing, corresponding to DI_C exceeding 0.7 over a reduced area of the wall, while the ED, EDS and EDSC walls experienced less diagonal damage. The confinement present in the EDSC walls also reduces the damage within the toes of the EDSC walls.

As shown in Figure 3.11, while the enhanced system incorporating all three strategies is highly effective at mitigating damage for low-rise structures, with minimal damage observed in the 1-, 2- and 4-story archetypes, there is considerably more damage for the 8- and 12-story structures. The additional damage observed in these taller archetypes is due to the larger amount of PT or ED forces required in the design procedure to meet the base shear demands. This is because the moment resistance added by the flexural arms scales based on horizontal distance to the rocking toe, and the length did not increase across archetypes 2-5 while the height increased considerably. This results in a less practical design for the flexural yielding devices, as the moment arm for the devices could not be increased

(and it even decreased for the devices placed closer to the center of the wall when multiple sets of arms were used) while the height increased.

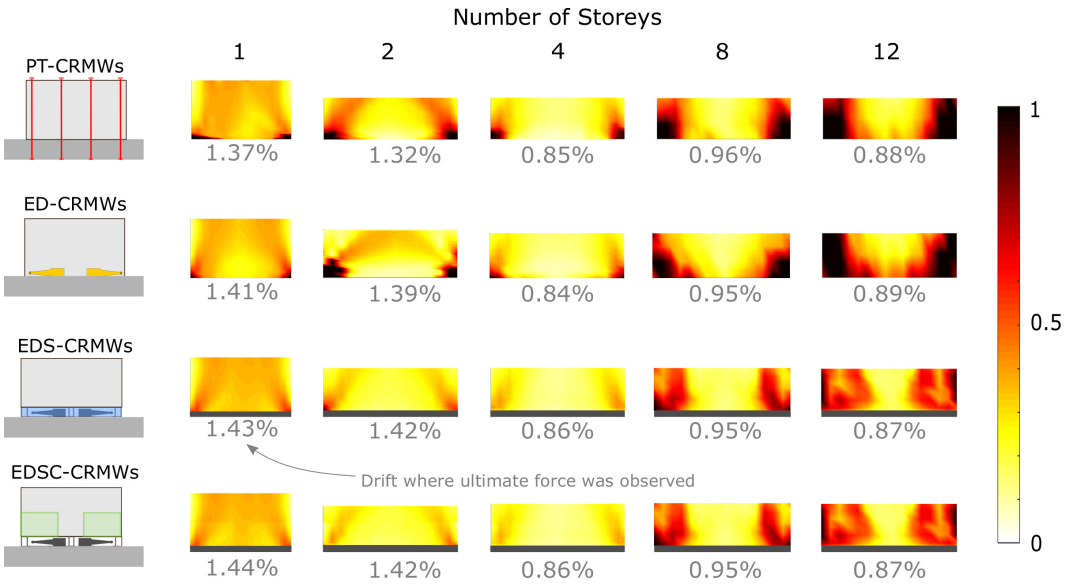

Figure 3.11: Damage index at peak load for the first story of each archetype wall

To normalize the results for each archetype wall regardless of the number of stories, the overall percentage of the first story (where the majority of the damage was observed) exceeding each damage state from Table 3.2 is plotted against the peak roof drift throughout the analysis of each wall in Figure 3.12. The bolded line is the average for each set of archetype walls. For DS1, corresponding to minor/repairable damage, both the PT walls and the ED walls reach nearly 100% of the first story being damaged prior to 1.5% roof drift. An improvement is observed with the EDS and EDSC walls, where the average damage reduces to 84% and 79% of the first story exceeding DS1 for the EDS and EDSC walls, respectively. The observed damage in DS2 is reduced by a larger margin, from 57% and 56% of the first-story area in the PT and ED-CRMWs to 8% in the EDS and EDSC archetypes, with no significant

improvement observed as a result of the confinement plates. DS3 shows the most substantial benefit to implementing the proposed strategies, with the alternative walls incorporating all three strategies experiencing as low as 0% of the first story exceeding DS3, compared to an average of 30% in the PT archetypes.

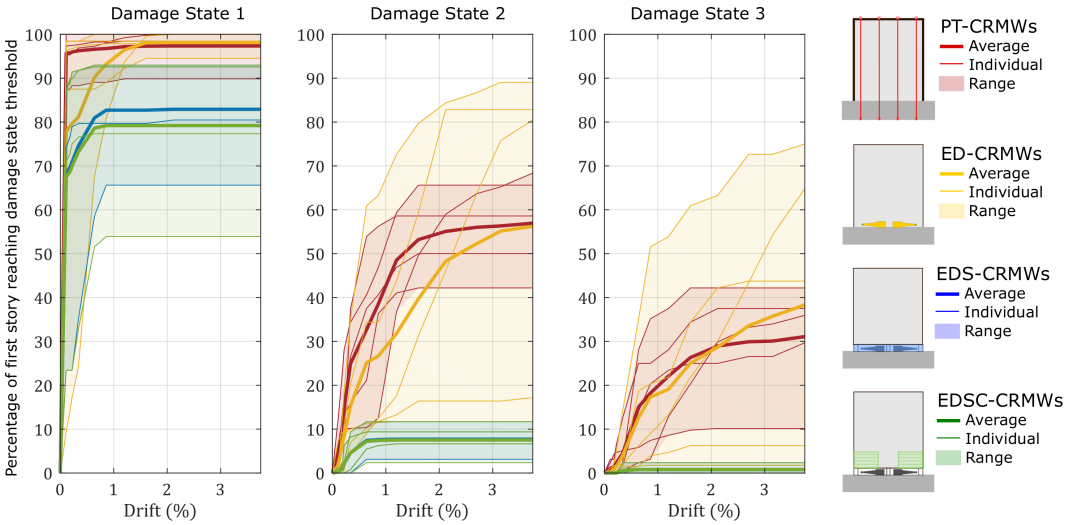

Figure 3.12: Damage State Curves

3.8 Conclusions

The current study proposed using three strategies to enhance the performance of CRMWs, namely externally mounted supplemental energy dissipation devices, a steel base component, and confining plates in the rocking toe region. The energy dissipation devices address the low inherent damping of CRMW systems, while adding the ability to inspect and replace the devices if needed following seismic events. Furthermore, the devices also eliminate the need for stoppers to resist sliding. The use of the steel base eases detailing and architectural considerations as well as reduces damage.

The confining plates in the rocking toe region further reduce damage by increasing the compressive strain capacity of the masonry in this critical region of the wall. A nonlinear finite element model and damage index were also created and validated to capture the behavior and damage of CRMWs. This model and damage index were then used to assess the damage incurred on a suite of 20 archetype walls, and subsequently to examine the effectiveness of these three strategies collectively in comparison to a more conventional PT-CRMW system. The results of the study are summarized as follows:

- The proposed modelling technique of using multi-layered shell elements is very effective at capturing the overall response of CRMWs, consistently producing results that are within 7% of the peak force measured in experimental tests.
- The proposed damage index is capable of quantifying damage in CRMWs, particularly in identifying crushing damage at the rocking toes and the development of diagonal tension cracks.
- The proposed CRMW system incorporating all three strategies shows promising results for reducing damage in CRMWs, with severe damage being almost entirely eliminated in the critical regions of the walls.

While future experimental studies will be essential to validate the proposed CRMW wall system, the numerical work presented in this study indicates that the proposed system has the potential to be a high-performance seismic force-resisting system with extremely low damage.

3.9 Acknowledgements

Support for this project was provided through the Canadian Concrete Masonry Producers Association (CCMPA), the Canada Masonry Design Centre (CMDC), the Natural Sciences and Engineering Research Council (NSERC), and the Ontario Centres of Excellence (OCE).

3.10 References

ACI Innovation Task Group 5. 2009. "Requirements for Design of a Special Unbonded Post-Tensioned Precast Shear Wall Satisfying ACI ITG-5.1 (ACI ITG-5.2-09) and Commentary." American Concrete Institute, 1: 1–21.

ASTM. 2009. "Standard Test Methods for Cyclic (Reversed) Load Test for Shear Resistance of Vertical Elements of the Lateral Force Resisting Systems for Buildings 1 (E2126)." ASTM.

Bazant, Z. P. 1984. "Size effect in blunt fracture: concrete, rock, metal." Journal of Engineering Mechanics 110(4): 518-535.

CSA (Canadian Standards Association). 2014. Design of masonry structures. CSA S304-14. Mississauga, ON, Canada

Dvorkin, E. N., D. Pantuso, and E. A. Repetto. 1995. "A formulation of the MITC4 shell element for finite strain elasto-plastic analysis." Computer Methods in Applied Mechanics and Engineering, 125 :1–4. https://doi.org/10.1016/0045-7825(95)00767-U.

East, M., M. Ezzeldin, and L. Wiebe. 2020. "Numerical modelling of a confinement system for controlled rocking masonry wall toes." 17th World Conference on Earthquake Engineering. Sendai: 17th World Conference on Earthquake Engineering.

East, M., Li, J., M. Ezzeldin, and L. Wiebe. 2022. "Development of a Flexural Yielding Energy Dissipation Device for Controlled Rocking Systems." Journal of Structural Engineering. https://doi.org/10.1061/(ASCE)ST.1943-541X.0003461

Eguchi, R. T., J. D. Goltz, C. E. Taylor, S. E. Chang, P. J. Flores, L. A. Johnson, H. A. Seligson, and N. C. Blais. 1998. "Direct economic losses in the Northridge earthquake: A three-year post-event perspective." Earthquake Spectra, 14 (2): 245-264. https://doi.org/10.1193/1.1585998.

El-Hashimy, T., Ezzeldin, M., Tait, M., & El-Dakhakhni, W. (2019). "Out-of-plane performance of reinforced masonry shear walls constructed with boundary elements". Journal of Structural Engineering, 145(8): 04019073.

Federal Emergency Management Agency (FEMAP-58). 2018. "Volume 5 – Expected Seismic Performance of Code-Conforming Buildings." Fema P-58, 5 (December).

Guan, H., and Y.-C. Loo. 1997. "Flexural and Shear Failure Analysis of Reinforced Concrete Slabs and Flat Plates." Advances in Structural Engineering, 1 (1): 71-85. https://doi.org/10.1177/136943329700100108.

Hallinan, P., and H. Guan. 2007. "Layered finite element analysis of one-way and two-way concrete walls with openings." Advances in Structural Engineering, 10 (1): 55-72. https://doi.org/10.1260/136943307780150850.

Hassanli, R., M. A. ElGawady, and J. E. Mills. 2017. "In-plane flexural strength of unbonded post-tensioned concrete masonry walls." Engineering Structures. 136: 245-260. https://doi.org/10.1016/j.engstruct.2017.01.016.

Jafari, A., and R. Dugnani. 2018. "Estimation of Load-Induced Damage and Repair Cost in Post-Tensioned Concrete Rocking Walls." Journal of Shanghai Jiaotong University (Science), 23 (1): 122-131. https://doi.org/10.1007/s12204-018-1917-x.

Jirásek, M., and Bauer, M. 2012. "Numerical aspects of the crack band approach." Computers & Structures 110: 60-78.

Kalliontzis, D., and A. E. Schultz. 2017. "Characterizing the In-Plane Rocking Response of Masonry Walls with Unbonded Posttensioning." Journal of Structural Engineering, 143 (9): 04017110. https://doi.org/10.1061/(ASCE)ST.1943-541X.0001838.

Kim, T. H., K. M. Lee, Y. S. Chung, and H. M. Shin. 2005. "Seismic damage assessment of reinforced concrete bridge columns." Engineering Structures, 27 (4): 576-592. https://doi.org/10.1016/j.engstruct.2004.11.016.

Laursen, P. T., and J. M. Ingham. 2004. "Structural Testing of Large-Scale Posttensioned Concrete Masonry Walls." Journal of Structural

Engineering, 130 (10): 1497. https://doi.org/10.1061/(asce)0733-9445(2004)130:10(1497).

Li, J. 2019. "Development of a Flexural Yielding Energy Dissipation Device for Controlled Rocking Masonry Walls." *MASc Thesis.* McMaster University.

Lu, X., X. Lu, H. Guan, and L. Ye. 2013. "Collapse simulation of reinforced concrete high-rise building induced by extreme earthquakes." Earthquake Engineering and Structural Dynamics, 42 (5): 705-723. https://doi.org/10.1002/eqe.2240.

Lu, X., L. Xie, H. Guan, Y. Huang, and X. Lu. 2015. "A shear wall element for nonlinear seismic analysis of super-tall buildings using OpenSees." Finite Elements in Analysis and Design, 98: 14-25. https://doi.org/10.1016/j.finel.2015.01.006.

Mazzoni, S., F. McKenna, M. H. Scott, and G. L. Fenves. 2006. "OpenSees command language manual." Pacific Earthquake Engineering Research Center, (February).

MSJC. 2013. "Building Code Requirements and Specification for Masonry Structures." Masonry Standards Joint Committee.

NIST (National Institute of Standards and Technology). 2010. Evaluation of the FEMA P-695 Methodology for Quantification of Building Seismic Performance Factors (NIST GCR 10-917-8). Gaithersburg, MD.

Priestley, M., and D. Elder. 1983. "Stress-Strain Curves for Unconfined and Confined Concrete Masonry." ACI Journal Proceedings, 80 (3): 192-201.

https://doi.org/10.14359/10834.

Rosenboom, O. A., and Kowalsky, M. J. (2004). "Reversed in-plane cyclic behavior of posttensioned clay brick masonry walls." Journal of Structural Engineering, 10.1061/(ASCE)0733-9445(2004)130:5(787), 787–798.

Wight, G. D., and J. M. Ingham. 2006. "Seismic performance of a post-tensioned concrete masonry wall system." Doctoral Dissertation. University of Aukland

Yassin, A., M. Ezzeldin, T. Steele, and L. Wiebe. 2020. "Seismic Collapse Risk Assessment of Posttensioned Controlled Rocking Masonry Walls." Journal of Structural Engineering, 146(5): 04020060. https://doi.org/10.1061/(ASCE)ST.1943-541X.0002599.

Yassin, A., M. Ezzeldin, and L. Wiebe. 2022a. "Experimental Assessment of Controlled Rocking Masonry Shear Walls without Post-tensioning." Journal of Structural Engineering, 148(4): 04022018. https://doi.org/10.1061/(asce)st.1943-541x.0003307.

Yassin, A., Ezzeldin, M., and Wiebe, L. (2022b). "Experimental Assessment of Resilient Controlled Rocking Masonry Walls with Replaceable Energy Dissipation." Journal of Structural Engineering, (Submitted).

Chapter 4

Development of Controlled Rocking Masonry Walls with Energy Dissipation Accessible in a Steel Base

4.1 Abstract

Recent studies have investigated the seismic response of controlled rocking masonry walls (CRMWs) that rely on gravity loads for self-centering and on supplemental energy dissipation (ED) devices to control the response (ED-CRMWs). However, such studies reported that some limitations still exist due to ED devices being installed inside the wall, making repairs difficult or impossible following the yielding or fracturing of such devices. For these reasons, the current study develops a new system, namely controlled rocking masonry walls with Energy dissipation Accessible in a Steel base (EASt-CRMWs). In this system, walls are constructed upon a steel rocking base to allow for the installation of ED devices within the footprint of the wall. In addition, these ED devices are in the form of externally-mounted cantilevered steel flexural yielding arms that can be easily replaced following

a seismic event. To investigate the seismic response of the new system, the study reports the experimental results of six EASt-CRMWs tested under displacement-controlled quasi-static cyclic fully-reversed loading. Various design parameters are investigated herein, including the axial load, aspect ratio, vertical reinforcement, confinement technique, and size of the flexural arms. The experimental results are presented in terms of the force-displacement responses, residual drift ratios, and damage patterns including the use of digital image correlation techniques. Using such results, iterative and simplified procedures are developed and validated to predict the monotonic force-displacement responses of the test walls. The experimental results show that the use of a steel rocking base considerably enhanced the seismic response of the walls by protecting their rocking toes at large drift ratios. Specifically, extremely low damage was observed at the end of the tests, where five walls reached drift ratios up to 4.0% with no strength degradation and with residual drifts of less than 0.1%. The vertical reinforcement and confinement properties of the rocking toes had almost no influence on the cyclic response of the test walls; however, the axial load, aspect ratio, and amount of ED altered their responses. The two prediction procedures were also able to simulate the monotonic responses of the walls at all displacement ranges. With these results, the current study demonstrates that the proposed EASt-CRMWs are expected to be a resilient system within the masonry construction practice by achieving low damage and rapid recovery following seismic events.

4.2 Introduction

Early experimental studies on controlled rocking systems by Erkmen and Schultz (2009) and Priestley and Tao (1993), during the Precast Seismic Structural Systems (PRESSS) program, showed promising results for self-centering concrete wall systems. Such studies reported that controlled rocking precast concrete walls could achieve enhanced seismic performance with only minor damage and minimum residual displacements. These research efforts have led to design guidelines for seismic force-resisting systems that rely on special unbonded post-tensioned (PT) precast concrete shear walls (ACI Innovation Task Group 5 2009). Moreover, significant steps were taken by several researchers to investigate the response of controlled rocking systems applied to masonry walls (Laursen and Ingham 2004; Rosenboom and Kowalsky 2004; Wight and Ingham 2006; Toranzo et al. 2009; Hassanli et al. 2016, 2017; Yassin et al. 2020). For example, Laursen and Ingham (2004) tested six fully-grouted controlled rocking reinforced masonry walls. These walls relied on PT tendons that were placed through the walls to provide restoring forces, returning the wall to return to its original alignment following seismic events. While being able to withstand large drifts up to 1%, damage was observed at drifts exceeding 1% at the rocking toes due to the brittle nature of masonry walls in comparison to reinforced concrete shear walls. The study also reported that the installation of the PT tendons complicated the construction, and ultimately led to poor performance in terms of deformation capacity due to a combination of PT losses and the additional compression placed on the masonry rocking toes. Further studies by Rosenboom and Kowalsky (2004) and Hassanli et al.

(2016, 2017) reported similar conclusions to those by Laursen and Ingham (2004). The use of energy dissipation (ED) devices was also recommended to address the low damping of the system due to the walls remaining mostly elastic compared to conventional masonry systems with fixed bases (Hassanli et al., 2017).

These conclusions led to a recent study by Yassin et al. (2022a) that omitted PT tendons and relied instead on gravity loads to self-center the walls and and ED devices to control their peak displacements. In Yassin et al. (2022a), six controlled rocking masonry walls with internal, axial yielding energy dissipation devices (ED-CRMWs) were tested. The study also investigated the use of confining plates and end boundary elements to reduce damage at the rocking toes of the test walls, as recommended in previous studies (Laursen et al. 2004; Shedid et al. 2009, 2011; Banting and El-Dakhakhni 2014; Ezzeldin et al. 2017). These ED-CRMWs were able to withstand large displacements with low residual displacements; however, since the ED devices used by Yassin et al. (2022a) were located inside the wall, such devices are inaccessible for repairs following seismic events. To address this, more recent studies have been conducted to develop an externally-mounted ED device using a steel flexural arm that can easily be replaced following seismic events (Li 2019; East et al. 2022). The studies have experimentally and numerically investigated the performance of such steel flexural arms and established design equations that can be used to incorporate them into CRMW systems (Li 2019; East et al. 2022). Following this, a single wall was tested by Yassin et al. (2022b), where steel flexural arms at the base of the wall were connected to the wall through special prefabricated steel blocks. In order to connect the arms to the foundation,

thick steel plates were required to be cast in the foundation while it was being poured. The results were promising, with only minor damage being observed at the rocking toe up to a drift ratio of 1%, and no strength degradation up to a drift ratio of 5%. This recent study indicated three main limitations to be addressed in future research studies. First, only a single wall was tested, and therefore, more wall tests with other configurations are essential to better understand the performance of the system. Second, the prefabricated steel blocks led to several detailing and construction challenges, and thus, alternative methods for connecting the flexural arms to the wall are still needed. Third, the arms extended outside the footprint of the wall, leading to architectural issues in practical construction.

The current study develops a new system, namely controlled rocking masonry walls with Energy dissipation Accessible in a Steel base (EASt-CRMWs), to address the aforementioned limitations. Similar to ED-CRMWs, this system omits PT and relies on gravity loads and steel flexural arms to control the seismic response; however, the use of a steel base is expected to further reduce damage by providing a stiffer and stronger material than masonry in the highly stressed regions at the rocking toes of the wall. From a practical perspective, the EASt-CRMW system places the flexural arms within the footprint of the wall, thus reducing the architectural implications of extrusions at the base of the walls. This system also allows for an unaltered, standard construction practice to be maintained for both the foundation crews and the masons as the steel detailing requirements are performed separately from their workflow.

In this respect, the current study presents the experimental results of six

EASt-CRMWs tested under displacement-controlled quasi-static cyclic fully-reversed loading in order to quantify the seismic performance of the new system with different design parameters, including the confinement technique in the rocking toes, vertical reinforcement ratio, axial load level, aspect ratio, and amount of ED. Thereafter, the study develops two procedures to predict the monotonic force-displacement responses of the EASt-CRMWs system. The first is an iterative procedure that employs sectional analysis at the cross-section above the steel rocking component near the base of the wall, while the second is a simplified procedure that is based on equivalent stress block simplifications to the compression stresses at the rocking toes directly atop the steel base component.

4.3 Experimental Program

4.3.1 Test Matrix

As shown in Figure 4.1, all the walls were two stories tall with a height of 2660 mm, corresponding to a height of 5600 mm in full-scale. The walls were constructed by a professional mason using half-scale concrete block units (90 x 90 x 185 mm), which are true replicas of the full-scale blocks (190 x 190 x 390 mm) widely used in North America. The joints were scaled to 5 mm and constructed using a 50% running bond. To accommodate the horizontal reinforcement, the webs of the masonry units were notched to a depth of 20 mm.

Table 4.1 summarizes the geometrical configurations and reinforcement details of the six EASt-CRMWs that were tested. Wall 1 serves as a reference

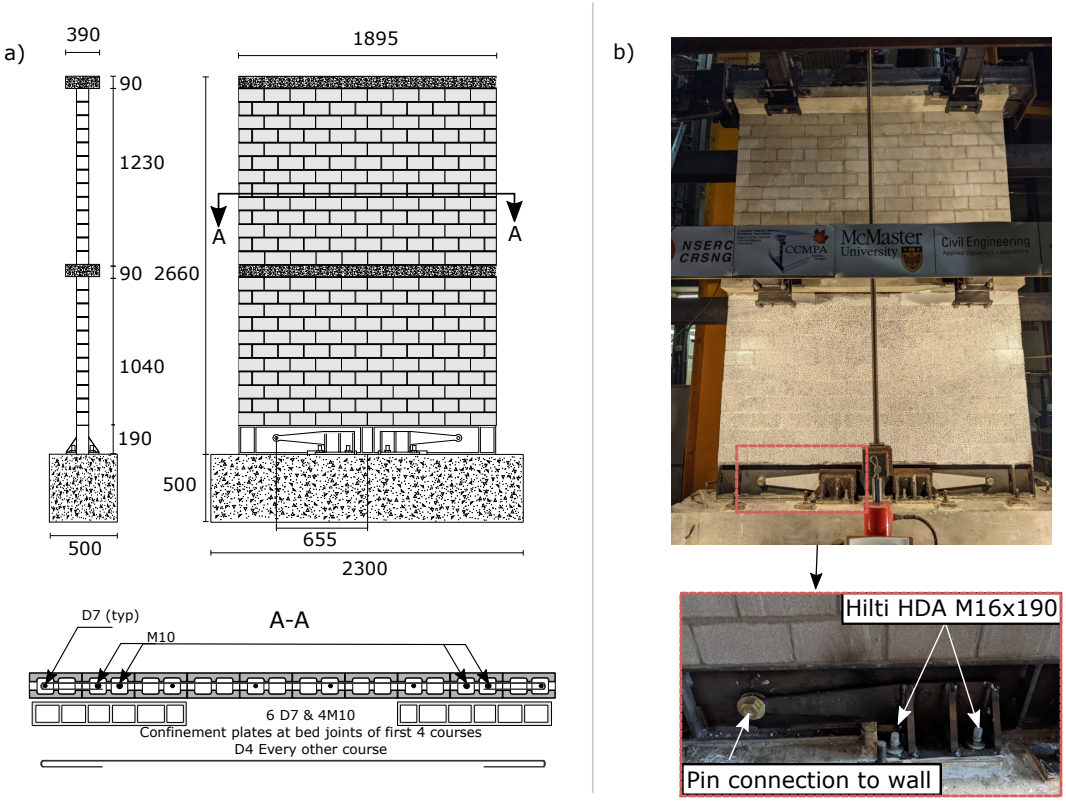

Figure 4.1: a) Typical wall geometry (all dimensions are in mm); and b) Photo of a wall prior to testing, with details of the energy dissipation installation

wall for the experimental program and was designed to have the same overall geometry and lateral yield strength as the ED-CRMWs tested by Yassin et al. (2022b). As such, four flexural arms were used, two on each side placed symmetrically, as shown in Figure 4.1a. The flexural arms have an engaged length of 315 mm and a thickness of 15.88 mm, and were cut from grade 44W steel using a water jet cutter. The arms have design yield and ultimate forces of 23.6 kN and 49.1 kN, respectively, calculated as described later. Each of the flexural arms was connected to the foundation using two Hilti HDA M16-190 undercut anchors, as shown in Figure 4.1b, and were pinned to the wall at a distance of 655 mm from the wall centerline. The reinforcement was

primarily intended to preserve integrity during rocking and to satisfy the standard requirements for seismic detailing. As such, the reinforcement of Wall 1 was selected according to the minimum reinforcement requirements outlined in TMS (2016), with larger vertical bars placed above the locations of the flexural arms to facilitate load transfer into the wall. The vertical reinforcement comprised D7 and M10 bars welded to the steel base component at the locations indicated in Figure 4.1a. These bars ran continuously over the height of the wall to avoid lap splices and to limit the number of test parameters to be considered. The horizontal reinforcement consisted of a D4 bar at every other course. This horizontal reinforcement formed 180°hooks around the outermost vertical bars. Confinement plates of 1.5 mm thickness, cut from mild steel, were also placed in the first four bed joints at the wall toes, as shown in Figure 4.1a, in order to increase the strain capacity of these critical rocking regions. The wall was loaded with an axial stress of 1.17 MPa to represent normal intensity gravity loads.

Table 4.1: Test matrix

Specimen	h_w (mm)	l_w (mm)	Pa (MPa)	ρ_v (%)	ρ_h (%)	Confinement	F_y[i]
Wall 1	2660	1895	1.17	0.36	0.70	yes	23.6 kN
Wall 2	2660	1895	1.17	0.36	0.70	no	23.6 kN
Wall 3	2660	1895	1.17	0.56	0.70	yes	23.6 kN
Wall 4	2660	1895	2.31	0.36	0.70	yes	23.6 kN
Wall 5	2660	1295	1.17	0.36	0.70	yes	23.6 kN
Wall 6	2660	1895	1.17	0.36	0.70	yes	28.3[ii] kN

[i]theoretical yield of each flexural arm calculated from Eq. 2 (East et al. 2022)
[ii]obtained by using a 3/4" steel plate, the next readily accessible size up from the 5/8" used for Wall 1

4.3.2 Design Criteria

The flexural strength of the walls was calculated based on a sectional analysis of the cross-section directly above the steel base, assuming a linear strain distribution. An equivalent stress block with depth a was calculated using Eq. 4.3.1, which is a version of the equation provided by TMS (2016) that has been modified to incorporate Eq. 4.3.2, which was developed by East et al. (2022) to predict the yield force of the flexural arms, F_y. The flexural strength (M_n) of the walls was then calculated using Eq. 4.3.3.

$$a = \frac{\sum_{i=1}^{n} F_{y_i} + P}{0.8 f'_m t_w} \tag{4.3.1}$$

$$F_y = \frac{4}{27} \frac{b^2 t \sigma_y}{h} \tag{4.3.2}$$

$$M_n = \sum_{i=1}^{n} F_y (d_i - \frac{a}{2}) + P \frac{L_w - a}{2} \tag{4.3.3}$$

where b is the largest depth of the tapered flexural arm; t is the thickness of the device; h is the length of the flexural arm; σ_y is the steel yield strength; f'_m is the masonry compressive strength; and t_w is the thickness of the wall.

The amount of ED resistance was set such that the ratio of the moment contribution from the ED devices to that from the gravity loads was less than 1, as presented in Eq. 4.3.4, in order to ensure that a self-centering response was obtained (Kurama et al. 2005):

$$\frac{\sum_{i=1}^{n} F_u (d_i - \frac{a}{2})}{\frac{P(L_w - a)}{2}} < 1 \tag{4.3.4}$$

where F_u is the ultimate force of the flexural arms; d_i is the distance from the pinned connection of the ED device i to the outermost compression point; a is the equivalent stress block depth; P is the gravity load on the wall including its self-weight; and L_w is the wall length. The ultimate force of the flexural arms, F_u, is defined by East et al. (2022), and presented in Eq. 4.3.5, where σ_u is the ultimate strength of the steel:

$$F_u = \frac{6}{27}\frac{b^2 t \sigma_u}{h} \tag{4.3.5}$$

To ensure a rocking joint gap closure after loading, the maximum developed force in the ED devices should be less than the restoring gravity force, following the guidelines outlined by ACI ITG 5.2 (ACI 2009), as presented in Eq. 4.3.6.

$$\frac{\sum_{i=1}^{n} F_{u_i}}{P} < 1 \tag{4.3.6}$$

As the walls were intended to have a failure mode of the flexural arms reaching an ultimate stage, they were designed to have shear and sliding resistances sufficiently higher (i.e., at least two times) than the lateral load corresponding to the flexural strength. The shear strength of each wall was calculated using Eq. 4.3.7 following provisions from the TMS (2016) for fully-grouted reinforced masonry walls.

$$V_n = 0.083\left(4.0 - 1.75\frac{M}{V d_v}\right) A_{nv}\sqrt{f'_m} + 0.25P + 0.5\frac{A_v}{s} f_y d_v \tag{4.3.7}$$

where d_v is the shear depth (assumed to be 0.8 L_w); A_{nv} is the shear area; A_v is the shear reinforcement cross-sectional area; f'_m is the compressive strength

of masonry in MPa; s is the shear reinforcement spacing; and f_y is the shear reinforcement yield strength.

4.3.3 Construction Sequence

The walls were constructed in stages to be representative of how they would be constructed in masonry practice, as shown in Figure 4.2. First, the steel rocking base was fabricated and placed upon the foundation using a layer of mortar (Figure 4.2a) to ensure that the steel base was level in case of irregularities on the foundation surface. Next, the anchor locations were drilled into the foundation and the flexural arms were connected to the rocking base, as shown in Figure 4.2b. The anchors were installed after the foundation was poured in order to avoid detailing requirements pertaining to casting anchors within the foundation. The vertical reinforcement was then welded to the steel base, as shown in Figure 4.2c. Afterwards, the wall of the first story was constructed by certified masons, where each half story was built and then fully grouted (Figure 4.2d). The floor slab of the first story was then cast, as shown in Figure 4.2e. The last two stages were repeated to build the second story, as shown in Figure 4.2f. Such a construction sequence is intended to have minimal changes in the workflow of a traditional masonry construction site, with the only difference being the installation of the steel base with both the flexural arms and the vertical rebars (Figures 4.2a to 4.2c), which could be subcontracted out.

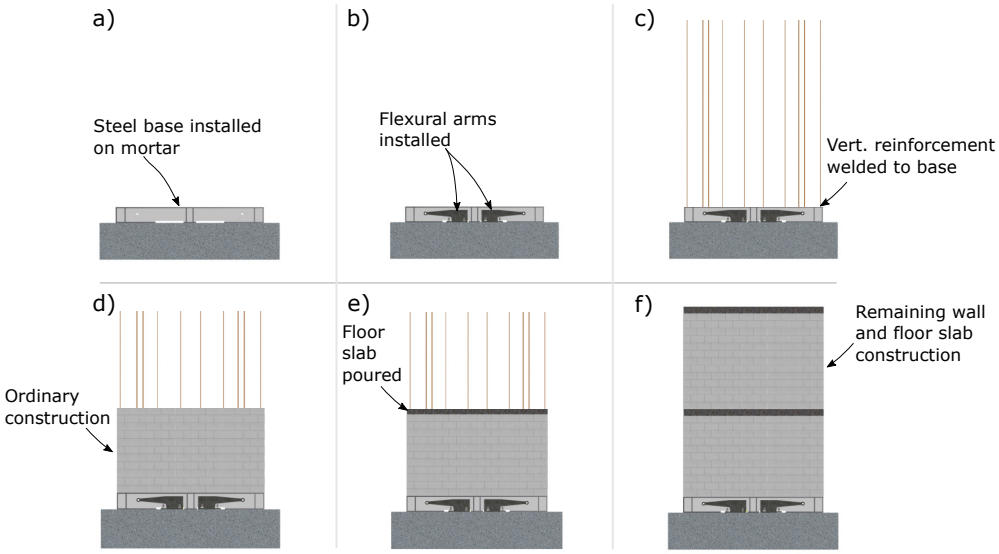

Figure 4.2: Construction sequence

4.3.4 Material Properties

Type S mortar was used to build the walls with an average thickness of approximately 5 mm for each mortar joint. Three mortar cubes were taken from each batch used during construction and they were then tested under compression in accordance with CSA A165-14 (CSA 2014a) to determine their compressive strengths. Additionally, a flow test was conducted on each batch of mortar prepared in accordance with CSA A179-14 (CSA 2014b). Three half-scale blocks (95 mm thickness, 95 mm height and 185 mm length) were capped and tested under compression in accordance with CSA A165-14. Grout was mixed with the proportions of 1:3.9:0.85:0.04 of cement:sand:water:lime. Three cylinders were taken from each grout batch and were cured for 30 days before they were tested in compression following CSA A179-14 (CSA 2014b). Three prisms, each four blocks high by one block long, were constructed from each batch of grout during construction,

and they were then tested in accordance with CSA S304-14 to determine the specified masonry strength, f'_m (CSA 2014c). The reinforcement used within the walls was also tested in tension in accordance with CSA G30.18 (CSA 2014d). In addition, three coupons were taken from each plate used to fabricate the flexural arms and tested in accordance with ASTM A370 (ASTM 2013). Concrete cylinders were also taken from the foundation as well as from the floor slabs and tested in accordance with CSA A23.3-14 (CSA 2014e). The resulting material properties and corresponding coefficients of variation (C.o.V.) for all the tested samples are summarized in Table 4.2.

Table 4.2: Material Properties

Material Test	Average Values	C.o.V (%)
Type S mortar	19.9 MPa	8.9
Mortar flow test	126.6 %	14.3
Half-scale block	25.4 MPa	2.9
Grout	23.6 MPa	9.6
Masonry compressive strength	11.5 MPa	9.8
D4 reinforcement	504 MPa	3.1
D7 reinforcement	462 MPa	3.6
M10 reinforcement	479 MPa	4.4
Coupon test	352 MPa	1.3
Floor slab	26.5 MPa	2.5
Foundation	32.4 MPa	1.7

4.3.5 Test Setup

The test setup is shown in Figure 4.3. The reinforced concrete footing for each wall was prestressed to the strong floor of the Applied Dynamics Laboratory at McMaster University, with a layer of mortar to ensure the wall was level. At the top of each wall, a rigid steel loading beam was mortared to the top slab.

Six 25 mm steel rods were cast in the open cells of the wall and protruded above the top slab and were subsequently welded to the loading beam to facilitate a uniform transfer of load. The walls were also constrained in the out-of-plane direction at the first and second story slabs using a roller system at four points on each slab, as shown in Figure 4.3. The purpose of the slabs was to provide a location for out-of-plane restraint and to mimic the real construction process, without adding the stiffness and strength that would be provided by the slabs in a complete building system. The axial force due to tributary gravity loads was simulated using two hydraulic jacks attached at the top of the wall using two 25 mm high-strength rods and a box section atop the loading beam.

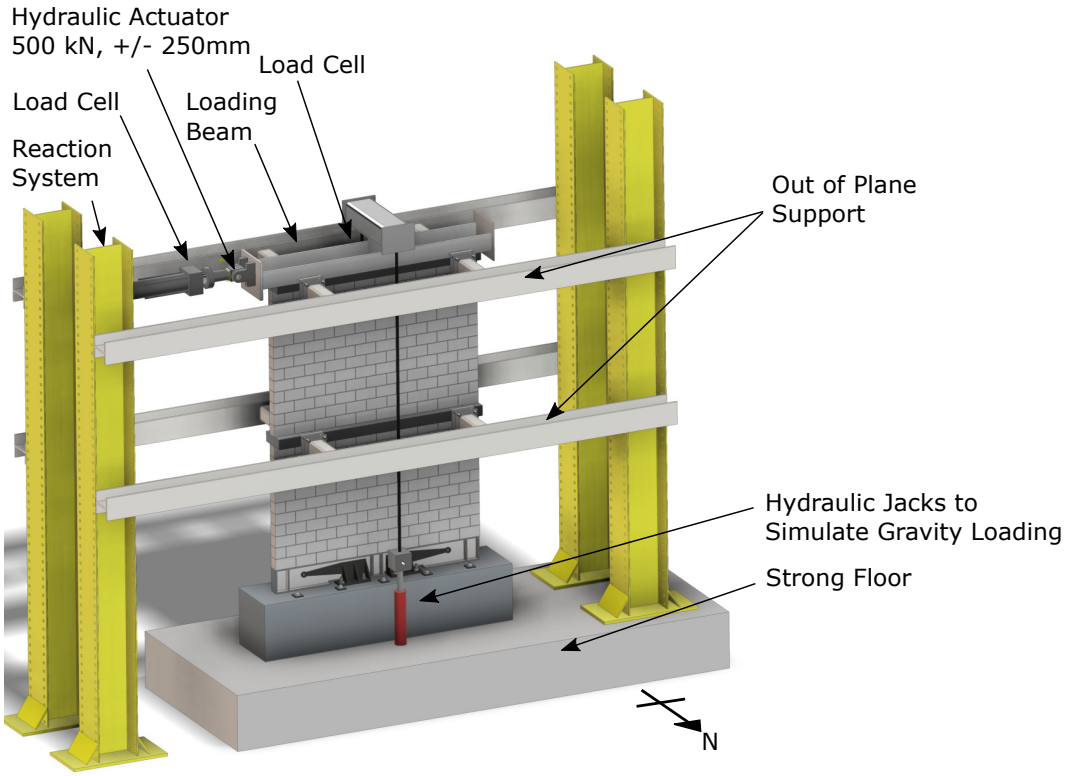

Figure 4.3: Test setup

4.3.6 Instrumentation

A total of 23 linear potentiometers and 16 strain gauges were mounted on the South face of each wall, as presented in Figure 4.4. The vertically mounted linear potentiometers (V1-V17) were used to measure vertical displacements at various locations on the wall. Five vertical potentiometers (V1-V5) were mounted at 240 mm from the wall-foundation interface to measure the gap opening at the base of the wall. Two vertical potentiometers (V6-V7) were attached to the pinned end of the arms, while the remaining ten vertical potentiometers (V8-V17) were used to calculate axial strains. Lateral displacements were also monitored through four horizontally mounted linear potentiometers (H1-H4), while the remaining two horizontal potentiometers (H5-H6) were used to measure the relative sliding between the wall and the footing of each wall (H5) as well as between the footing and the laboratory floor (H6).

In addition to this, each outermost vertical reinforcement bar had three strain gauges at 50 mm (S1 and S4), 100 mm (S2 and S5), and 200 mm (S3 and S6) from the masonry-steel interface to assess if the reinforcement remained elastic throughout testing. Two additional strain gauges were used on the first (S8) and third (S9) transverse reinforcement bars, midway across the wall to investigate the strains forming in the shear reinforcement. Three strain gauges were used on the compression side of each of the flexural arms (S10-S16) to capture the onset of yielding in such ED devices.

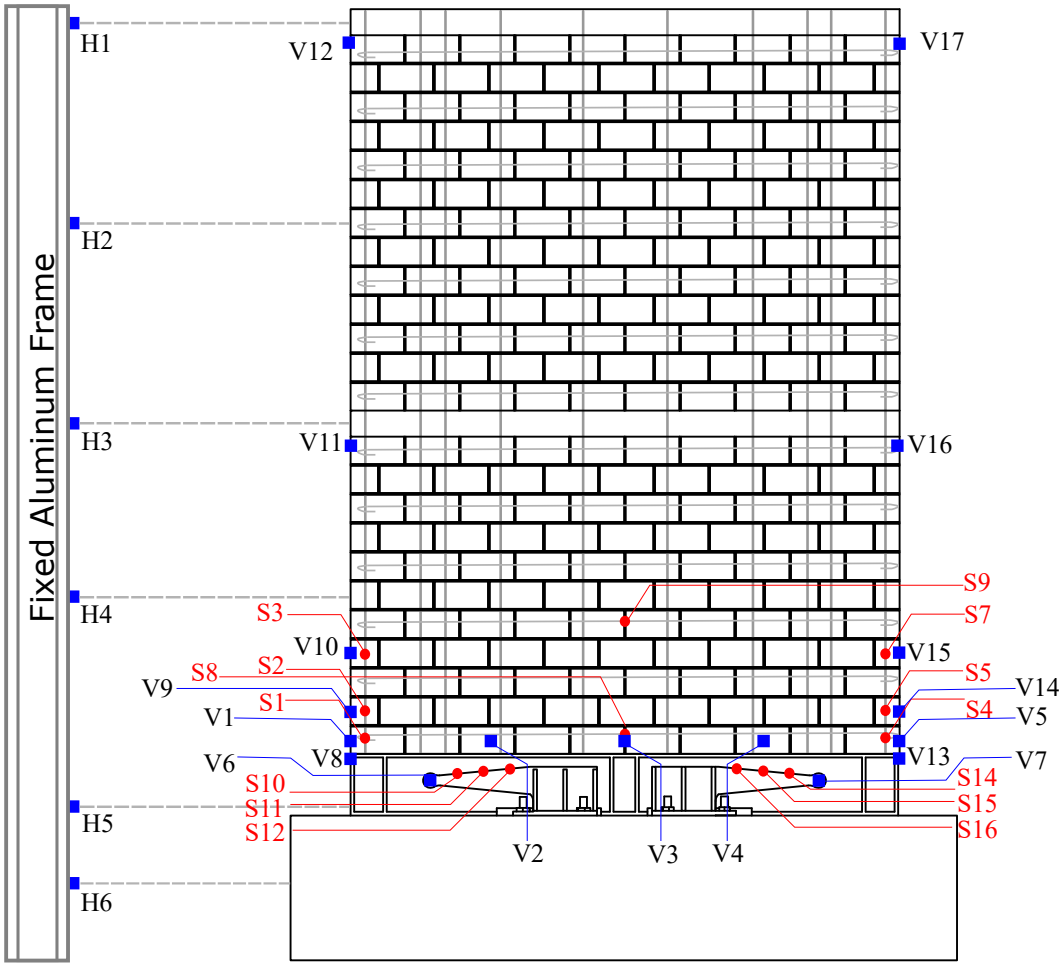

Figure 4.4: Instrumentation details

4.3.7 Digital Image Correlation

A Digital Image Correlation (DIC) technique was used to quantify the displacements on the wall surfaces, thus evaluating the corresponding strains and damage. A pattern of black dots was drawn on a white painted surface of the walls, as shown in Figure 4.5, to ensure an adequate density of the speckle pattern. They were drawn by hand in order to maintain control over the speckle size based on recommendations from Whyte (2012), where similar DIC techniques were used to monitor reinforced concrete walls. The length of

the black dots was intended to be 4-6 mm, corresponding to 5-9 pixels with the cameras used. This was performed to ensure that each subset of pixels examined in the DIC software contained at least three speckles based on recommendations by Sutton et al. (2009). Two Canon Rebel T8i 24.1MP cameras were used to take photographs at roof displacement increments of 5 mm throughout the test and at the end of each cycle. A commercial software, GOM Correlate (GOM, 2016), was used to map the strains by tracking the motion of the pattern of dots throughout the sequence of images. To reduce lens distortion effects, the camera was trained on the first story of each wall, where the concentration of damage was expected.

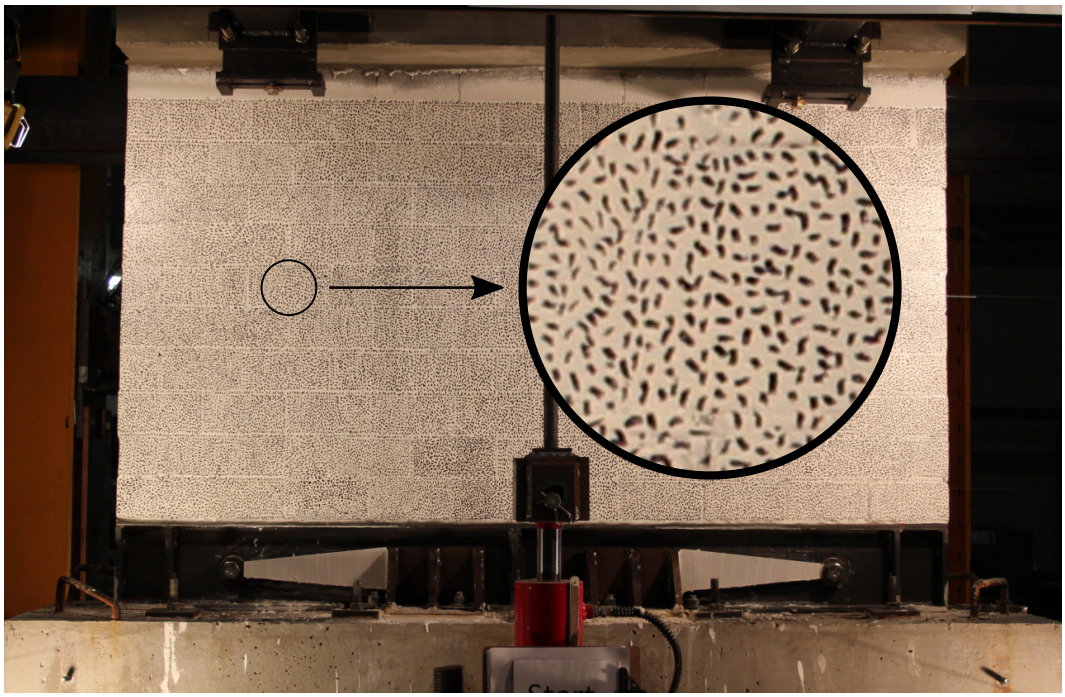

Figure 4.5: DIC Setup

4.3.8 Loading Protocol

To facilitate direct comparison, the FEMA 461 (FEMA 2007) loading protocol was adopted in the current study as this protocol was also used by Yassin et al. (2022b). The loading protocol is a quasi-static testing protocol, as shown in Figure 4.6. In this loading protocol, each cycle was repeated twice, and each subsequent cycle increased by 40% from the previous cycle until the ultimate displacement was reached. After reaching the ultimate displacement, each subsequent cycle amplitude was increased by 30%. Each test was terminated when either the wall lost 50% of its lateral strength or it was unsafe to continue testing due to factors related to the specimen components, as will be discussed later.

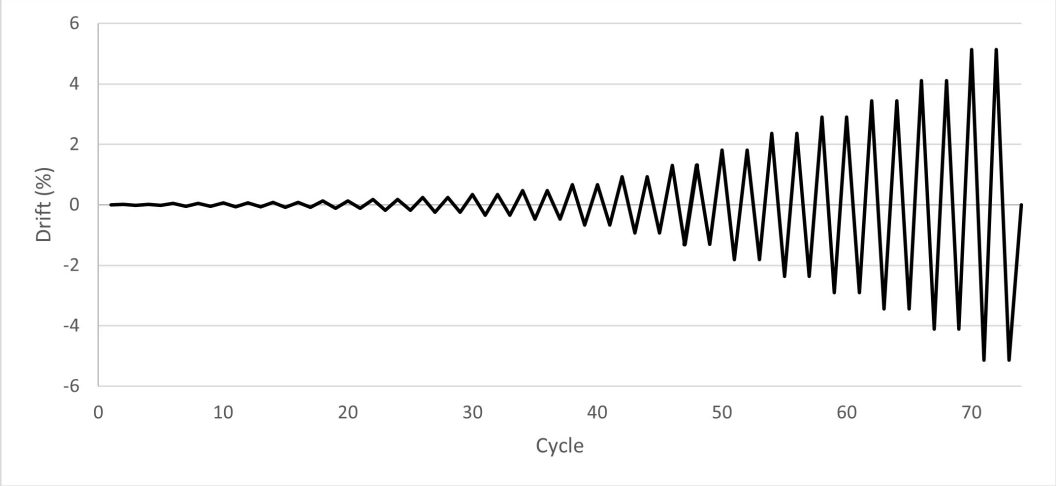

Figure 4.6: Loading Protocol

4.4 Test Results

4.4.1 Damage Sequence

Each wall showed a rocking response characterized by separation at the wall-foundation interface. Drift ratios discussed herein are the displacement of the walls normalized by 2510 mm, representing the height of the topmost horizontal linear potentiometer (H1) above the foundation. Yielding of the flexural arms was identified when strains recorded on SG1-6 exceeded the yield strain of steel. Table 4.3 summarizes key displacements and forces observed throughout each wall test.

For Wall 1, the reference wall for the study, the rocking mechanism was first observed at an average drift ratio (averaged between the push and pull directions) of $\Delta_{up} = 0.08\%$ (Figure 4.7a). As intended, the flexural arms were engaged as the wall began to uplift. The flexural arms reached their yield strain at an average drift ratio of $\Delta_y = 0.7\%$ (Figure 4.7b). Up to this drift ratio, there was no visual indication of tension or shear cracks in the wall. At a drift ratio of 0.94%, a hairline crack was observed at the end of the wall at the second bed joint and spread inwards to roughly one-third of the wall length. At a drift ratio of 5%, the flexural arms came into contact with the bottom flange of the steel base, as shown in Figures 4.7c and d. This contact resulted in a sharp spike in the lateral strength of the wall as the force transferred directly into the fixed end of the flexural arms, as opposed to through flexure along the entire length of the arms as originally intended. The test was terminated because of this contact. No significant damage was observed throughout the test, and no significant sliding was recorded at any point during the test.

Figure 4.7: Test photos at various drift ratios; a) Wall 1 uplift; b) Wall 1 flexural arm yield; c) Wall 1 peak drift ratio (5% or 125 mm); d) Wall 1 flexural arm contact with steel base at peak drift ratio; e) Wall 2 peak drift ratio; f) Wall 3 peak drift ratio; g) Wall 4 prior to failure; h) Wall 4 post-failure; i) Wall 5 peak drift ratio; and j) Wall 6 peak drift ratio

Wall 2 was identical to Wall 1 but with no confinement plates in the rocking toes. As such, a very similar response was observed for Wall 2 compared to Wall 1. Uplift was first observed at an average drift ratio of 0.08%, nearly identical to Wall 1. This was expected as the lack of confinement plates in Wall 2 did not influence its uplift moment. The flexural arms reached a yield strain at a very similar average drift ratio of 0.65% compared to Wall 1. At an average drift ratio of 1.1%, hairline cracks were observed at the first three bed joints in tension. Notably, more bed joints developed hairline cracks in Wall 2 compared to Wall 1. This is attributed to the presence of confinement plates in Wall 1 that led to a single, dominant crack forming earlier because there was less mortar within the joints as the total thickness of the joints was still 5 mm, despite having 1.5 mm plates. As such, this single crack occurred earlier and was wider than the multiple cracks that formed in Wall 2. No significant damage was observed throughout the remainder of the test of Wall 2, and the test of this wall was terminated at a drift ratio of 5% when the flexural arms came into contact with the steel base, as shown in Figure 4.7e.

Wall 3, with additional vertical reinforcement, exhibited a very similar response to Wall 1. Uplift observed at an average drift ratio of 0.08%. Similar to Wall 1, the flexural arms yielded at a drift ratio of 0.67%. Hairline cracks were first observed at a drift ratio of 0.98% and propagated similarly to Wall 1. No significant damage was also observed until the test was terminated at a drift ratio of 4%, as shown in Figure 4.7f. As this was the first wall tested in the experimental program, the remaining walls were constructed to accommodate a drift ratio of 5% before the contact between the arms and the steel base occurred.

Wall 4, with a higher axial load, exhibited a delayed initiation to uplift

relative to Wall 1. The uplift was initiated at a drift ratio of 0.14%, as larger forces were required to overcome the axial load, thus imposing larger flexural deformations on the wall prior to uplift. The flexural arms also experienced yield at a later drift ratio of 0.79%. Unlike Wall 1, at this drift ratio, the bottom six bed joints developed cracks that propagated throughout the test. At a drift ratio of 2.8%, face shell spalling was observed at the rocking toes of the wall, as shown in Figure 4.7g. At a drift ratio of 2.9%, the wall experienced abrupt failure due to rebar buckling, as can be seen in Figure 4.7h. At this drift ratio, the outermost vertical bar buckled within the compression side of the wall, and immediately caused buckling of each subsequent bar, leading to a progression of complete masonry failure.

Wall 5, with a larger aspect ratio, initiated uplift at a lower drift ratio (0.06%) than Wall 1. This was expected as the height of the wall remained constant while the length was shortened, resulting in a shorter lever arm for the axial load to resist for uplift to occur. The lower force also imposed less flexural deformations on the wall prior to uplift. The flexural arms reached a yield strain at an average drift ratio of 0.65%. Hairline cracks were first observed at a drift ratio of 1.02%, and these cracks did not propagate or widen. Wall 5 reached a drift ratio of 5% before the test was terminated due to contact between the flexural arms and the steel base, as shown in Figure 4.7i.

Wall 6, with larger flexural arms, showed a similar response to Wall 1 before the arms were engaged at a drift ratio of 0.08%. As expected, yielding occurred at a higher drift ratio of 0.74%. Hairline cracks were observed at a drift ratio of 0.98%; however, no significant damage was observed until the end of the test at a drift ratio of 5%, as shown in Figure 4.7j, when the test was

terminated due to the contact between the flexural arms and the steel base.

Table 4.3: Key displacements (in mm) and corresponding forces (in kN) for each wall

Specimen	Direction	Δ_{up} (%)	Q_{up} (kN)	Δ_y (%)	Q_y (kN)	Δ_u (%)	Q_u (kN)
W1	Push	2.1 (0.08)	66.4	18.7 (0.7)	94.3	125 (5.0)	116
	Pull	2.1 (0.08)	67.2	18.3 (0.7)	95.3	125 (5.0)	128[i]
W2	Push	2.0 (0.08)	67.4	17.5 (0.7)	97.3	125 (5.0)	110
	Pull	2.1 (0.08)	66.1	16.9 (0.6)	94.6	125 (5.0)	127[i]
W3	Push	2.2 (0.08)	65.2	18.3 (0.7)	93.2	100[ii](4.0)	108
	Pull	2.2 (0.08)	67.3	17.1 (0.7)	94.5	100[ii](4.0)	108
W4	Push	3.6 (0.14)	136.1	20.4 (0.8)	156.1	80.2[iii](2.9)	169
	Pull	3.8 (0.14)	141.3	21.6 (0.8)	158.2	57.8 (2.2)	170
W5	Push	1.6 (0.06)	33.7	16.9 (0.6)	58.2	125 (5.0)	67.5[ii]
	Pull	1.5 (0.06)	34.8	17.2 (0.7)	57.6	125 (5.0)	65.0
W6	Push	2.2 (0.08)	62.4	19.5 (0.7)	103.4	125 (5.0)	120.7
	Pull	2.2 (0.08)	63.8	19.8 (0.7)	105.8	125 (5.0)	125.6[ii]

[i]Force increased sharply when contact was observed between the flexural arms and the steel base

[ii]Test was terminated prior to the final cycle due to less clearance between the arms and the steel base

[iii] Wall failed in this cycle to reach the target displacement

4.4.2 Force-Displacement Response

The force-displacement response, measured using the load cell of the hydraulic actuator and the lateral displacement of the horizontal potentiometer H1, is plotted in Figure 4.8. The figure shows that all six walls had the intended self-centering flag shaped hysteretic response, even with no post-tensioning. The flexural arms of Wall 1 reached a yield strain at an average force of 94.8 kN. The design yield force was 95 kN, and therefore, the design methodology used in the current study was deemed effective for Wall 1. Wall 1 reached peak forces of 116 kN and 128 kN in the push and pull directions, respectively. This asymmetric response is due to the contact between the flexural arms and the steel base that resulted in spikes in the forces of the final push and pull cycles,

as shown in Figure 4.8. Wall 1 reached these peak forces at a drift ratio of 5%, indicating that if this contact had not been made, the wall could have reached higher ultimate forces in both directions. At larger displacement cycles, the unloading hysteretic response is somewhat irregular. This is likely due to increased force demands creating slight uplift of the Hilti anchors used for fixing the flexural arms to the foundation. As they are mechanical expansion anchors, they rely on concrete bearing for the connection, and at high forces the anchors allow for slight uplift, resulting in some slack to the system upon unloading as the flexural arms transition between tension and compression.

As can be seen in Table 4.3, the yield forces (Q_y) of Walls 2 and 3 were within 3% of Wall 1, indicating that the confinement plates and the vertical reinforcement did not influence the yield force of each wall. Table 3 shows also that the ultimate forces (Q_u) of Wall 2 were 110 kN and 127 kN in the push and pull directions, respectively, similar to Wall 1. Wall 3 had a similar peak force of 108 kN in both directions, which was less than the ultimate force of walls 1 and 2 because Wall 3 was tested only to a drift ratio of 4%, with no spike in forces. This is consistent with the nearly identical overall hysteretic responses between Walls 2 and 3 compared to Wall 1 in Figure 4.8.

Wall 4 had significantly different average yield and ultimate forces of 157 kN and 170 kN, respectively, due to its higher axial load. Wall 5 also exhibited different yield and peak forces on average of 58 kN and 66 kN, respectively, due to the higher aspect ratio of this wall. As the energy devices used in Walls 4 and 5 were nearly identical to those in Wall 1, the hysteretic responses shown in Figure 4.8 are nearly identical to Wall 1 following uplift, but at different forces as the increased axial load and aspect ratios increased and decreased the uplift forces respectively. As can be seen in Table 4.3, Wall 6 had slightly

larger yield and ultimate forces than Wall 1 due to the larger flexural arms used Wall 6, which also resulted in slightly wider hysteretic loops, displayed in Figure 4.8. It was also observed that the anchors connecting the flexural arms in Wall 6 provided more flexibility and slight uplift upon loading due to imperfect installation of the anchors. This resulted in a slightly more flexible response at small drifts compared to Wall 1, despite the larger flexural arm used.

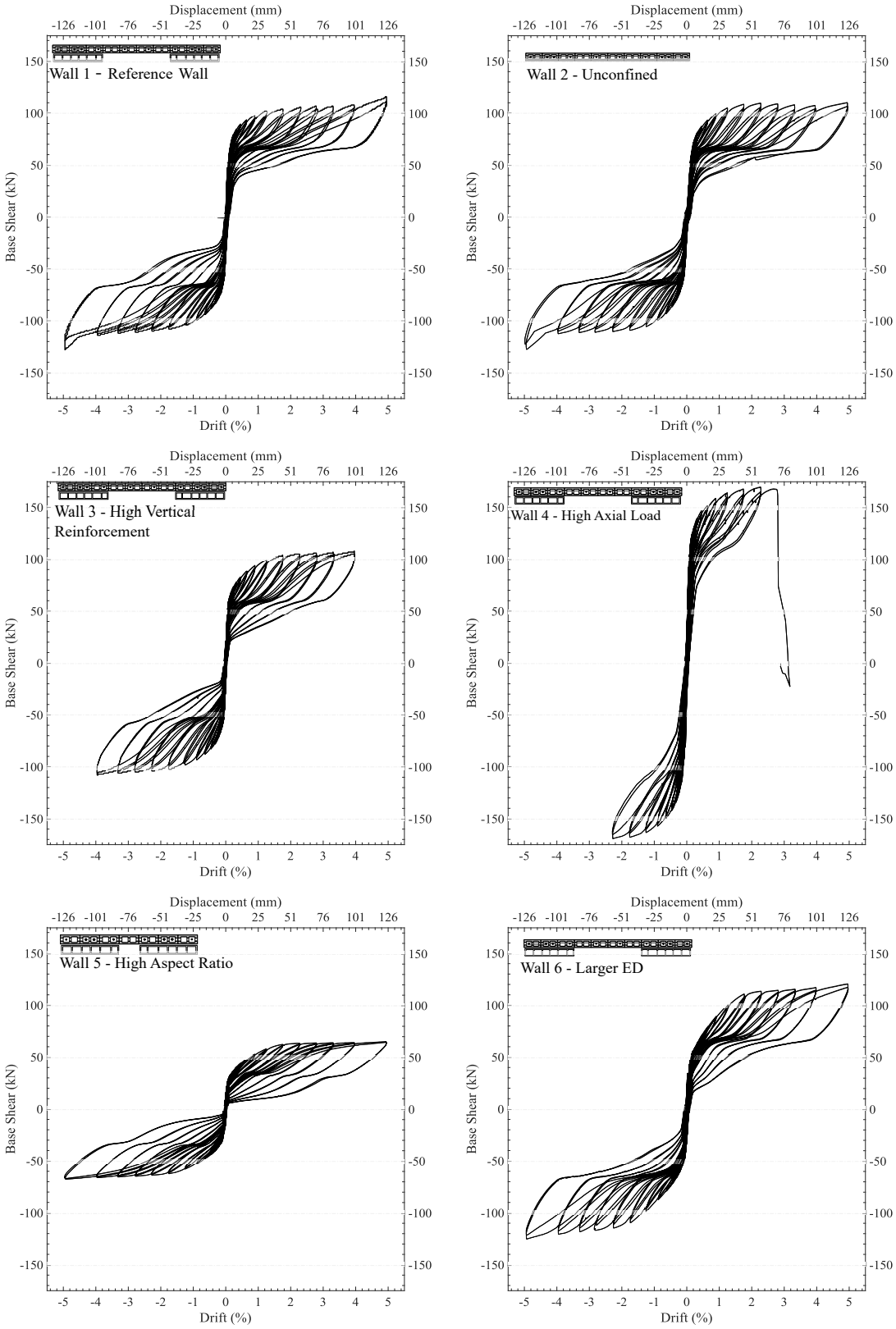

Figure 4.8: Hysteretic responses of the test walls

4.4.3 Backbone Curves

Figure 4.9 presents the load-displacement envelopes for the first cycle at each drift ratio for all the walls. All walls experienced similar, distinct stages throughout the tests. Specifically, the first stage was decompression, which initiated at a very low drift ratio when the overturning moment due to the lateral load exceeded the decompression moment of the wall. Following this, the flexural arms started to elastically deform, resulting in a change in stiffness. As reported by East et al. (2022), the flexural arms did not display a distinct yield plateau as they were intended to yield progressively throughout the cross-section along the entire length, thus maximizing the energy dissipated while also maintaining significant ductility. As such, the stiffness of the walls continuously change in Figure 4.9, resulting in a rounded portion of the load-displacement envelope. Once the entire length of the flexural arm yielded, at a displacement of approximately 45 mm for all the walls except Wall 4 (i.e., which yielded at a displacement of 54 mm) based on strain gauge readings (SG10-SG16), the flexural arms experienced strain hardening but the overall system stiffness became much lower. This resulted in a relatively constant plateau throughout the larger drift ratios. Due to the high displacement capacity of the arms, no strength degradation was observed in any of the walls, apart from Wall 4.

4.4.4 Crack Widths

Figure 4.10 shows the DIC analysis results at several key points throughout the loading history of Wall 4. This test was selected as an example because Wall 4 had the most damage. The DIC analysis shows the profile of the vertical

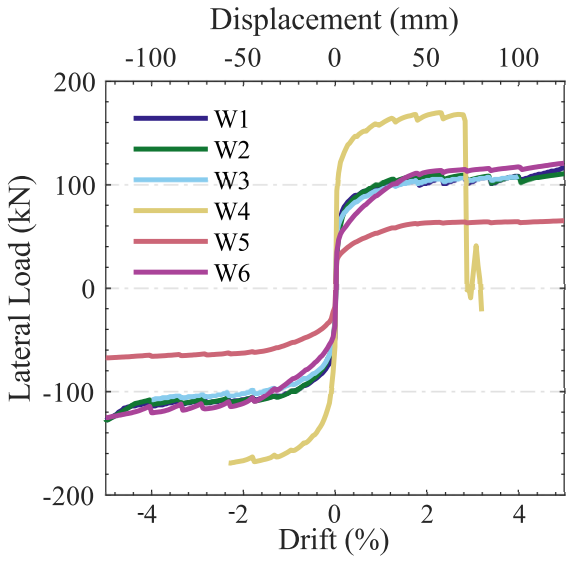

Figure 4.9: Envelope responses of the test walls

strains on the North surface of the wall throughout the loading history. As can be seen in Figure 4.10, hairline cracks that were not visible during the test at early displacement cycles are indicated by the DIC analysis, and the propagation of these cracks is also observed with increased cycles.

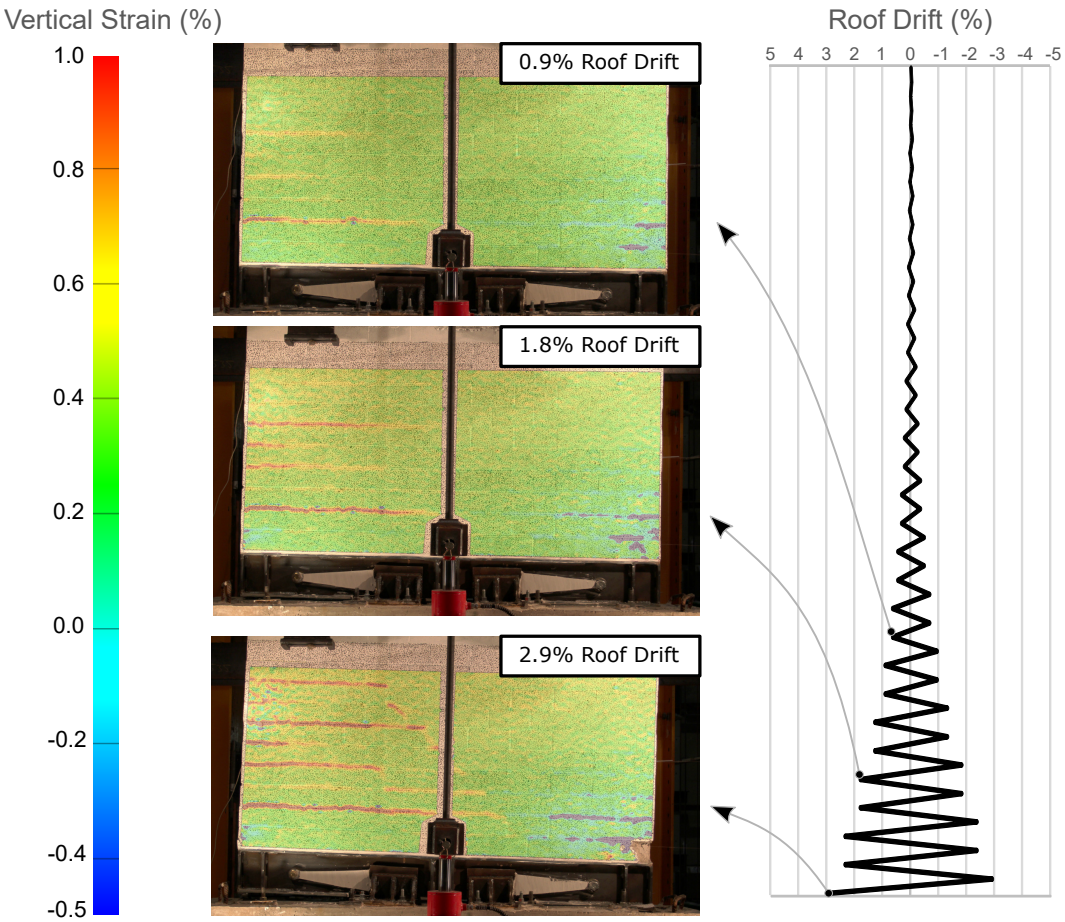

Figure 4.10: DIC analysis results of Wall 4 at various drift ratios

Crack widths were subsequently quantified using DIC by tracking the relative displacements of the pixels above and below the cracks as they propagate. The largest crack widths throughout the loading history were also measured physically using a Starret-487 feeler gauge, to a tolerance of 0.0015 inches (0.0381 mm). These measurements were compared to the analysis results in order to assess the accuracy of the DIC technique, as shown in Fig. 4.11 for Wall 4. The figure shows that the physical measurements were within 10% of the DIC analysis results at several different stages of the testing protocol. Based on the DIC results, the crack widths increased and

decreased by approximately 0.3 mm with the reverse cycling of the wall, indicating that the crack opened and closed, as expected, with the push and pull directions of the testing protocol.

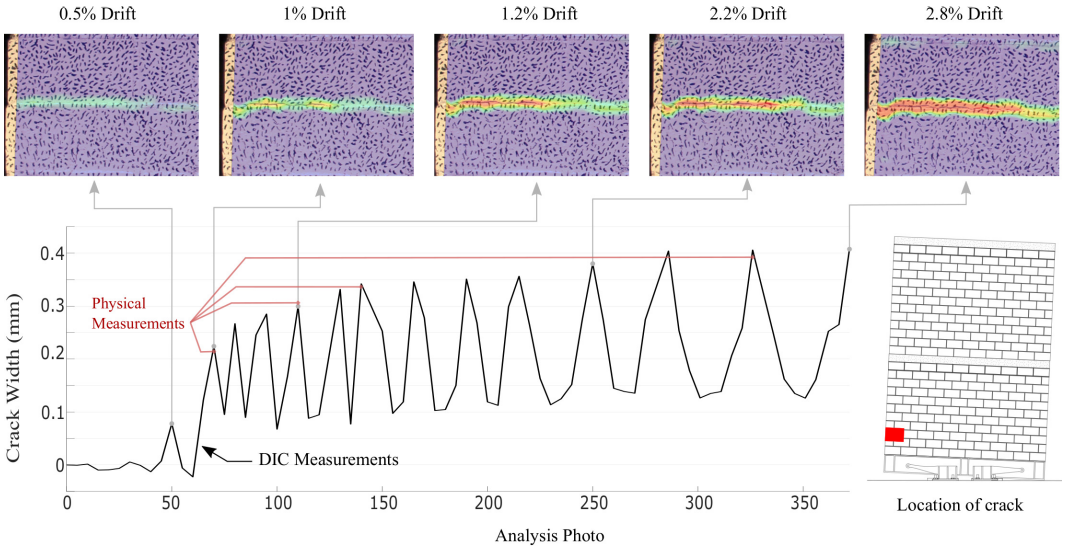

Figure 4.11: DIC results of the largest crack width of Wall 4

After verifying that the crack widths obtained from the DIC analyses were accurate, the largest cracks of each wall were determined and plotted at their corresponding drift ratios, as shown in Figure 4.12. Due to errors related to the camera setup, the results of Wall 5 are not presented in the figure. As can be seen in Figure 4.12, the largest cracks were observed in Wall 4 due to the significantly higher lateral load imposed on this wall, where the largest crack reached a maximum width of 0.42 mm just before failure. Conversely, Wall 3 had the smallest crack width at the end of the test, with a maximum crack width of 0.2 mm. Walls 1, 2, and 6 all had cracks that remained below 0.35 mm in width throughout the tests. Overall, the walls experienced minimal damage throughout the loading history, with no significant cracks due to tension, shear, or compression in any of the walls, except for Wall 4 immediately before its

failure.

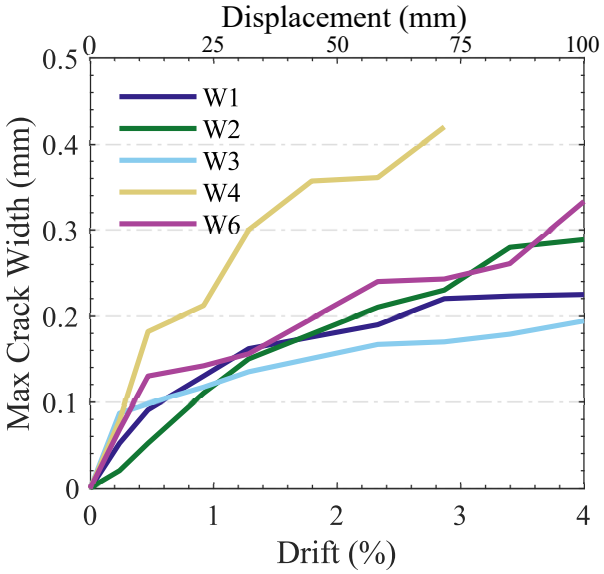

Figure 4.12: Maximum crack widths for each wall using DIC

4.4.5 Residual Drift Ratios

The residual drift is determined in the current study as the average lateral drift at the points of zero lateral force following the end of the first cycle at each displacement level. Figure 4.13 plots the residual drift against the corresponding peak lateral drift of the cycle. As shown in the figure, the residual drifts for all the test walls remained below 0.1% up to the maximum drift reached by each wall. This is considerably less than the 0.2% residual drift limit imposed by the FEMA P58 for damage state 1 (DS1), indicating that no structural realignment or repair is required (Applied Technology Council 2018). Figure 4.13 demonstrates clearly one of the advantages of the EASt-CRMW system, where no wall repairs would be required following seismic events, only the replacement of the flexural arms if needed.

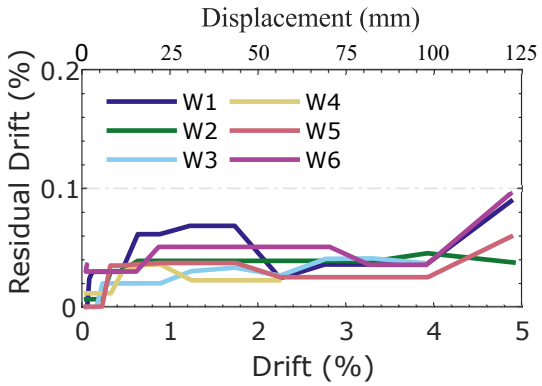

Figure 4.13: Residual drifts of the test walls

4.4.6 Base Rotation-Drift Relationships

For all the test walls, Figure 4.14 shows the relationship between the base rotations and their corresponding lateral drift ratios. The base rotation was obtained using the vertical displacements measured at the wall base (V1-V5). As shown in Figure 4.14, the base rotations and the lateral drift ratios are nearly identical, indicating that the EASt-CRMWs responded mainly in a rigid body rocking deformation model, which agrees with the findings of previous CRMW systems (Kalliontzis and Schultz, 2017; Hassanli et al. 2016; Yassin et al. 2022a and 2022b).

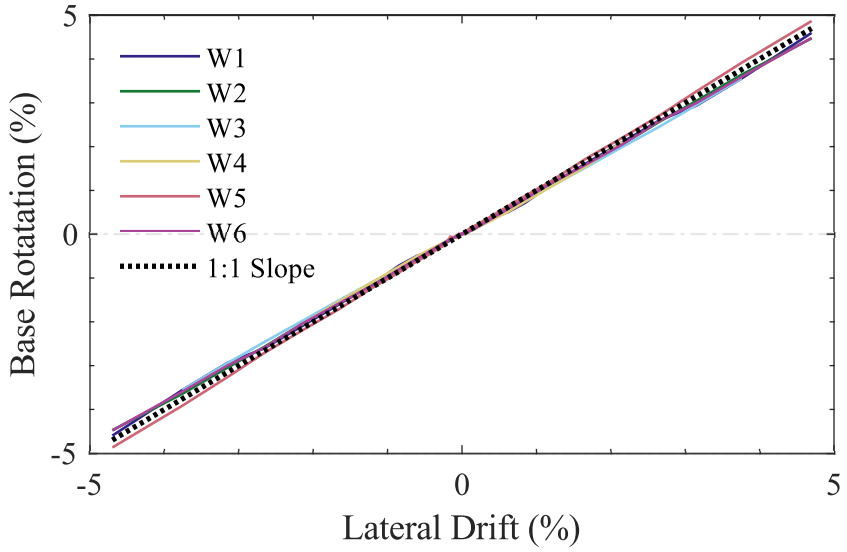

Figure 4.14: Base rotation variations with lateral drifts of the test walls

4.4.7 Energy Dissipation

Figure 4.15 shows the cumulative energy dissipated throughout the testing of each wall. Wall 4 achieved the largest amount of dissipated energy due to its higher lateral load capacity when compared to all the remaining five walls, likely due to more nonlinear response in the masonry because of the higher compressive loads imposed to simulate the gravity loading. As can be seen in the figure, all other walls have similar ED values, with slightly higher values for Wall 6 at large drift ratios, which was expected due to its larger ED devices relative to all other walls.

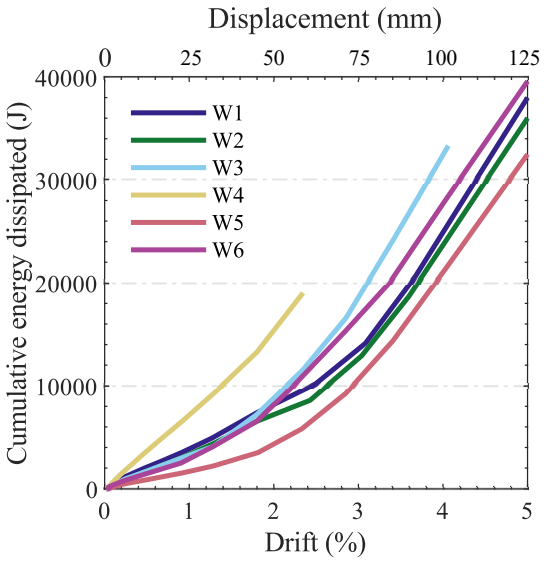

Figure 4.15: Cumulative energy dissipation

4.5 Monotonic Response Predictions

In order to facilitate future design of EASt-CRMWs, two procedures are proposed in the current study to predict the response of the system. Each procedure is based on a sectional analysis at the interface between the steel base and the masonry wall. Both procedures use the following assumptions:

1. The wall is subjected to in-plane deformations and responds in a rocking mechanism.

2. A gap opening mechanism (rocking base) occurs at the wall-foundation interface.

3. The wall behaves as a semi-rigid body, with the deformed region being defined by the compression zone height (Z_c) and the neutral axis depth (c), as shown in Figure 4.16a.

4. The ED devices prevent sliding of the wall relative to its foundation.

5. Each ED device carries an equal proportion of the base shear.

6. The ED devices transfer the loads into the vertical reinforcement directly atop their location on the steel rocking base.

Figure 4.16a outlines critical geometric variables discussed throughout both procedures, while Figure 4.16b shows critical variables related to the flexural arms.

4.5.1 Iterative Procedure

The iterative procedure can be used to estimate the response of walls like those presented earlier in this paper using the following steps.

Step 1: Select a wall rotation, ϑ_w, the corresponding lateral displacement, and an initial estimate for the neutral axis depth, c.

Step 2: Calculate the displacement of the ED devices, δ_{ED}, using Eq. 4.5.1.

$$\delta_{ED} = \theta_w d_{ED} \tag{4.5.1}$$

Step 3: Estimate the total vertical downward force, T, using Eqs. 4.5.2 and 4.5.3.

$$T = \Sigma_{i=1}^{n} F_{ED_i} + W \tag{4.5.2}$$

$$F_{ED} = \begin{cases} F_y \frac{\delta_{ED}}{\delta_y}, & \delta_{ED} \leq \delta_y \\ \frac{F_u - F_y}{\delta_u - \delta_y}(\delta_{ED} - \delta_y), & \delta_y \leq \delta_{ED} \leq \delta_u \end{cases} \tag{4.5.3}$$

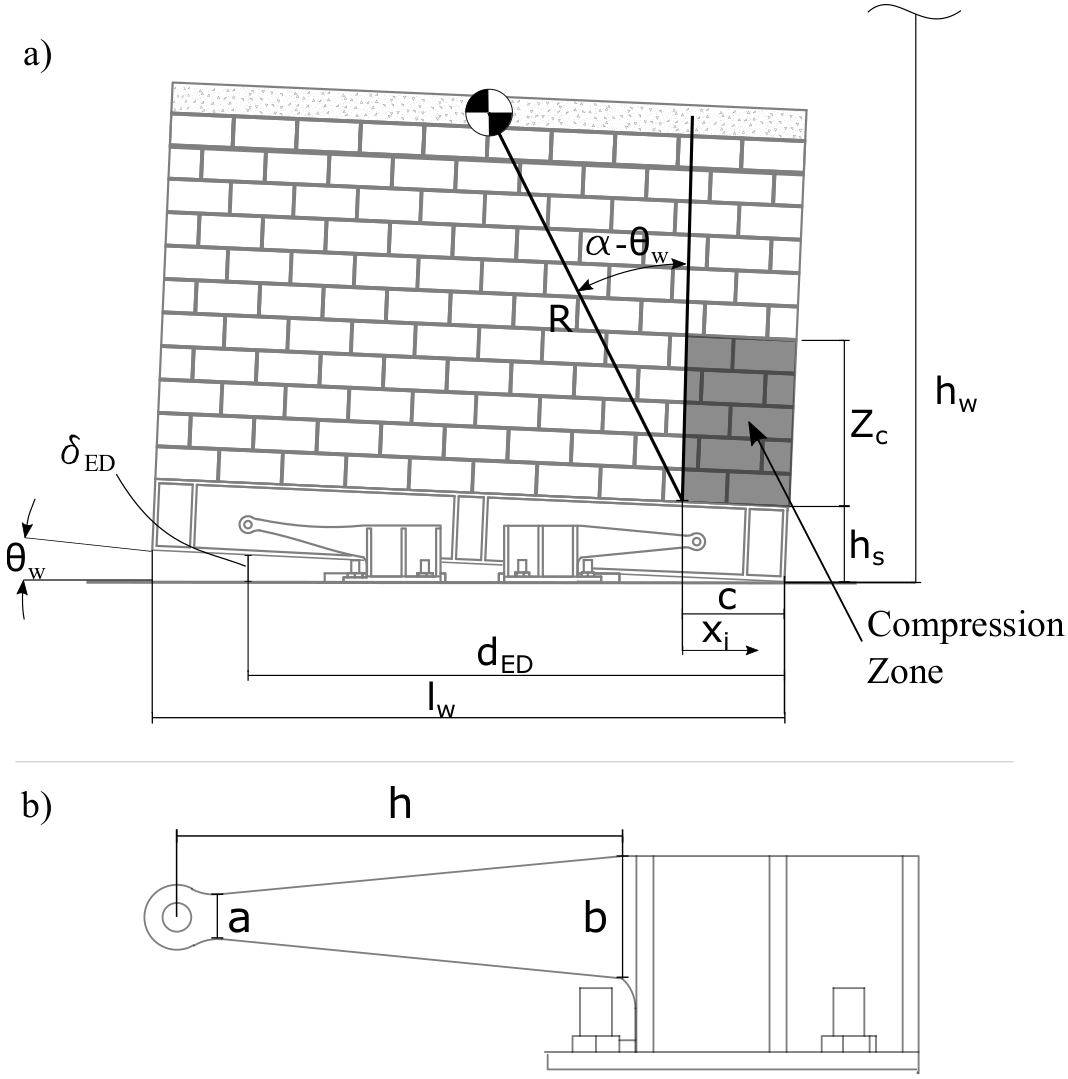

Figure 4.16: Geometric design variables

where Eqs. 4.3.2 and 4.3.5 are used for F_y and F_u, respectively, and n represents the number of flexural arms engaged upon uplift (2 in the current study). Eq. 4.5.4 is an expression for the yield displacement of the flexural arm (δ_u), proposed by East et al. (2022). Meanwhile, δ_u is the ultimate displacement of the flexural arms that was assumed as 15% of shear deformation of the device, based on experimental observations made on component-level testing of these devices in Li (2019) and East et al. (2022).

W is the total weight of the wall and gravity loading on its tributary area.

$$\delta_y = \frac{6h^2 F_y}{E_s t(b-a)^3}\left(\frac{b}{a} - \frac{a}{b} + 2ln\left(\frac{b}{a}\right)\right) \tag{4.5.4}$$

Parameters b, a, and h correspond to geometric properties of the flexural arms, as shown in Figure 4.16b; E_s is the elastic modulus of steel; and t is the thickness of the arm. *Step 4*: Compute the compressive force, C, using Eq. 4.5.6.

$$C = t_w \int_0^c f_{cmi}[\epsilon_{mi}(x_i)]dx_i \tag{4.5.5}$$

where x_i represents the distance of a point within the compressive zone to the neutral axis; t_w is the thickness of the wall; and ϵ_{mi} is the strain in the masonry at point i, defined in Eq. 4.5.7.

$$\epsilon_{mi} = \frac{x_i}{c}\epsilon_m \tag{4.5.6}$$

The maximum compressive strain (ϵ_m) is estimated using Eq. 4.5.8 based on a study by Kalliontzis and Schultz (2017), where the equation was validated based on experimental results from Hassanli et al. (2016, 2017b) and Rosenboom and Kowalsky (2004) for PT-CRMWs. It is assumed that the idealized compression zone (Z_c) is the smaller value of $1.5c$ and the wall height, as recommended by Kalliontzis and Schultz (2017), and ϵ_o represents the masonry compressive strain due to self-weight and gravity loading.

$$\epsilon_m = \theta_w \frac{c}{Z_c} + \epsilon_o \tag{4.5.7}$$

The masonry compressive stress (f_{cmi}) is calculated using Eq. 4.5.9-4.5.10

based on stress-strain curves for masonry developed by Priestley and Elder (1983).

$$f_{cmi} = \begin{cases} 1.067 f'_{cm} \left(\frac{2\epsilon_{mi}}{\epsilon_{ml}} - \left(\frac{\epsilon_{mi}}{\epsilon_{ml}} \right)^2 \right), & \epsilon_m i \leq \epsilon_{ml} \\ 1.067 f'_{cm} [1 - Z_m(\epsilon_{mi} - \epsilon_{ml}], & \epsilon_{ml} \leq \epsilon_{mi} \leq \epsilon_{mp} \\ 0.2 f'_{cm}, & \epsilon_{mi} \geq \epsilon_{mp} \end{cases} \tag{4.5.8}$$

$$\epsilon_{mp} = \epsilon_{ml} + \frac{0.813}{Z_m} \tag{4.5.9}$$

$$Z_m = \frac{0.5K}{\frac{3+0.29 f'_{cm}}{145 f'_{cm} - 1000} - \epsilon_{ml}} \tag{4.5.10}$$

where f'_{cm} is the compressive strength of confined masonry (MPa); K is the ratio between confined and unconfined strength; and $\epsilon_{ml} = 0.002K$ for confined masonry as suggested by Priestley and Elder (1983). For unconfined masonry, as in the case of Wall 2, Eq. 4.5.9 was used but the unconfined compressive strength was used in place of the confined compressive strength, and a value of 1 was used for K in the subsequent calculations.

Step 5: Calculate the difference between T and C. If the two forces are not equal in magnitude, return to Step 4, and revise the calculation for C with a new estimate for the c value until convergence. *Step 6*: Compute the moment at the top of the steel base component using Eq. 4.5.11, where R is the distance from the center of mass to the neutral axis and α is defined in Eq.

4.5.12 and shown in Figure 4.16a.

$$M = \Sigma_{j=1}^{n} F_{ED_j}(d_{ED_j} - c) + WRsin(\alpha - \theta_w) + t_w \int_0^c f_{cmi}[\epsilon_{mi}(x_i)]x_i dx_i \quad (4.5.11)$$

$$\alpha = tan^{-1}\left(\frac{\frac{l_w}{2} - c}{\frac{h_w}{2} - h_s}\right) \quad (4.5.12)$$

where h_w is the height of the wall; and h_s is the height of the steel base component.

Step 7: Compute the horizontal load assuming a load applied at the top of the wall using Eq. 4.5.13 and calculate the axial load in each flexural arm using Eq. 4.5.14, where N is the total number of arms used in the wall (including those that are not engaged in flexure, as per assumption 5).

$$F = \frac{M}{h_w - h_s} \quad (4.5.13)$$

$$F_a = \frac{F}{N} \quad (4.5.14)$$

Step 8: Revise Eqs. 4.3.2 and 4.3.5 to include the axial load of the arm, resulting in Eqs. 4.5.15 and 4.5.16 (East et al. 2022).

$$F_{y,a} = \frac{4}{27}\frac{b^2 t\sigma_y}{h} - \frac{F_a \delta_y}{h} \quad (4.5.15)$$

$$F_{u,a} = \frac{6}{27}\frac{b^2 t\sigma_y}{u} - \frac{1.5F_a \delta_y}{h} \quad (4.5.16)$$

Step 9: Repeat Steps 3-8 with the updated values of F_{ED} until convergence

is achieved between the updated T and C values.

Step 10: Return to Step 1 and repeat for different values of wall rotation and lateral displacement.

4.5.2 Simplified Procedure

The simplified procedure aims at reducing the number of iterations needed for each step by assuming a trilinear relationship between the neutral axis depth and drift based on a single calculated yield point of the system, following the relationship proposed by Kalliontzis and Schultz (2017) and Aaleti and Sritharan (2009). First, to compute the compressive masonry force at a calculated yield displacement for the wall (D_y), an equivalent stress block distribution is assumed magnified by the same K factor from the iterative procedure to account for an increase in masonry strength due to confinement.

Step 1: Calculate the yield displacement, D_y, using Eq. 4.5.17.

$$D_y = \delta_y \frac{h_w}{d_{ED}} + \frac{W\frac{l_w}{2} + 2F_y d_{ED}}{3E_m I} \tag{4.5.17}$$

where I is the second moment of area of the masonry wall cross-section; E_m is the elastic modulus of masonry; and $_{ED}$ is the distance of the ED device from the edge of the wall. This approximation is based on the sum of the displacement due to base rotation and the flexural response of the wall, assuming a single point load at the top of the wall.

Step 2: Compute the compressive force, C, assuming an equivalent stress block using Eq. 4.5.18 and an estimate for the neutral axis depth at the yield

point, c_y.

$$C = K f'_m \alpha \beta t_w c_y \tag{4.5.18}$$

where αand βare the equivalent stress block parameters, both equal to 0.8.

Step 3: Calculate T using Eqs. 4.5.1, 4.5.2 and 4.5.3 assuming ϑ_w=D_y/h_w (Eq. 4.5.1).

Step 4: Same as Step 5 of the iterative procedure.

Step 5: Construct the neutral axis versus wall rotation relationship according to Figure 4.17. This figure proposes a trilinear estimate for the neutral axis variation, where c_y denotes the neutral axis depth calculated in Step 4. The neutral axis depth is assumed to remain constant for all wall rotations larger than 0.5%, as displayed in Figure 4.17. This relationship is taken from past studies incorporating both analytical and experimental work involving sectional analysis of PT-CRMWs (Kalliontzis and Schultz 2017). Included in Figure 4.17 is the neutral axis depth for Walls 1 and 3 (obtained from V1-5 in Figure 4.4), which had similar geometrical properties, displaying the approximation to be reasonably accurate for a simplified procedure.

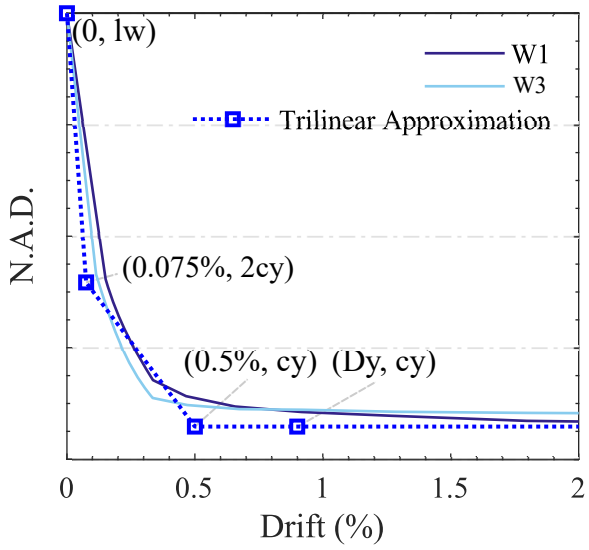

Figure 4.17: Trilinear idealization of the neutral axis depth

Step 6: Compute the moment at the top of the steel base component for all values of ϑ_w using Eq. 4.5.19 with the value of c from Figure 4.17 corresponding to each value of ϑ_w.

$$M = \Sigma_{j=1}^{n} F_{ED_j}(d_{ED_j} - c) + WRsin(\alpha - \theta_w) + C\left(c - \frac{\beta c}{2}\right) \qquad (4.5.19)$$

Step 7: Compute the horizontal load assuming a load applied at the top of the wall using Eq. 4.5.13.

4.5.3 Validation of Procedures

The force-displacement envelopes of all the test walls were calculated using iterative and simplified procedures and are compared to the experimental envelopes in Figure 4.18. Both procedures can capture the experimental results, with some minor deviations in Walls 4 and 6. The discrepancy for

Wall 4 arises from the trilinear neutral axis depth approximation used, as it was calibrated using walls from previous studies that had considerably less axial load, and thus, is less accurate for walls with axial stress ratios higher than the recommended limits of 15% of the compressive strength of the wall. In Wall 6, the additional flexibility from the anchors results in a softer stiffness upon uplift as discussed previously, which is not accounted for in the calculations. Overall, the iterative and simplified procedures were able to capture the response of the test walls with maximum errors of 3.5% and 8.0%, respectively, aside from Wall 4 and 6, in which the maximum errors were 17% and 18% due to the aforementioned factors.

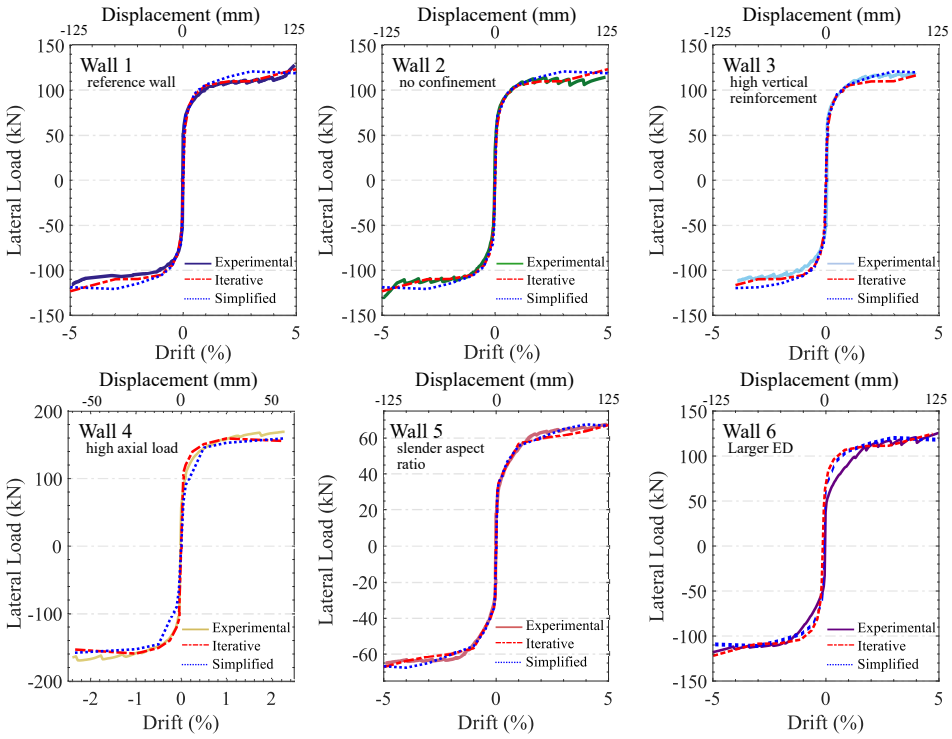

Figure 4.18: Monotonic response predictions compared to the experimental results

4.6 Conclusions

The current study presented the experimental results of six half-scale, two-story controlled rocking masonry walls with Energy dissipation Accessible in a Steel base (EASt-CRMWs). Through these walls, different parameters were investigated, including the aspect ratio, vertical reinforcement ratio, confinement technique in the rocking toes, axial load, and amount of energy dissipation (ED). In addition to maintaining the construction process, the steel base allowed for externally mounted ED devices to be easily installed within the footprint of the wall. The work presented in this paper led to the following observations and conclusions:

- All walls reached 4% drift with no sign of strength degradation, except for one wall which had a much larger axial load. The inelastic response was concentrated in the ED devices connected to the steel rocking base of the wall.

- All walls achieved a high level of self-centering, with residual drifts of less than 0.1%.

- Confining plates at the bed joints were not required to avoid damage in the wall toes, due to the steel base serving as the rocking point.

- Unusually high levels of axial stress (2.31 MPa, corresponding to an axial stress of 18% of the compressive capacity of the wall) reduced the ultimate displacement capacity of the walls, resulting in reinforcement buckling at a drift ratio of 2.9%.

- The aspect ratio altered the numerical values of rocking response

parameters, but the overall behavior of the walls with different aspect ratios remained consistent.

- Minimum vertical reinforcement was sufficient to maintain the wall integrity as the EASt-CRMWs were controlled by a rigid body rocking mechanism, without relying on the reinforcement for ductility capacity at larger deformations. Only minor superficial cracks were observed throughout all tests (less than 0.5 mm in width).

- The proposed iterative and simplified sectional analysis procedures were able to predict the monotonic force-displacement responses of the EASt-CRMWs to within 3.5% and 8%, respectively, except for two walls over a small range of low-amplitude response (between 0.5% and 1.0% drift ratios).

In general, the tests demonstrated that relying on gravity loads and supplemental ED devices can maintain the high performance of EASt-CRMWs regarding their self-centering ability, minimal damage, and high drift capacity. The steel base further simplified the detailing requirements and installation of the flexural arms, while also reducing the damage at the rocking toes. Future study is still needed to investigate the replaceability of the flexural arms following seismic events, as well as to develop numerical models capable of predicting the response of EASt-CRMWs.

4.7 Acknowledgements

The financial support for this project was provided through the Canadian Concrete Masonry Producers Association (CCMPA), the Canada Masonry Design Centre (CMDC), the Natural Sciences and Engineering Research Council (NSERC), and the Ontario Centres of Excellence (OCE).

4.8 Data Availability Statement

All data, models, and code generated or used during the study appear in the submitted article, are referenced accordingly, or are available upon reasonable request.

4.9 References

Aaleti, S., and S. Sritharan. 2009. "A simplified analysis method for characterizing unbonded post-tensioned precast wall systems." *Engineering Structures*, 31 (12): 2966-2975. https://doi.org/10.1016/j.engstruct.2009.07.024.

ACI Innovation Task Group 5. 2009. "Requirements for Design of a Special Unbonded Post-Tensioned Precast Shear Wall Satisfying ACI ITG-5.1 (ACI ITG-5.2-09) and Commentary." *American Concrete Institute*, 1: 1–21.

Applied Technology Council. 2018. "FEMA P-58-1: Seismic Performance Assessment of Buildings. Volume 1 – Methodology." *FEMA P-58-1.*

ASTM (American Society for Testing and Materials). 2013. Mechanical Testing of Steel Products. A370. West Conshohocken, PA.

Banting, B. R., and W. W. El-Dakhakhni. 2014. "Seismic Performance Quantification of Reinforced Masonry Structural Walls with Boundary Elements." *Journal of Structural Engineering*, 140 (5): 04014001. https://doi.org/10.1061/(asce)st.1943-541x.0000895.

CSA (Canadian Standards Association). 2014a. *Mortar and grout for unit masonry*. CSA A179-14. Mississauga, ON: CSA.

CSA (Canadian Standards Association). 2014a. *Standards on concrete masonry units*. CSA A165-14. Mississauga, ON: CSA.

CSA (Canadian Standards Association). 2014c. *Design of masonry structures*. CSA S304-14. Mississauga, ON.

CSA (Canadian Standards Association). 2014d. *Carbon steel bars for concrete reinforcement*. CSA G30.18-09. Mississauga, ON.

CSA (Canadian Standards Association). 2014e. *Design of concrete structures*. A23.3-14. Mississauga, ON.

East, M., Li, J., M. Ezzeldin, and L. Wiebe. 2022a. "Development of a Flexural Yielding Energy Dissipation Device for Controlled Rocking Systems." *Journal of Structural Engineering*. https://doi.org/10.1061/(ASCE)ST.1943-541X.0003461

Erkmen, B., and A. E. Schultz. 2009. "Self-centering behavior of unbonded, post-tensioned precast concrete shear walls." *Journal of Earthquake*

Engineering, 13 (7): 1047–1064. https://doi.org/10.1080/13632460902859136.

Ezzeldin, M., W. El-Dakhakhni, and L. Wiebe. 2017. "Experimental Assessment of the System-Level Seismic Performance od an Asymmetrical Reinforced Concrete Block-Wall Building with Boundary Elements." *Journal of Structural Engineering*, 143 (8): 04017063. https://doi.org/10.1061/(asce)st.1943-541x.0001790.

(FEMA). 2007. "Interim Protocols For Determining Seismic Performance Characteristics of Structural and Nonstructural Components Through Laboratory Testing." *FEMA 461*.

GOM mbH. 2016. "Inspection Basic." GOM Software

Hassanli, R., M. A. ElGawady, and J. E. Mills. 2016. "Experimental Investigation of In-Plane Cyclic Response of Unbonded Posttensioned Masonry Walls." *Journal of Structural Engineering*, 142 (5): 04015171. https://doi.org/10.1061/(asce)st.1943-541x.0001450.

Hassanli, R., M. A. ElGawady, and J. E. Mills. 2017a. "In-plane flexural strength of unbonded post-tensioned concrete masonry walls." *Engineering Structures*. 136: 245-260 https://doi.org/10.1016/j.engstruct.2017.01.016.

Kalliontzis, D., and A. E. Schultz. 2017. "Characterizing the In-Plane Rocking Response of Masonry Walls with Unbonded Posttensioning." *Journal of Structural Engineering*, 143 (9): 04017110. https://doi.org/10.1061/(ASCE)ST.1943-541X.0001838.

Laursen, P. T., and J. M. Ingham. 2004. "Structural Testing of Large-Scale Posttensioned Concrete Masonry Walls." *Journal of Structural Engineering*, 130 (10). https://doi.org/10.1061/(asce)0733-9445(2004)130:10(1497).

Li, J. 2019. "Development of a Flexural Yielding Energy Dissipation Device for Controlled Rocking Masonry Walls." *MASc Thesis*. McMaster University.

Priestley, M., and D. Elder. 1983. "Stress-Strain Curves for Unconfined and Confined Concrete Masonry." *ACI Journal Proceedings*, 80 (3): 192-201. https://doi.org/10.14359/10834.

Priestley, M. J. N., and J. R. Tao. 1993. "Seismic Response of Precast Prestressed Concrete Frames With Partially Debonded Tendons." *PCI Journal,* 38 (1): 58–69. https://doi.org/10.15554/pcij.01011993.58.69.

Rosenboom, O. A., and M. J. Kowalsky. 2004. "Reversed In-Plane Cyclic Behavior of Posttensioned Clay Brick Masonry Walls." *Journal of Structural Engineering*, 130 (5): 787-798. https://doi.org/10.1061/(asce)0733-9445(2004)130:5(787).

Shedid, M. T., W. W. El-Dakhakhni, and R. G. Drysdale. 2009. "Behavior of fully grouted reinforced concrete masonry shear walls failing in flexure: Analysis." *Engineering Structures*, 31 (9): 2032-2044. https://doi.org/10.1016/j.engstruct.2009.03.006.

Shedid, M. T., W. W. El-Dakhakhni, and R. G. Drysdale. 2011. "Seismic Response Modification Factors for Reinforced Masonry Structural

Walls." *Journal of Performance of Constructed Facilities*, 25 (2): 74-86. https://doi.org/10.1061/(asce)cf.1943-5509.0000144.

Sutton, M., Orteau, J. J., Schreier, H., 2009. "Image Correlation for Shape, Motion and Deformation Measurements: Basic Concepts, Theory and Application." *Springer Science and Business Media*. doi:10.1007/978-0-387-78747-3

TMS (The Masonry Society). (2016). "Building Code Requirements and Specification for Masonry Structures." TMS 402/602-16, Longmont, CO.

Toranzo, L. A., J. I. Restrepo, J. B. Mander, and A. J. Carr. 2009. "Shake-table tests of confined-masonry rocking walls with supplementary hysteretic damping." *Journal of Earthquake Engineering*, 13 (6): 882–898. https://doi.org/10.1080/13632460802715040.

Wight, G. D. 2006. "Seismic performance of a post-tensioned concrete masonry wall system." *PhD Dissertation*. University of Auckland.

Whyte, C. A. (2012). Hybrid simulation of the seismic response of squat reinforced concrete shear walls. *PhD Dissertation*. University of California, Berkeley.

Yassin, A., Ezzeldin, M., Steele, T., and Wiebe, L. 2020. Seismic collapse risk assessment of posttensioned controlled rocking masonry walls. *Journal of Structural Engineering*, 146(5), 04020060.

Yassin, A., M. Ezzeldin, and L. Wiebe. 2022a. "Experimental Assessment of Controlled Rocking Masonry Shear Walls without Post-tensioning."

Journal of Structural Engineering, 148 (4): 04022018. https://doi.org/10.1061/(asce)st.1943-541x.0003307.

Yassin, A., Ezzeldin, M., and Wiebe, L. 2022b. "Experimental Assessment of Resilient Controlled Rocking Masonry Walls with Replaceable Energy Dissipation." *Journal of Structural Engineering*, (Submitted).

Chapter 5

Repairability and Damage Assessment of Controlled Rocking Masonry Walls with Energy Dissipation Accessible in a Steel Base

5.1 Abstract

In recent years, several studies have investigated the seismic response of controlled rocking masonry walls (CRMWs) that rely on both gravity loading for self-centering, and supplemental energy dissipation (ED) devices to control the response (ED-CRMWs). Such studies had limitations due to ED devices being installed on a masonry wall or being embedded within the wall itself, making repair difficult or impossible following ED yielding or fracturing. The current study describes the experimental testing of two half-scale CRMWs constructed with supplemental flexural yielding Energy dissipation devices Accessible in a Steel base (EASt-CRMWs). The proposed EASt-CRMWs allow for simplified construction and installation of the

energy dissipation devices, in addition to easy access to replace them following damage. The walls were nominally identical, except that Wall 2 was constructed with steel plates at the rocking points between the steel base and the foundation interface. Each wall was tested under quasi-static, cyclic loading up to drifts of 2.35%, after which the ED devices were replaced and the same wall was tested again. In total, Wall 1 was tested three times and Wall 2 was tested twice. All five tests showed a favorable self-centering response with no signs of significant damage to the walls. The ED devices were easily replaced between tests, and the damage was localized to the ED devices. In Wall 1, damage to the mortar at the steel base-foundation interface led to slightly decreased lateral load capacity upon retesting at low drift ratios; the plates in Wall 2 avoided this damage, leading to essentially idental performance between the first and second tests of this wall. In addition, residual drifts remained below 0.05% for all wall tests. Finally, a numerical model and a damage index proposed previously were validated based on both the experimental work presented in this study and additional configurations of EASt-CRMWs presented in a previous recent study. The results show that the model can capture the overall response of the walls, and the damage index can accurately predict the location, type, and severity of damage.

5.2 Introduction

The use of controlled rocking walls that allow for opening at the wall-foundation interface has received considerable attention in recent studies due to their ability to re-center with low residual deformations and minimal

damage following large lateral displacements. Significant steps have been taken to understand the response of controlled rocking systems when applied to masonry walls in several studies (Laursen 2002; Laursen and Ingham 2004; Rosenboom and Kowalsky 2004; Wight 2006; Hassanli et al. 2016; 2017; Yassin et al. 2020; East et al. 2022a). For example, Laursen and Ingham (2004) tested six fully-grouted controlled rocking reinforced masonry walls. These walls relied on post-tensioning (PT) tendons that were placed through the wall to provide restoring forces, thus allowing the wall to return to its original vertical alignment following seismic events. However, the studies reported that the installation of the PT tendons complicated the construction process, and ultimately can lead to poor performance in terms of deformation capacity due to a combination of PT losses and the additional compression demands placed on the rocking toes. A study by Hassanli et al. (2017) highlighted also that controlled rocking masonry systems have low inherent damping compared to conventional masonry systems (i.e., with fixed bases) due to the walls remaining mostly elastic. The use of energy dissipation devices was therefore recommended to address the low damping of the system.

These findings led to a recent study by Yassin et al. (2022a) which incorporated supplemental energy dissipation and omitted PT tendons, instead relying on gravity loads, to provide restoring forces. In this study, six walls were tested with internal, axial yielding energy dissipation devices (ED-CRMWs). These ED-CRMWs were able to withstand large displacements with low residual displacements which are typical characteristics of controlled rocking systems. However, since the energy dissipation devices were located inside the walls, the construction process was

complicated with additional detailing requirements, and the used devices are also irreplaceable following a seismic event. To address these limitations, recent studies were conducted to develop an externally-mounted energy dissipation device (a steel flexural arm) that can easily be replaced following a seismic event (Li 2019; East et al. 2022b). Such studies have experimentally and numerically investigated the performance of such external devices and established design equations that can be used to incorporate them into CRMW systems (East et al. 2022b). Following this, a single wall was tested by Yassin et al. (2022b) that incorporated steel flexural arms connected at the base of the wall using specially fabricated steel blocks and other components cast into the foundation. The results were promising, with only minor damage being observed at the rocking toes at a drift ratio of 1%. The flexural arms were also able to be replaced and the wall was retested, achieving a nearly identical performance. However, the study indicated that alternative methods for detailing and installation of flexural arms are still required.

A recent study by East et al. (2022a) developed a numerical model to capture the results of post-tensioned CRMWs (PT-CRMW) and ED-CRMWs. This model was also associated with a proposed new damage index for reinforced masonry walls, including CRMW systems. Following this, an enhanced system was proposed with a steel base component to reduce damage as well as simplify construction, but no experimental results were available to validate a model for this new system. Therefore, East et al. (2022c) presented six CRMWs with Energy dissipation Accessible constructed atop a Steel base (EASt-CRMWs) that were constructed and tested under quasi-static loading. The results were promising, displaying a

very favorable hysteretic performance with extremely low residual deformations and no significant damage to the masonry wall portions. Despite the flexural arms being replaceable, each wall was tested only once in that study, indicating the need for further study of the repairability of the EASt-CRMW system and its performance following the replacement of the devices.

The current study aims at addressing the limitations of the previous studies on EASt-CRMWs. First, this study focuses on investigating the replaceability of the energy dissipation devices and the ability to obtain similar responses with new devices installed at the base of the walls. As such, two half-scale two-story EASt-CRMWs were constructed and each tested multiple times with new sets of flexural yielding energy dissipation devices. One of the walls was constructed identically to that of the first phase reported by East et al. (2022c), while the second wall was constructed with minor adjustments to the rocking toe region of the wall by adding a steel plate between the rocking interface of the wall and the foundation in order to avoid damage to the mortar layer. Second, the study validates the ability of the nonlinear OpenSees model developed by East et al. (2022a) to capture the performance of the EASt-CRMW system, as well as the ability of the damage index that was proposed by East et al. (2022a) to predict the damage to these walls.

5.3 Experimental Program

5.3.1 Test Matrix

The two walls tested in this study had the same overall geometry, as shown in Figure 5.1. Both walls were constructed by a professional mason using half-scale concrete block units (90 x 90 x 185 mm). The joints were scaled to 5 mm and constructed using a 50% running bond. To accommodate the horizontal reinforcement, the masonry units' webs were notched to a depth of 20 mm.

The first wall, Wall 1, was designed to have the same lateral load capacity as the ED-CRMWs tested by Yassin et al. (2022a) and the EASt-CRMWs tested by East et al. (2022c). The vertical reinforcement comprised D7 and M10 bars that were welded to the steel base component at the locations indicated in Figure 5.1. Vertical reinforcement ran continuously over the height of each wall to avoid lap splices and to limit the number of test parameters to be considered. The horizontal reinforcement consisted of a D4 bar placed at every other course. The horizontal reinforcement formed 180ooks around the outermost vertical bars. Confinement plates, cut from mild steel of 1.5 mm thickness, were placed in the first four courses at the bed joints of the toe regions to increase the strain capacity of the critical rocking toe regions. Four flexural arms were used, two placed symmetrically on each side. The flexural arms had a length of 315 mm and a thickness of 15.88 mm, and they were cut from Grade 44W steel using a water jet cutter. Each of the flexural yielding devices was connected to the foundation using two Hilti HDA M16x190 undercut anchors, as shown in Figure 5.1. The wall was intended to be retested using a replacement set of flexural arms but the

same anchors at the base of the wall. The devices were pinned to the wall at a distance of 655 mm from the wall centerline. The wall was loaded with an axial stress of 1.17 MPa, representing normal intensity gravity loads.

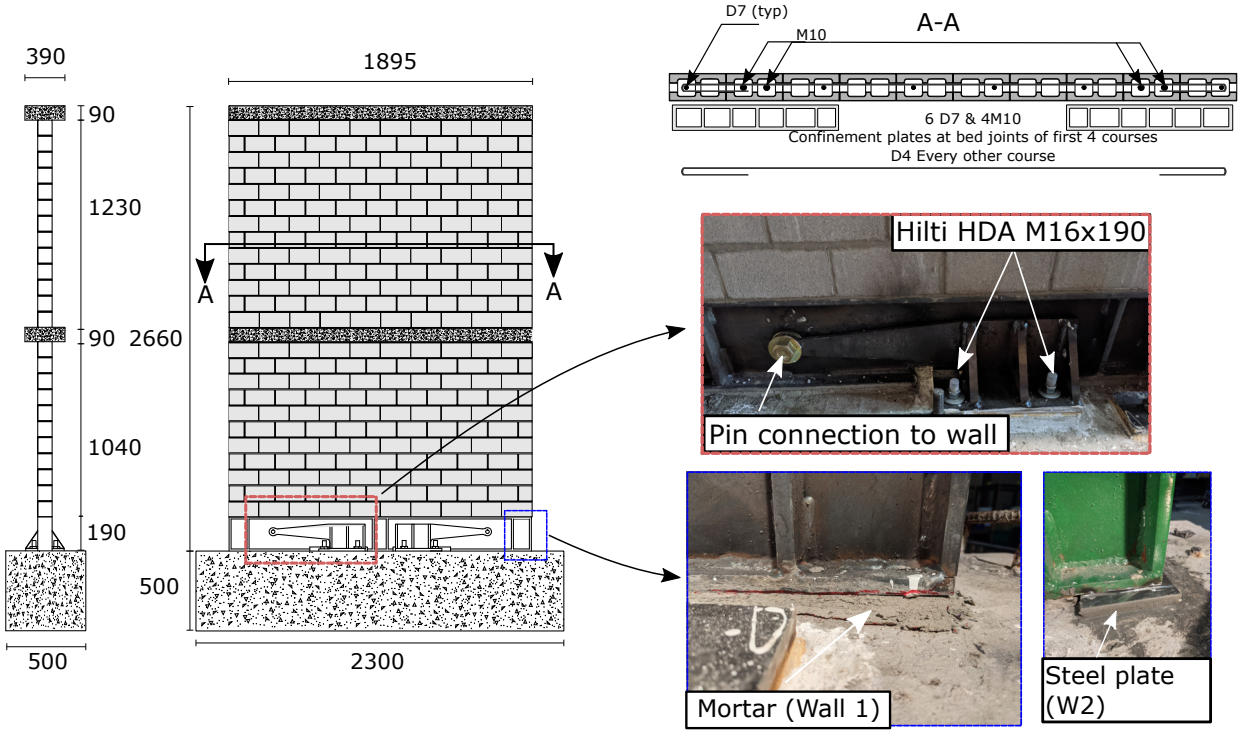

Figure 5.1: Wall geometrical and construction details

The second wall, Wall 2, was constructed identically to Wall 1, except that a steel rocking plate was epoxied to the foundation between the steel base and the foundation in place of the mortar at the end 100 mm of the interface, as shown in Figure 5.1. This was performed to minimize any potential damage to the mortar joint throughout testing and to investigate the influence that damage to that joint can have on the response of the walls.

5.3.2 Design Criteria

The walls were designed to reach a peak force when the flexural arms reached their design yield forces, with the wall's capacity designed based on this limit state. The flexural strength of the walls was calculated based on a sectional analysis of the cross-section directly above the steel base, assuming a linear strain distribution. An equivalent stress block with depth a was calculated using Eq. 5.3.1, which is a version of the equation provided by TMS (2016) that is modified to include the yield force (F_y) of the flexural arms. Eq. 5.3.2 was developed by East et al. (2022b) to predict this yield force. The flexural strength of the walls was then calculated using Eq. 5.3.3.

$$a = \frac{\sum_{i=1}^{n} F_{y_i} + P}{0.8 f'_m t_w} \tag{5.3.1}$$

$$F_y = \frac{4}{27} \frac{b^2 t \sigma_y}{h} \tag{5.3.2}$$

$$M_n = \sum_{i=1}^{n} F_y (d_i - \frac{a}{2}) + P \frac{L_w - a}{2} \tag{5.3.3}$$

where b is the largest depth of the tapered flexural arm; t is the thickness of the device; h is the length of the flexural arm; σ_y is the yield stress of the steel; f'_m is the masonry compressive strength; and t_w is the thickness of the wall. The walls were designed to have the flexural arms reaching an ultimate stage significantly past yielding without having shear or sliding shear failures in the masonry wall. As such, the walls were designed to have shear and sliding resistance much higher than the lateral load corresponding to the flexural strength, exceeding two times the nominal flexural capacity of the

wall. The shear strength of the walls was calculated with Eq. 5.3.4, following provisions from the TMS (2016) for fully-grouted reinforced masonry walls.

$$V_n = 0.083 \left(4.0 - 1.75\frac{M}{Vd_v}\right) A_{nv}\sqrt{f'_m} + 0.25P + 0.5\frac{A_v}{s} f_y d_v \qquad (5.3.4)$$

where d_v is the shear depth (assumed to be 0.8 L_w); A_{nv} is the shear area; A_v is the shear reinforcement cross-sectional area; f'_m is the compressive strength of masonry in MPa; s is the shear reinforcement spacing; and f_y is the shear reinforcement yield strength.

5.4 Construction Details

Walls 1 and 2 were constructed to imitate how the walls would be constructed in practice. First, the steel rocking base was fabricated, and placed upon the foundation on a layer of mortar to even out any irregularities on the foundation and level the steel base. For Wall 2, steel plates (3.175 mm thick) were epoxied to the foundation and used in place of mortar for the 100 mm at the ends of the steel base as discussed earlier. Next, the anchor locations were drilled into the foundation and the flexural arms were connected to the foundation and the rocking base. The vertical reinforcement was then welded to the steel base. The wall was then constructed by certified masons, with each half story being fully grouted, and the floor slabs being cast between build days. The intention was to have the workflow altered as little as possible from a traditional construction site. This was mostly achieved as the only differences between a conventional construction sequence and the one used in this study

is in the installation of the steel base, the flexural arms, and the welding of the vertical reinforcement to the steel base, all of which could be subcontracted out. Above the steel base, the construction process is nearly identical for the masons involved to that of a conventional reinforced masonry shear wall, aside from the inclusion of confinement plates in the first four courses of the walls of these tests, which may not be necessary based on the results reported by East et al. (2022c).

5.5 Material Properties

Type S mortar was used to build the walls with an average thickness of approximately 5 mm for each mortar joint. Three mortar cubes were taken from each batch used during construction. The mortar cubes were then tested under compression in accordance with CSA A165-14 (CSA 2014a) to determine their average compressive strength. Additionally, a flow test was conducted on each batch of mortar prepared following CSA A179-14 (CSA 2014a). Three half-scale blocks were capped and tested under compression in accordance with CSA A165-14 to determine their average compressive strength. Grout was mixed with the proportions of 1:3.9:0.85:0.04 of cement:sand:water:lime. Three cylinders were taken from each grout batch, for a total of six cylinders, and were cured for 30 days before testing them in compression following CSA A179-14 (CSA 2014a). Cylinders were also taken from the foundation concrete, as well as each inter-story slab, and tested according to CSA A23.2-14 (CSA 2014b). Three prisms of four blocks high by one block long were constructed from each batch of mortar during construction and were tested in accordance with CSA S304-14 to determine

f'_m (CSA 2014c). The reinforcement used within the walls was also tested in tension following CSA G30.18 (CSA 2014d). Three coupons were taken from each plate used to fabricate the flexural arms and tested in accordance with ASTM A370 (ASTM 2013). The resulting material properties are summarized in Table 5.1.

Table 5.1: Material Properties

Material Test	Average Value	C.o.V. (%)
Type S mortar	19.9 MPa	8.9
Percentage flow test	126.6%	14.3
Grout cylinder	23.6 MPa	9.6
Half-scale block	25.4 MPa	2.9
Inter-story floor slab concrete	26.5 MPa	2.5
Footing foundation concrete	32.4 MPa	1.7
4 course running bond prism	11.5 MPa	9.8
D4 reinforcement	504 MPa	3.1
D7 reinforcement	462 MPa	3.6
M10 reinforcement	479 MPa	4.4

Equation 5.3.2 was used to calculate the yield force of each of the sets of flexural arms used for each of the five tests. Due to the size limitations of the water jet cutter used, the devices were cut from different pieces of steel, which resulted in some material variation across the sets of devices. The expected yield forces are summarized in Table 5.2.

Table 5.2: Expected yield forces for the flexural arms (based on Eq. 5.3.2)

Specimen	F_y (kN)
Wall 1 Test 1	20.8
Wall 1 Test 2	21.1
Wall 1 Test 3	21.3
Wall 2 Test 1	23.9
Wall 2 Test 2	23.2

5.6 Test Setup

The test setup used for this study is depicted in Figure 5.2. The reinforced concrete footing for each wall was mounted to the strong floor of McMaster University's Applied Dynamics Laboratory with a layer of mortar to ensure the wall was level. The walls were constrained in the out-of-plane direction at the first and second story slabs using a roller system at four points on each slab, as shown in Figure 5.2. At the top of the walls, a rigid steel loading beam was mortared to the slab. Six 25 mm steel dowels were cast in the open cells of the wall and protruded above the top slab. These protruding rods were subsequently welded to the loading beam to facilitate a uniform transfer of load between the wall and the loading beam. The gravity load was simulated using two hydraulic jacks attached at the top of the wall using two 25 mm high-strength rods, attached through a box section atop the loading beam.

5.7 Instrumentation

Vertically mounted linear potentiometers (V1-V17) were used to measure vertical displacements at various locations on each wall specimen, as indicated in Figure 5.3. All vertical potentiometers were mounted on the South face of the wall (see Figure 5.3). Five vertical potentiometers (V1-5) were mounted 240 mm from the wall-foundation interface to measure the gap opening at the base of the wall. One vertical potentiometer was attached to the pinned end of the flexural arms (V6-7), while the remaining ten vertical potentiometers (V8-17) were used to determine the curvature along the wall height. Lateral displacements were monitored through four horizontally

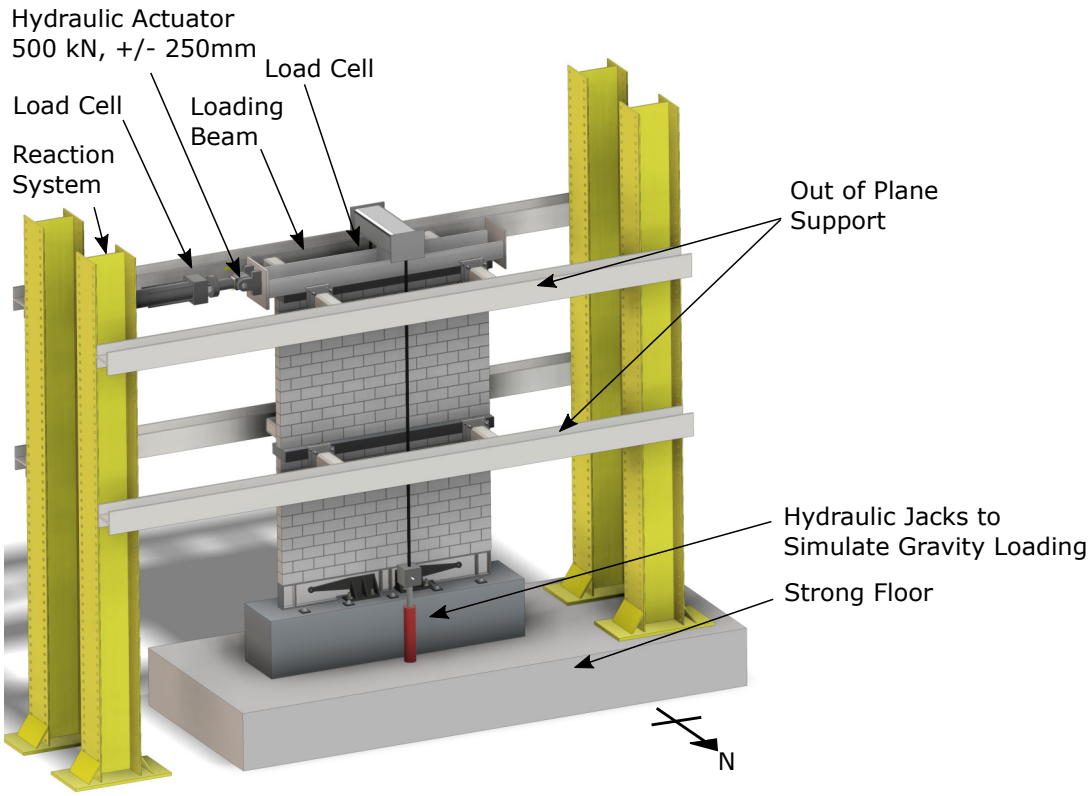

Figure 5.2: Test setup

mounted linear potentiometers (H1-4), while the remaining two horizontal potentiometers (H5-6) were used to measure relative sliding between the wall and the base footing of each wall, as well as between the footing and the laboratory foundation.

In addition to this, each outermost vertical reinforcement bar had three strain gauges (S1-6) at 50 mm, 100 mm, and 200 mm from the steel connection interface in order to assess if the reinforcement remained elastic throughout testing. Two additional strain gauges (S8-9) were used on the first and third transverse reinforcement bars, midway across the wall. Three strain gauges (S10-16) were used on the upper side of each of the flexural arms to determine when yielding first occurred in such devices.

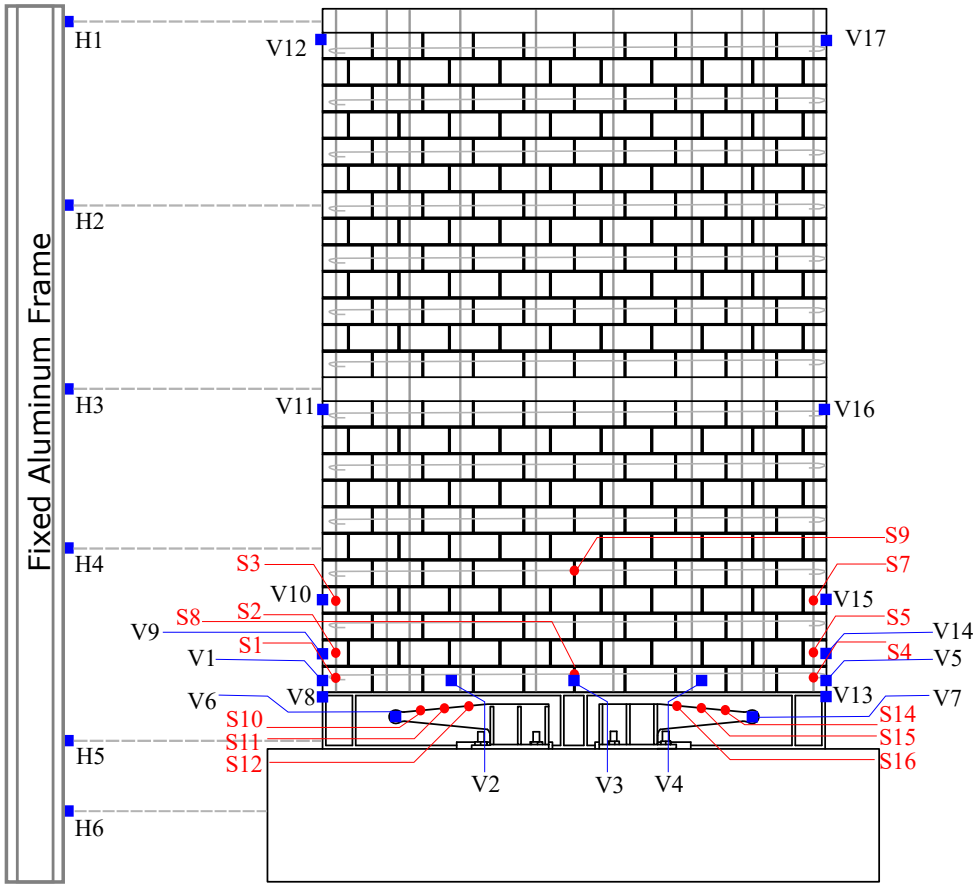

Figure 5.3: Instrumentation Plan

5.8 Testing Procedure

The loading protocol used was the FEMA 461 (FEMA 2007) quasi-static testing protocol, as shown in Figure 5.4. The loading protocol was adopted based on the protocol used by East et al. (2022c) in a previous study of EASt-CRMWs to allow for direct comparison. In the loading protocol, each cycle was repeated twice, and each subsequent cycle increased by 40% from the previous cycle. After reaching the ultimate displacement, each subsequent cycle amplitude was increased by 30%. Each test was terminated when the wall reached 2.4% lateral drift, to represent a very high level of

displacement demand, but not the full capacity of the system, as this study investigates the replaceability of the flexural arms.

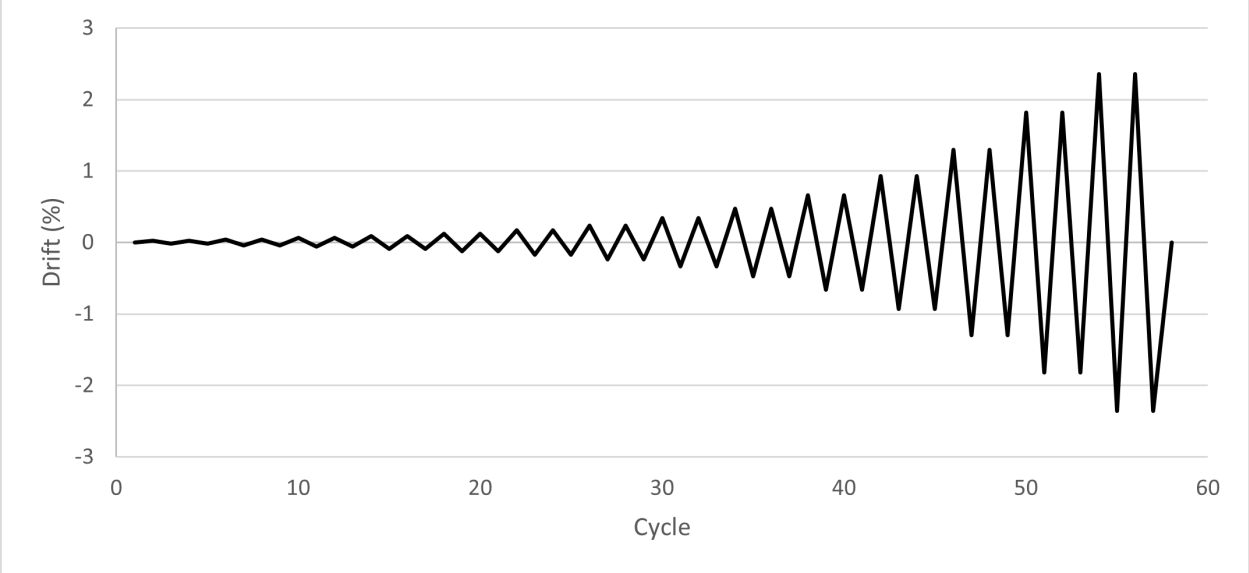

Figure 5.4: FEMA 461 Loading Protocol (FEMA 2007)

5.9 Test Results

5.9.1 Damage Sequence and Failure Modes

This subsection discusses the observed response and sequence of damage for the walls in their initial tests, and in tests of the repaired walls with new flexural arms. The drifts discussed are normalized by 2.51 m, which is the height of H1 relative to the base of the wall.

Initial Test of Walls 1 and 2

Figure 5.5 displays photos of key stages in the overall response of Wall 1. The rocking mechanism was first observed at a drift ratio of 0.08%. At this point,

the flexural arms began to engage, with compressive strains being recorded using SG10-16. The layer of mortar that was placed between the steel base and the foundation was observed to start crushing at a drift ratio of 0.10%, with the crushing moving towards the center of the wall as the drift increased. The flexural arms reached their yield strain at a drift ratio of 0.70%, as indicated by the readings from strain gauges SG 10-16. Hairline cracks appeared at the first three bed joints at a drift ratio of 0.92%; however, even at larger drifts, these cracks did not propagate past one-third of the wall length. In the final cycle, reaching a lateral drift ratio of 2.4%, there were still no significant signs of damage to the masonry, with only minimal hairline cracks at the first four bed joints. The strain in the flexural arms reached over 6.5 times the yield strain with no signs of buckling. At this drift ratio, neither of the outermost reinforcing bars reached a yield strain, with the highest reading in SG 1-6 being 1583 με. The layer of mortar below the steel base was completely crushed within the outer 150 mm of the ends of the rocking toes, as shown in Figure 5.5, while no other damage or signs of strength degradation were observed in the test. At the end of the test, the only source of significant damage was concentrated in the flexural arms, displaying the effectiveness of the system at localizing damage to the repairable energy dissipation devices.

Figure 5.5: Photos of Wall 1 during the first test

Wall 2 had a nearly identical response to Wall 1, which was expected as there is very little difference between the two walls with the exception of the steel plate replacing the mortar joint at the rocking toes between the steel base and the foundation. Uplift was observed at the same drift ratio, with the first signs of base joint opening at a drift ratio of 0.08%. The flexural arms reached

a yield strain at a drift of 0.73%. The strain in the flexural arms reached more than 6.5 times the yield strain with no signs of buckling, and the outermost reinforcement remained elastic, with a maximum strain of 1785 με. Notably, the steel plate at the rocking toe suffered no damage, and the mortar joint adjacent to the steel plate exhibited no signs of crushing.

Replacement of Flexural Arms

To evaluate the seismic resilience of the EASt-CRMW system, the flexural arms on Walls 1 and 2 were replaced by new arms with the same properties and dimensions. The replacement was performed with the axial loads still applied, to be representative of a real replacement scenario. The stages of replacing the flexural arms are displayed in Figure 5.6. The yielded flexural arms were cut off with an angle grinder as the plastic deformation made removal of the pin difficult. Following this, the rest of the flexural arm was lifted out, and the new one was installed on the same anchor bolts and pinned into the wall. This process was repeated for all four arms of each wall. The entire process was completed by a single person in under four hours, highlighting the benefits of the system and the simplicity of the repair process. Afterward, the walls were retested (each test with new flexural arms) under the same loading protocol. Wall 1 was tested a total of three times, while Wall 2 was tested twice.

Figure 5.6: Replacement of the flexural arms

Subsequent Tests of Wall 1

The response of Wall 1 during the second test followed a very similar sequence as the first test. Specifically, the rocking joint opened at a drift of 0.08%. The flexural arms reached a yield strain at a lateral drift of 0.93%, slightly later than that during the first test. The hairline cracks that formed during the first test did not propagate further throughout test 2. During the final cycle, the flexural arms reached a slightly lower strain than that in test 1, with an average of 6 times the yield strain, while still displaying no signs of buckling. The rocking joint behavior was influenced by the crushed layer of mortar at the interface between the steel base and the foundation, which caused the decompression point to move in slightly from the rocking toe. The

outermost vertical reinforcing bars remained elastic throughout the test, with the largest strain reaching 1694 με. At the end of the test, no significant damage was observed aside from the inelastic deformation concentrated in the flexural arms.

The response of Wall 1 during the third test remained very similar to the first two tests, with the yield drift of the flexural arms being slightly later, at a lateral drift of 0.98% in the final test. The same hairline cracks were present; however, these cracks did not propagate further during the third test. The mortar at the interface between the steel base and the foundation was crushed more, further moving the location of the rocking point and causing the outermost reinforcement to reach a peak strain of 1893 με, yet still in the elastic range. Even at the end of the third and final test, the only significant damage was within the flexural arms and at the mortar joint between the steel base and the foundation.

Subsequent Tests of Wall 2

Wall 2 showed a very similar response in its second test to that of the first test. The rocking mechanism was first observed at a drift ratio of 0.09%. The flexural arms reached a yield strain at a lateral drift of 0.79%, which was closer to the first test than for tests 2 and 3 of Wall 1, which exhibited yielding at delayed drifts. This is attributed to the grout layer adjacent to the steel plate remaining undamaged in the second test, which caused the rocking point to remain consistent between each test. The flexural devices reached approximately 6.5 times their yield strain in the second test, the same as the first. The outermost vertical reinforcing bars remained elastic, with a peak strain of 1865 με.

5.9.2 Force-Displacement Response

Figure 5.7 plots the force measured by the load cell of the hydraulic actuator against the displacement measured by the topmost horizontal potentiometer (H1) for each of the tests of Walls 1 and 2. The tests all displayed a hysteretic response characteristic of a controlled rocking system, with a change in stiffness when the rocking mechanism is initiated and the flexural arms begin to deform. As can be seen from the figure, neither wall exhibited any sign of strength degradation throughout any of the tests. Each wall recorded its peak force at the maximum displacement. Wall 1 reached peak forces of 104, 104 and 103 kN in the three tests, respectively, while Wall 2 peaked at 112 and 110 kN.

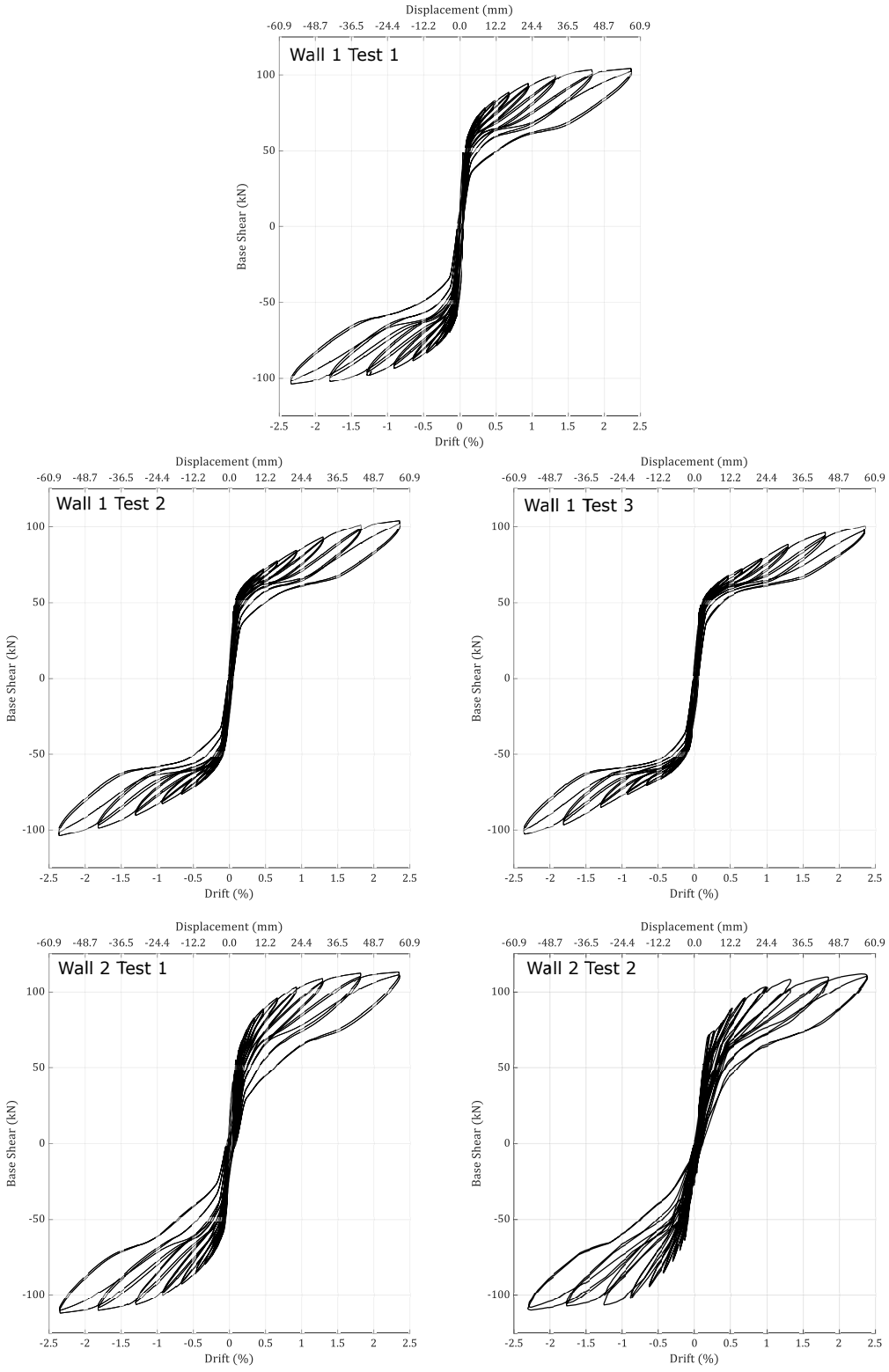

Figure 5.7: Hysteretic response of walls 1 and 2 for each test

In Wall 1, the earlier displacement cycles have a somewhat lower peak force in each consecutive test, despite reaching comparable peak strengths during the final cycle. Wall 1 experienced an average of a 16% reduction in peak force in the displacement cycles prior to 1% lateral drift during test 2, and a further 5% reduction (21% total compared to test 1) for test 3. In later cycles, with drifts exceeding 1%, this reduction is only 4% and 7% in comparison to the initial test. Figure 5.8 displays the envelopes of the force-displacement relationships for each test, where the reduction is greatest in lower amplitude cycles. This reduction is attributed to the damage to the mortar joint, which resulted in a slightly lower uplift moment due to a shorter moment arm. Conversely, this reduction is not observed in Wall 2, where there was only an average reduction of 2% in peak force prior to reaching 1% lateral drift. The peak forces for Wall 2 remained within 2% for all drifts, with some even slightly exceeding the peak force compared to the first test, suggesting essentially zero damage to the wall. These results demonstrate that the steel plate installed at the rocking interface was effective at preventing the progressive crushing of the mortar joint, and subsequently prevented the reduction in forces.

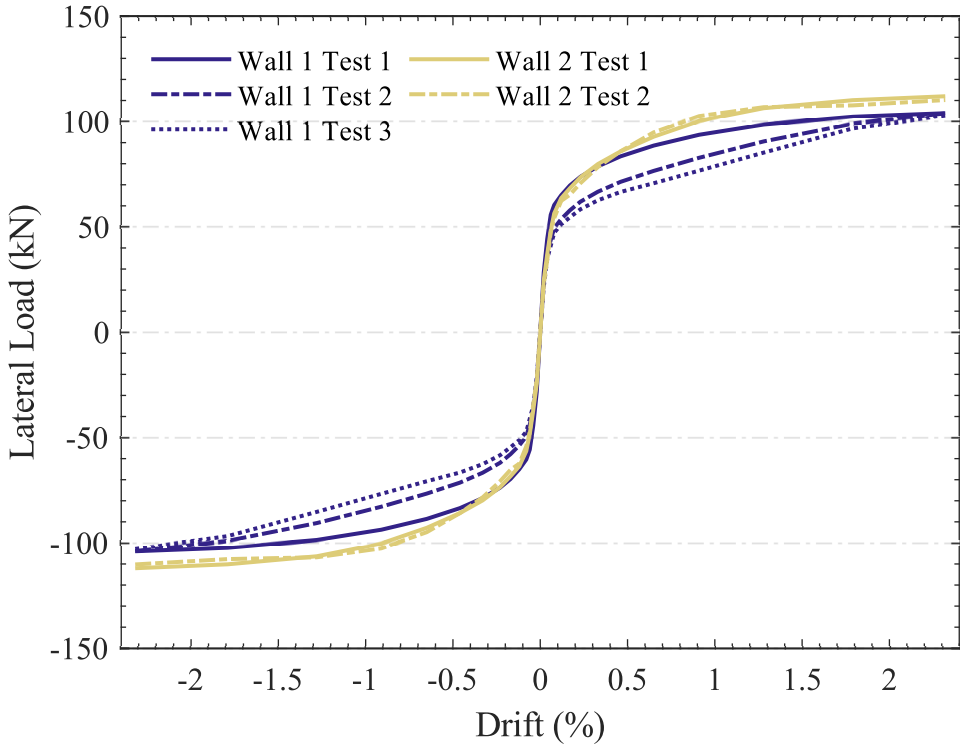

Figure 5.8: Envelope response of walls 1 and 2 for each test

5.9.3 Residual Drift Ratio

To quantify the self-centering capability, the residual drift was recorded at the end of the first displacement cycle in both the push and pull directions. Figure 5.9 displays the maximum residual drifts of each wall after each cycle in each test. The residual drifts for Walls 1 and 2 remained below 0.05% for all displacement cycles in the test. For comparison, a residual drift of 0.2% is considered acceptable as it represents the limit for damage state 1 (DS1, no structural realignment or repair) as defined in FEMA P-58 (Applied Technology Council 2018).

Upon replacement of the flexural arms and subsequent retesting of the walls, there was no consistent difference in the self-centering capacity of the

walls. The walls maintained residual drifts below 0.05%, highlighting the effectiveness of the replaceable, externally mounted flexural arms.

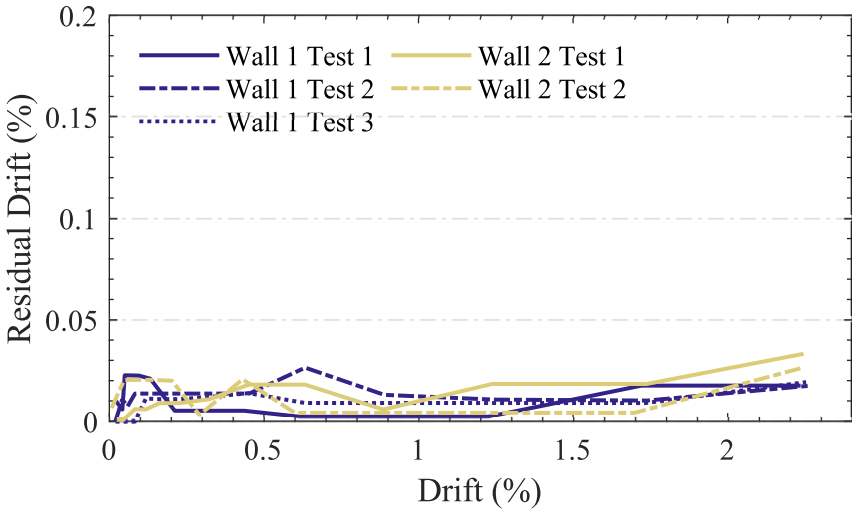

Figure 5.9: Residual drifts of walls 1 and 2 for each test

5.10 Numerical Model Validation

As indicated in the introduction, a numerical model was developed by East et al. (2022a) to propose the EASt-CRMW system and predict its low damage. That study highlighted the need to validate both the numerical model and the corresponding predictions of low damage that were made with a damage index proposed for masonry walls. Therefore, this section evaluates the application of that model and damage index to experimental results for EASt-CRMWs.

5.10.1 Modelling Approach

Figure 5.10 shows a schematic of the OpenSees model developed to capture the response of EASt-CRMWs. This model is discussed in detail in East et

al. (2022a), where it was validated against post-tensioned CRMWs, as well as a single ED-CRMW test by Yassin et al (2022b). As can be seen in the figure, the masonry is modelled using a series of 4-node, multi-layered shell elements with smeared layers to account for the vertical and horizontal reinforcement present in the wall, atop a base of compression-only springs. The masonry layers were assigned a modified Kent-Scott-Park stress-strain material model that is available as Concrete01 in OpenSees (Mazzoni et al. 2006). The parameters specified for the masonry material layers are defined by the compressive strength, tensile strength, crushing strength, strain at maximum strength, strain at crushing strength, ultimate tensile strain, and shear retention factor. The reinforcing bars were modelled as smeared layers of equivalent thicknesses, designated as PlateRebar following the Giuffre-Menegotto-Pinto model with isotropic strain hardening (referred to as Steel02 in OpenSees). The elastic modulus was taken as 200 GPa, while the strain hardening ratio was set to 1%. The remaining constants of *R0*, *CR1* and *CR2* were set to 18.5, 0.925 and 0.15, respectively.

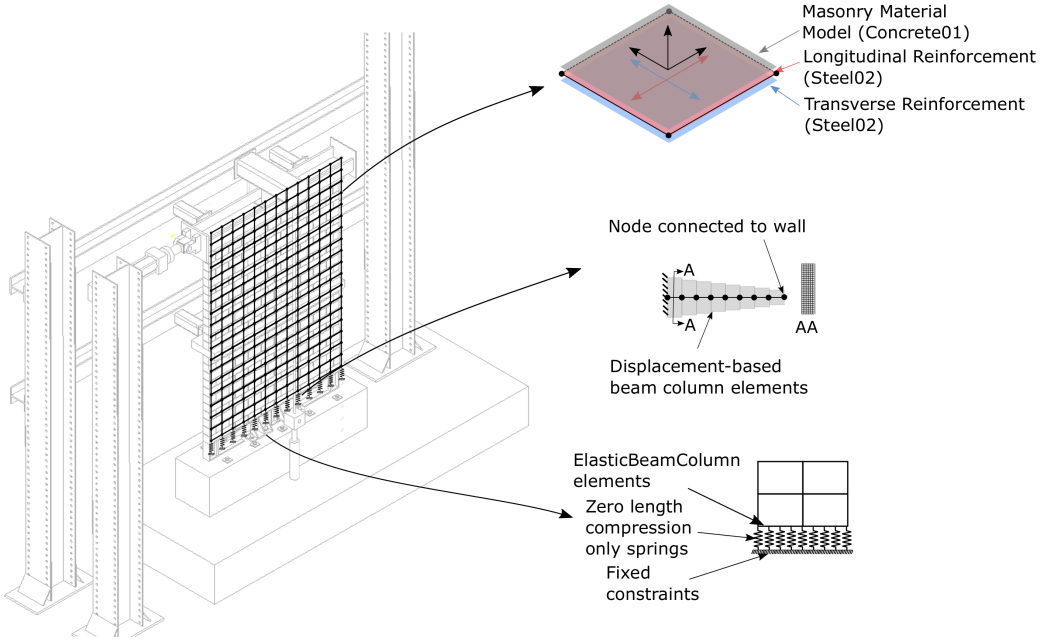

Figure 5.10: Schematic of the OpenSees model

The rocking interface shown in Figure 5.10 at the base of the wall is modelled with a series of zero-length, compression-only springs. The spacing between the springs was limited to a maximum of 12 mm in order to avoid convergence issues within the model. As there are significantly more springs than shell elements at the wall base, the nodes that align with the shell elements are connected directly to the springs, while the remaining springs are connected to the shell elements through a series of elastic beam-column elements, as shown in Figure 5.10. The layer between the steel base and the foundation was not modelled, so the model of the rocking interface was identical for Walls 1 and 2.

The flexural arms are modelled following the technique that was developed and validated by East et al. (2022b) based on a set of 14 experimental device tests by Li et al. (2019). The devices are modelled using a series of displacement-based fiber elements in OpenSees. Figure 10 shows

the flexural arm model incorporated into the CRMW model. Additional details regarding the modelling approach and validation can be found in East et al. (2022a). The slightly different strengths of the flexural arms for each test (Table 5.2) were the main difference among the models of the five different tests.

5.10.2 Modelled Walls

The experimental wall tests described in the current study were modelled, in addition to two walls from a previous study by East et al. (2022c). The details of each of the additional walls are shown in Table 5.3. The additional EASt-CRMWs from East et al. (2022c) investigated additional parameters beyond those of Walls 1 and 2 of the current study, namely the axial load ratio and the aspect ratio, as shown in Table 5.3.

Table 5.3: Details of additional walls from East et al. (2022c)

Parameter	East et al. (2022c) EASt-CRMW4	East et al. (2022c) EASt-CRMW7
hw	2660 mm	2660 mm
lw	1895 mm	1295 mm
Axial Stress	2.31 MPa	1.17 MPa
ρ_v (%)	0.36	0.36
ρ_h (%)	0.70	0.70
Confinement[i]	yes	yes
F_y[ii]	23.6 kN	23.6 kN

[i]the same arrangement of confinement plates was used as in Wall 1 and Wall 2 of the current study
[ii]design yield force from Eq. 5.3.2

5.10.3 Comparison of Model to Experimental Results

Figure 5.11 displays the hysteretic response of each of the walls. As can be seen in the figure, the model is able to simulate the experimental results such

as initial stiffness, ultimate strength, and overall hysteretic shape to a high degree of accuracy, indicating that the proposed modelling technique is effective at simulating the performance of EASt-CRMWs. The peak forces recorded by the model are within 2% of the experimental results, while the total energy dissipated was accurate within 7% for walls, with the model slightly underestimating the real energy dissipation.

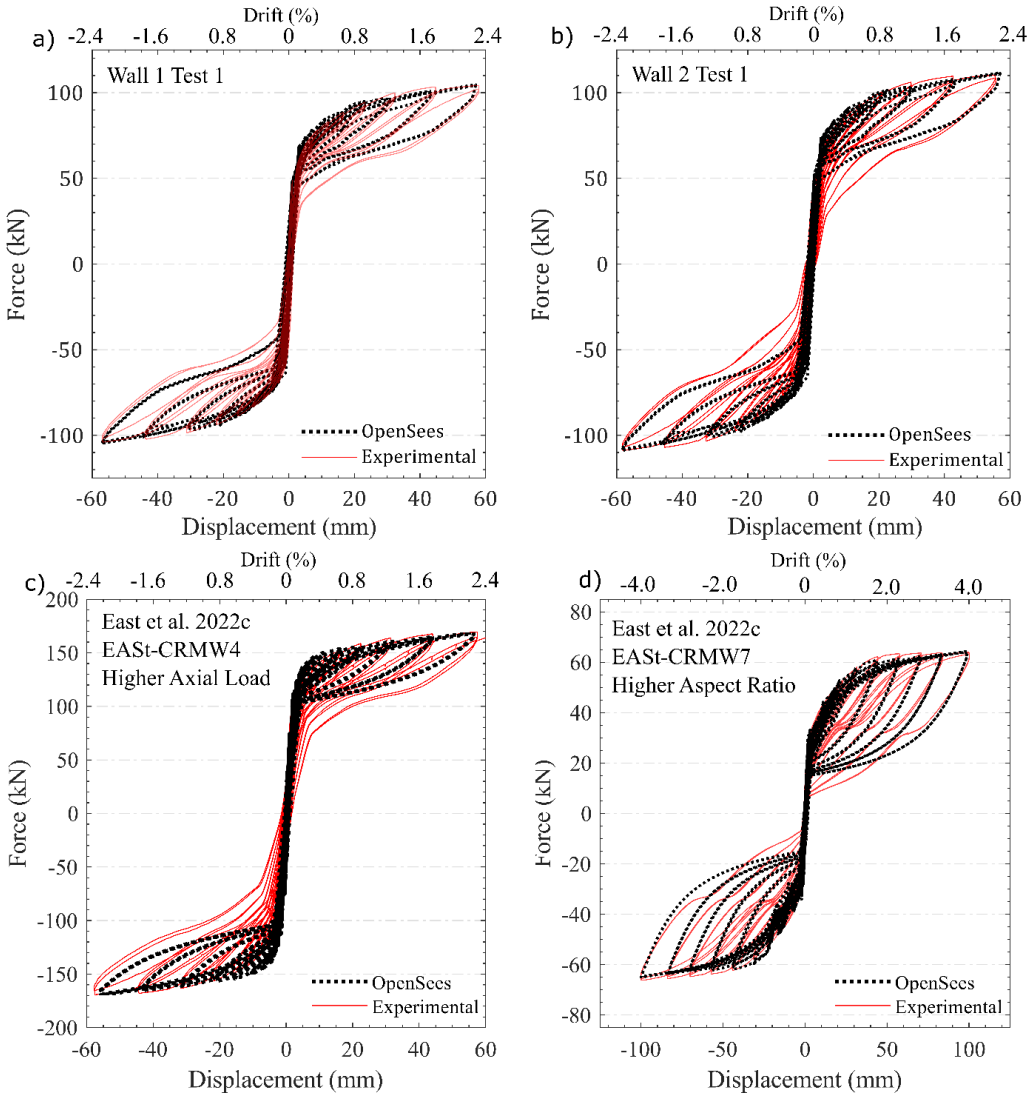

Figure 5.11: Numerical and experimental force-displacement response for a) Wall 1; b) Wall 2; c) EASt-CRMW4 (East et al. 2022c) d) EASt-CRMW7 (East et al. 2022c)

There are some limitations to the model proposed, leading to the discrepancies between the modelled responses and the experimental responses. As the mortar joint between the steel base and the foundation is not explicitly modelled, the model is not able to capture the reduced response observed upon retesting the walls due to the progressive crushing of the mortar at that interface. Similarly, the model tends to overestimate the force in the unloading portion of the hysteretic response due to the crushing of the mortar causing the neutral axis to move inward, resulting in a more curved unloading response. Finally, there is an additional slight irregularity on the return cycles of the experimental walls due to the sliding of the Hilti anchors used to install the flexural arms producing a small amount of slack in the system when it transitions into tension. This effect is also not captured by the numerical model, as fixed boundary conditions were used in the model.

5.11 Damage Index Validation

As discussed in the introduction, East et al. (2022a) proposed a damage index for reinforced masonry walls and used it to develop the concept of EASt-CRMWs, but no experimental data were available to verify the predictions of reduced damage for that case. The damage index takes the maximum of a compressive damage index, based on one developed for reinforced concrete walls by Kim et al. (2005), and a new tensile damage index. The compressive damage index is calculated using a failure criterion based on the principal compressive strains in relation to the ultimate compressive strains, with additional consideration of low cycle fatigue. The

tensile damage index is defined based on the ultimate masonry strain in tension, specifically for modelling techniques in which the reinforcement is smeared, such that tensile splitting effects in the masonry are captured. The overall DI value is taken as the maximum value between the compressive and tensile DI values. More detail on the calculation of the DI values can be found in East et al. (2022a). Table 5.4 links the DI values to the terminology in FEMA P-58 (Federal Emergency Management Agency 2018) for masonry structures for three Damage States (DS1-3).

Table 5.4: Damage State Definitions as proposed by East et al. (2022a)

Damage State	Damage Index Value	Description
DS1 – Minor/repairable damage	$0.1 \leq$ DI ≤ 0.4	Hairline cracks, aesthetic compressive damage
DS2 – Moderate damage	$0.4 <$DS2 ≤ 0.7	Tensile cracks exceeding 0.1mm, but less than 1 mm, repairable but not insignificant compression failure (face shell spalling/ cracking)
DS3 – Severe damage	DI ≥ 0.7	Complete failure (compressive crushing, large tensile cracks exceeding 1 mm in width)

Figure 5.12 compares the DI results of the initial test of Wall 1 to the damage observed throughout the test based on observations reported earlier in this study. The DI results in Figure 5.12b align with the low damage experimentally observed in Wall 1 (Figure 5.12a), with a maximum DI value of 0.35, only slightly lower than the the value of 0.4 expected to develop cracks exceeding 0.1 mm (Table 4). However, comparing to a wall with more

damage is still necessary to further validate the damage index at higher damage states. Therefore, Figure 5.13 compares the DI results for wall EASt-CRMW4 from East et al. (2022c) to the damage observed throughout the test of the wall, based on both visual observations and a digital image correlation (DIC) software, GOM Correlate (GOM 2016). More details on the DIC technique can be found in East et al. (2022c). As this wall was loaded with a considerably higher axial load (double that of the other walls in the test matrix), considerably more damage was observed throughout the test, making it the most appropriate wall to assess the DI accuracy. Figure 5.13a shows the DIC results during the last drift cycle, which were used to measure the width of cracks and observe other signs of damage, while Figure 5.13b shows a schematic of the wall with all tensile cracks exceeding 0.1 mm (all cracks remained below 1 mm), and repairable but not insignificant compressive damage, corresponding to DS2 from Table 5.4. As can be seen in Figure 5.13c, the damage index captures the location and extent of cracking within the tensile region of the wall, as well as the moderate amount of crushing damage and face shell spalling in the compressive rocking toes of the wall.

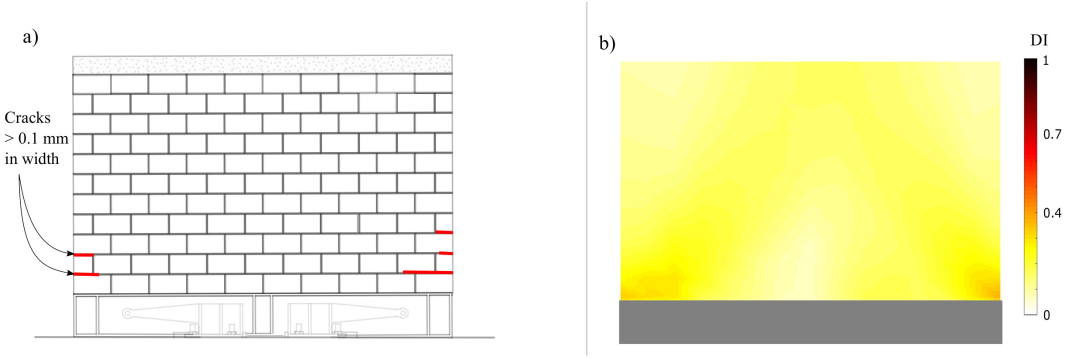

Figure 5.12: Damage index compared to experimental results of wall 1; a) schematic of observed damage through final drift ratios; b) DI predictions

The damage index was evaluated for all the tests discussed in the current study, with Table 5.5 summarizing peak compressive index (DI_C) and tensile index (DI_T) values at 0.5% drift, 1% drift, and the maximum drift ratio reached throughout testing. The DI values, interpreted as damage states using the ranges proposed in Table 5.4, are generally in agreement with the observed damage. DS1 is difficult to validate, as hairline cracks can be too fine to distinguish through visual inspection. No hairline cracks were observed in walls 1 and 2 at a drift ratio of 0.5% despite the tensile damage index slightly exceeding 0.1; however, in EASt-CRMW7, hairline cracks were observed at this drift ratio, consistent with the DI_T value that exceeded 0.2. As shown in Figure 5.13, in EASt-CRMW4, tensile cracks exceeding 0.1 mm were observed, aligning with the value of 0.4 (DS2) at a drift ratio of 0.5%. No compressive damage was observed in the tests at this damage ratio, and the low DIC values in Wall 1, Wall 2, and EASt-CRMW of 0.097, 0.098, and 0.066 reflect this; however, no signs of aesthetic compressive damage were observed in EASt-CRMW4, despite DIC exceeding 0.1. At a drift ratio of 1%, hairline cracks were visible in Wall 1, Wall 2 and EASt-CRMW7, and the corresponding DI_T values align with these observations, all within the range of DS1 (0.1 – 0.4). The cracks in EASt-CRMW4 were larger but remained below 1 mm in width, which is also consistent with the DIT value remaining within the DS2 range at this drift level. At each wall's peak drift ratio, Wall 1 and Wall 2 had cracks exceeding 0.1 mm in width (DS2) even though the DI_T values remained slightly below 0.4, at 0.353 and 0.351 respectively. EASt-CRMW4 experienced the first visible signs of compressive damage, with minor crushing at the rocking toes of the wall and minor face shell spalling, as displayed in Figure 5.13 and also represented accurately by the DIC exceeding 0.7, reaching a peak value of

0.756, with tensile cracks remaining below 1 mm, and a commensurate DI_T value of 0.379.

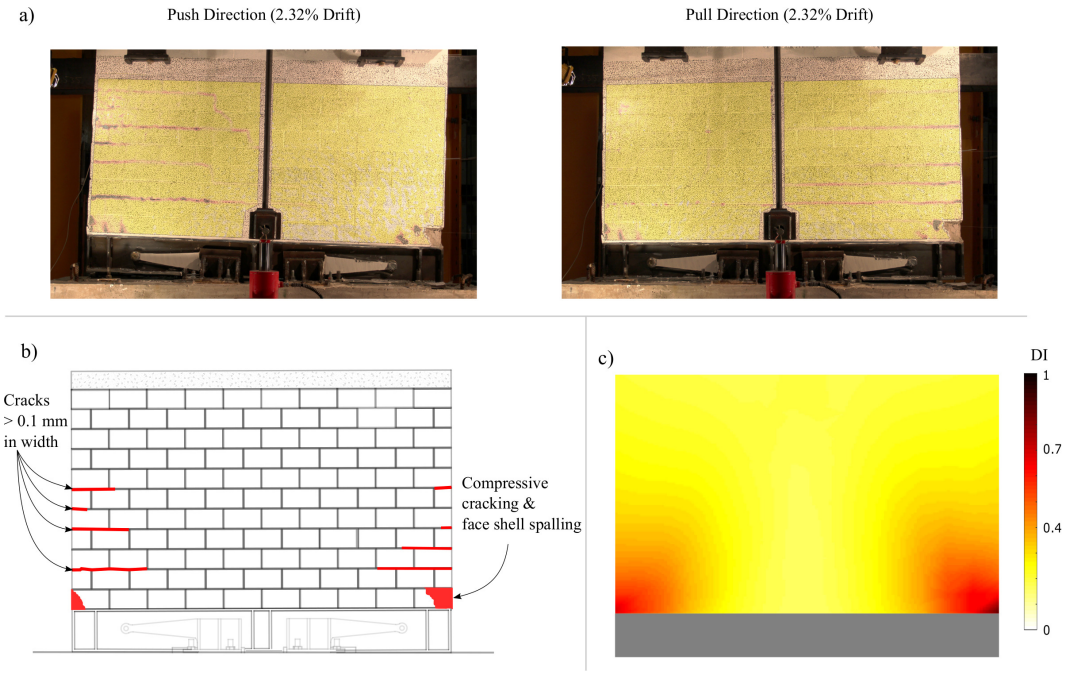

Figure 5.13: Figure 13 – Damage index compared to the experimental results of EASt-CRMW4 (East et al. 2022c); a) DIC results at final push and pull drift ratios; b) schematic of observed damage cumulative through final drift ratios; c) DI predictions

Overall, the damage index proposed by East et al. (2022b) predicted the location of hairline cracks, cracks exceeding 0.1 mm, and the extent of compressive crushing and compressive failure. The observed damage is generally consistent with the damage states outlined in Table 5.4, although there are some slight discrepancies, especially near the cutoffs between the discrete damage states. Because the walls achieved the intended low damage performance that the DI values predicted, validation of DS3 would require tests of a less resilient system in which more damage occurs.

Table 5.5: DI values for each of the walls modelled at various drift ratios compared to the observed damage

Drift Ratio		Wall 1	Wall 2	EASt-CRMW4 (higher axial load)	EASt-CRMW7 (higher aspect ratio)
0.5% drift	Max. DI_C	0.097	0.098	0.183	0.066
	Max. DI_T	0.121	0.122	0.398	0.201
	Observed Damage	no signs of compressive damage; no visible hairline cracks	no signs of compressive damage; no visible hairline cracks	no signs of compressive damage; cracks slightly exceeding 0.1 mm at some bed joints	no signs of compressive damage; no visible hairline cracks
1% Drift	Max. DI_C	0.097	0.098	0.189	0.078
	Max. DI_T	0.272	0.271	0.379	0.230
	Observed Damage	no signs of compressive damage; hairline cracks first visible	no signs of compressive damage; hairline cracks first visible	no signs of compressive damage; cracks exceeding 0.1 mm but less than 1 mm visible at multiple bed joints	no signs of compressive damage; hairline cracks first visible
Peak Drift[i]	Max. DI_C	0.105	0.103	0.756	0.105
	Max. DI_T	0.353	0.351	0.562	0.239
	Observed Damage	no signs of compressive damage; cracks exceeding 0.1 mm are visible	no signs of compressive damage, cracks exceeding 0.1 mm are visible	minor face shell spalling and crushing of the very end blocks on the rocking toe; cracks exceeding 0.1 mm are visibly larger and spreading inwards	no signs of compressive damage; hairline cracks spread inwards, but remain less than 0.1 mm in width

[i]the peak drifts were 2.4%, 2.4%, 2.9% and 5% respectively for each wall.

5.12 Conclusions

The current study reported the results of two controlled rocking masonry walls with external, accessible energy dissipation devices constructed atop a steel base (EASt-CRMWs). The two walls were tested under quasi-static cyclic loading to displacements exceeding 2% lateral drift, with residual drifts of less than 0.05% and no signs of damage in the masonry aside from hairline cracks at some bed joints. Following this, the energy dissipation devices were removed and replaced, and the walls were retested. A finite element model developed in OpenSees was validated to capture the response of this novel EASt-CRMW system. Finally, a proposed damage index for reinforced masonry walls was also validated against the experimental results for EASt-CRMWs. The experimental and numerical work presented in the current study provided the following conclusions:

- The proposed EASt-CRMW system is an extremely promising system with negligible damage and minimal residual drifts.
- The EASt-CRMW system allows for efficient replacement of the energy dissipation devices, thus minimizing any downtime a structure would experience following a seismic event.
- Such ED replacement restores the full initial system performance to within 2% of the peak force up to drifts of 2.4%.
- The use of a steel plate at the rocking toe prevents the crushing of mortar at that location, and subsequently prevents reductions in peak forces upon repair and repeated loading of the walls.

- The numerical modelling technique used is capable of capturing the response of the EASt-CRMW system to a high degree of accuracy, with peak forces captured to within 2%.
- The proposed damage index accurately predicts the location, extent and severity of damage in EASt-CRMWs.

5.13 Acknowledgements

The financial support for this project was provided through the Canadian Concrete Masonry Producers Association (CCMPA), the Canada Masonry Design Centre (CMDC), the Natural Sciences and Engineering Research Council (NSERC), and the Ontario Centres of Excellence (OCE).

5.14 Data Availability Statement

All data, models, and code generated or used during the study appear in the submitted article, are referenced accordingly, or are available at reasonable request.

5.15 References

ACI Innovation Task Group 5. 2009. "Requirements for Design of a Special Unbonded Post-Tensioned Precast Shear Wall Satisfying ACI ITG-5.1 (ACI ITG-5.2-09) and Commentary." American Concrete Institute, 1: 1–21.

Applied Technology Council. 2018. "FEMA P-58-1: Seismic Performance Assessment of Buildings. Volume 1 – Methodology." *Fema P-58-1*, 1 (December 2018).

ASTM (American Society for Testing and Materials). 2013. Mechanical Testing of Steel Products. A370. West Conshohocken, PA.

Banting, B. R., and W. W. El-Dakhakhni. 2014. "Seismic Performance Quantification of Reinforced Masonry Structural Walls with Boundary Elements." *Journal of Structural Engineering*, 140 (5): 04014001. https://doi.org/10.1061/(asce)st.1943-541x.0000895.

CSA (Canadian Standards Association). 2014a. *Mortar and grout for unit masonry*. CSA A179-14. Mississauga, ON: CSA.

CSA (Canadian Standards Association). 2014a. *Standards on concrete masonry units*. CSA A165-14. Mississauga, ON: CSA.

CSA (Canadian Standards Association). 2014c. *Design of masonry structures*. CSA S304-14. Mississauga, ON.

CSA (Canadian Standards Association). 2014d. *Carbon steel bars for concrete reinforcement*. CSA G30.18-09. Mississauga, ON.

CSA (Canadian Standards Association). 2014e. *Design of concrete structures*. A23.3-14. Mississauga, ON.

Dvorkin, E. N., D. Pantuso, and E. A. Repetto. 1995. "A formulation of the MITC4 shell element for finite strain elasto-plastic analysis." Computer Methods in Applied Mechanics and Engineering, 125 :1–4. https://doi.org/10.1016/0045-7825(95)00767-U.

East, M., Ezzeldin, M., Wiebe, L., 2022a. "Strategies to Reduce and Quantify Damage in Controlled Rocking Masonry Walls." *Journal of Structural Engineering.* Submitted. STENG-11851.

East, M., Li, J., M. Ezzeldin, and L. Wiebe. 2022b. "Development of a Flexural Yielding Energy Dissipation Device for Controlled Rocking Systems." *Journal of Structural Engineering.* https://doi.org/10.1061/(ASCE)ST.1943-541X.0003461

East, M., Ezzeldin, M., Wiebe, L., 2022c. "Development of Controlled Rocking Masonry Walls with Energy Dissipation in a Steel Base." *Journal of Structural Engineering.* Submitted.

Ezzeldin, M., W. El-Dakhakhni, and L. Wiebe. 2017. "Experimental Assessment of the System-Level Seismic Performance od an Asymmetrical Reinforced Concrete Block-Wall Building with Boundary Elements." *Journal of Structural Engineering*, 143 (8): 04017063. https://doi.org/10.1061/(asce)st.1943-541x.0001790.

(FEMA). 2007. "Interim Protocols For Determining Seismic Performance Characteristics of Structural and Nonstructural Components Through Laboratory Testing." *FEMA 461.*

GOM mbH. 2016. "Inspection Basic." GOM Software

Hallinan, P., and H. Guan. 2007. "Layered finite element analysis of one-way and two-way concrete walls with openings." *Advances in Structural Engineering*, 10 (1): 55-72. https://doi.org/10.1260/136943307780150850.

Hassanli, R., M. A. ElGawady, and J. E. Mills. 2016. "Experimental Investigation of In-Plane Cyclic Response of Unbonded Posttensioned Masonry Walls." *Journal of Structural Engineering*, 142 (5): 04015171. https://doi.org/10.1061/(asce)st.1943-541x.0001450.

Hassanli, R., M. A. ElGawady, and J. E. Mills. 2017a. "In-plane flexural strength of unbonded post-tensioned concrete masonry walls." *Engineering Structures*. 136: 245-260 https://doi.org/10.1016/j.engstruct.2017.01.016.

Kim, T. H., K. M. Lee, Y. S. Chung, and H. M. Shin. 2005. "Seismic damage assessment of reinforced concrete bridge columns." *Engineering Structures*, 27 (4): 576-592. https://doi.org/10.1016/j.engstruct.2004.11.016.

Laursen, P. 2002. "Seismic analysis and design of post-tensioned concrete masonry walls." *Doctoral Dissertation*. University of Auckland.

Laursen, P. T., and J. M. Ingham. 2004. "Structural Testing of Large-Scale Posttensioned Concrete Masonry Walls." *Journal of Structural Engineering*, 130 (10). https://doi.org/10.1061/(asce)0733-9445(2004)130:10(1497).

Li, J. 2019. "Development of a Flexural Yielding Energy Dissipation Device for Controlled Rocking Masonry Walls." *MASc Thesis*. McMaster University..

Lu, X., X. Lu, H. Guan, and L. Ye. 2013. "Collapse simulation of reinforced concrete high-rise building induced by extreme earthquakes."

Earthquake Engineering and Structural Dynamics, 42 (5): 705-723. https://doi.org/10.1002/eqe.2240.

Lu, X., L. Xie, H. Guan, Y. Huang, and X. Lu. 2015. "A shear wall element for nonlinear seismic analysis of super-tall buildings using OpenSees." Finite Elements in Analysis and Design, 98: 14-25. https://doi.org/10.1016/j.finel.2015.01.006.

Mazzoni, S., F. McKenna, M. H. Scott, and G. L. Fenves. 2006. "OpenSees command language manual." Pacific Earthquake Engineering Research Center, (February).

Priestley, M., and D. Elder. 1983. "Stress-Strain Curves for Unconfined and Confined Concrete Masonry." *ACI Journal Proceedings*, 80 (3): 192-201. https://doi.org/10.14359/10834.

Rosenboom, O. A., and M. J. Kowalsky. 2004. "Reversed In-Plane Cyclic Behavior of Posttensioned Clay Brick Masonry Walls." *Journal of Structural Engineering*, 130 (5): 787-798. https://doi.org/10.1061/(asce)0733-9445(2004)130:5(787).

Shedid, M. T., W. W. El-Dakhakhni, and R. G. Drysdale. 2009. "Behavior of fully grouted reinforced concrete masonry shear walls failing in flexure: Analysis." *Engineering Structures*, 31 (9): 2032-2044. https://doi.org/10.1016/j.engstruct.2009.03.006.

Shedid, M. T., W. W. El-Dakhakhni, and R. G. Drysdale. 2011. "Seismic Response Modification Factors for Reinforced Masonry Structural Walls." *Journal of Performance of Constructed Facilities*, 25 (2): 74-86. https://doi.org/10.1061/(asce)cf.1943-5509.0000144.

TMS (The Masonry Society). (2016). "Building Code Requirements and Specification for Masonry Structures." TMS 402/602-16, Longmont, CO.

Wight, G. D. 2006. "Seismic performance of a post-tensioned concrete masonry wall system." *PhD Dissertation*. University of Auckland.

Yassin, A., M. Ezzeldin, and L. Wiebe. 2022a. "Experimental Assessment of Controlled Rocking Masonry Shear Walls without Post-tensioning." *Journal of Structural Engineering*, 148 (4): 04022018. https://doi.org/10.1061/(asce)st.1943-541x.0003307.

Yassin, A., Ezzeldin, M., and Wiebe, L. 2022b. "Experimental Assessment of Resilient Controlled Rocking Masonry Walls with Replaceable Energy Dissipation." *Journal of Structural Engineering*, (Submitted).

Chapter 6

Conclusions and Recommendations

6.1 Summary

The main objective of this dissertation was to develop an innovative controlled rocking masonry wall (CRMW) system that minimizes damage, residual drifts, repair costs, and downtime. To that end, this thesis focused on the development of controlled rocking masonry walls with energy dissipation accessible, constructed atop a steel rocking base (EASt-CRMWs). The dissertation started by developing an energy dissipation device to be used within controlled rocking systems, mounted externally to the system. In this respect, the experimental results of fourteen previously tested devices were used to develop and validate a numerical model which subsequently was used to introduce design equations for the flexural yielding energy dissipation devices to be used in future CRMW systems.

After the energy dissipation devices were developed, a numerical study was undertaken to evaluate various strategies to reduce damage and enhance the performance of CRMWs. Specifically, the study developed and validated a nonlinear finite element model along with a damage index to quantify damage based on numerical results. Both the model and the damage index were used

to investigate the impact of various design alternatives to conventional CRMW systems, such as omitting post-tensioning, using the newly developed energy dissipation device, using confinement plates, and constructing atop a steel rocking component.

To verify the results of the optimal configuration proposed in the numerical study, a series of controlled rocking masonry walls with energy dissipation accessible atop a steel rocking base (EASt-CRMWs) were constructed and tested. The experimental study contained six walls tested under quasi-static loading to investigate various parameters including the presence of confining plates, the amount of vertical reinforcement, the axial load ratio, the aspect ratio and the amount of energy dissipation included. Two detailed procedures to predict the monotonic response of the EASt-CRMW system were also presented.

Finally, an additional series of tests on two EASt-CRMWs was undertaken to investigate the replaceability of the energy dissipation devices and how the system performed with repeated tests. The numerical model and corresponding damage index from Chapter 3 were also further validated based on results from all the EASt-CRMWs tested.

6.2 Conclusions

This dissertation provided numerical and experimental results to support the development of the EASt-CRMWs toward inclusion in future seismic design codes and standards. The following conclusions highlight the main findings and contributions of the research presented in the previous chapters:

The flexural yielding energy dissipation device that was developed

displays a favorable, stable hysteretic response. The device can withstand the base shear, eliminating the need for stoppers placed at the ends of the walls. While the device was developed for use within the context of the EASt-CRMW system, it is expected that the device can also be used in other seismic force-resisting systems in future research studies. Furthermore, the design equations are expected to be a useful tool in implementing the devices in practical design applications, and the numerical model that is developed for the devices is another valuable resource for future studies on systems with the devices.

The numerical model developed for controlled rocking masonry walls, which utilizes multi-layer shell elements, proved to be highly accurate and efficient at capturing the response of various CRMW systems. The multi-layer shell elements also allowed strains to be recorded throughout the entire wall, such that a damage index could be implemented to quantify damage within CRMWs with a high degree of accuracy. The modelling techniques discussed in the current study can be adapted to simulate other seismic force-resisting systems, while the damage index proposed for CRMWs can be easily applied to conventional reinforced masonry shear walls (i.e., with fixed bases) in future studies.

The experimental results of the EASt-CRMWs tested with different configurations showed that almost all walls were capable of achieving extremely low damage to the walls themselves, with essentially all the damage concentrated in the energy dissipation devices, which were easily removed and replaced following testing. No signs of sliding were recorded at any point, indicating that the devices eliminated the need for stoppers to resist sliding shear in a CRMW system. All walls but one were able to reach

a lateral drift of 4%, with no strength degradation, residual drifts less than 0.1% and no substantial wall damage. The steel base component preserved the integrity of the rocking toe region of the wall completely. These results demonstrated the effectiveness of the system overall as a promising alternative to PT-CRMWs. With minor detailing considerations to the interface between the rocking base and the foundation, nearly identical responses can be obtained from the walls following the replacement of the energy dissipation devices. In addition to the favorable response, the construction process of the EASt-CRMW system was effective at minimizing the differences from that of ordinary reinforced masonry construction practice, while also avoiding architectural issues by eliminating the need for stoppers at the end of the walls and containing the energy dissipation devices within the footprint of the wall.

Two detailed procedures were outlined for predicting the monotonic response of the newly proposed EASt-CRMW system. The procedures rely on sectional equilibrium at the interface between the rocking base and the masonry, as well as assumed distributions of strain and neutral axis depth adapted from previous studies pertaining to PT-CRMWs. One procedure is more detailed, and subsequently more accurate; however, it requires more iterative calculations for each step of the response. The second is a simplified procedure, relying on an idealized compressive stress block to reduce the need to iterate throughout the procedure. Both procedures are expected to be valuable tools for future research related to EASt-CRMWs.

6.3 Recommendations for Future Research

The research presented in this thesis included numerical, analytical and experimental investigation of EASt-CRMWs. However, as in any innovative research project, several outstanding challenges remain unresolved and require further study. The following points present possible extensions to the research in order to continue the development of the EASt-CRMW system:

- Experimental tests under dynamic loading are still essential to represent seismic demands more closely. Dynamic testing will further study the impact effects on the wall-foundation interface, validate the damage index proposed herein and observe higher mode effects on the system.

- As demonstrated in Chapter 5, the interface between the steel rocking base and the foundation influences the performance of the wall. A more detailed investigation of the response at this location including using different materials (e.g., rubber pads), different configurations, and most importantly, dynamic impact loading is needed.

- This study looked only at the wall itself, without an investigation of the detailing requirements to connect floor diaphragms to the wall. As the displacements of the system are large, special considerations and additional research are essential to allow for the EASt-CRMW system to be incorporated into a structure.

- The testing was limited to the in-plane response of the EASt-CRMW system. As such, a system-level investigation examining multiple walls

in various directions is essential to understand the full structural response of the system, particularly how the walls respond in the out-of-plane direction. As the system is highly dependent on gravity loading, thorough investigation on the design process and overall limitations due to geometric layouts need to be evaluated.

- The numerical model considered static analysis of in-plane walls, and therefore, dynamic modelling at the system-level to investigate higher mode effects, quantify impact effects and fully account for P-Delta effects from the full structure are required in future studies.

- The developed damage index was validated using various CRMW walls. As the damage index has the potential to be used for conventional reinforced masonry shear walls, additional studies can be performed to validate the index against previous experimental work.

Appendix A

Derivation of Yield Dispalcement for Flexural Arms

The following outlines the derivation of the yield displacement equation found within Chapters 2, 3, 4 and 5 for the flexural arms. Figure A.1 Displays the boundary conditions and other relevant information for the derivation. The derivation assumes an Euler-Bournoulli beam element (and corresponding polynomial deflected shape) satisfying the differential equation:

$$\frac{d^2y}{dx^2} = \frac{Px}{EI(x)} \tag{A.0.1}$$

rearranging and integrating yields:

$$dy = \frac{-6L^3(2ax + b(L - 2x))}{Et(a - b)^2(ax + b(l - x))^2} + C_1 \tag{A.0.2}$$

as the boundary condition is fixed, at x=0, rotation (dy) = 0. This allows C_1 to be solved as:

$$C_1 = \frac{6L^4Pb}{Et(a - b)^2(bL)^2} \tag{A.0.3}$$

Integrating the expression again yields the following expression:

$$y = \frac{-6L^3P\left(\frac{bL}{ax+b(L-x)} + 2ln(ax+b(x-L))\right)}{Et(a-b)^3} + \frac{6L^4Pb}{Et(a-b)^2}x + C_2 \quad \text{(A.0.4)}$$

using the boundary conditions again, of x = 0, y = 0 (at the support) allows C_2 to be solved as:

$$C_2 = \frac{6L^3(1+2ln(bL))}{Et(a-b)^3} \quad \text{(A.0.5)}$$

Giving the final expression for displacement of:

$$y = \frac{-6L^3P\left(\frac{bL}{ax+b(L-x)} + 2ln(ax+b(x-L))\right)}{Et(a-b)^3} + \frac{6L^4Pb}{Et(a-b)^2}x + \frac{6L^3(1+2ln(bL))}{Et(a-b)^3} \quad \text{(A.0.6)}$$

which simplifies down to:

$$y = \frac{6L^3P}{Et(a-b)^3}\left(\frac{a}{b} - \frac{b}{a} - 2ln\left(\frac{b}{a}\right)\right) \quad \text{(A.0.7)}$$

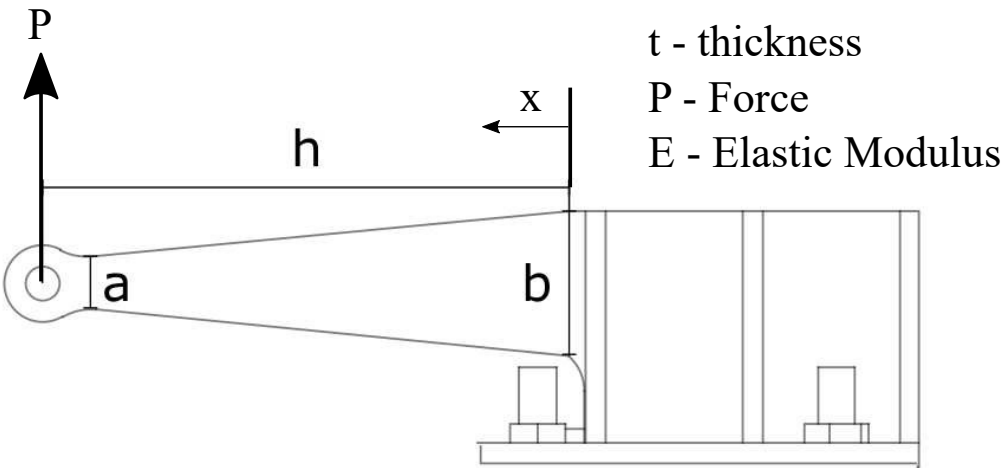

Figure A.1: Schematic for derivation of yield displacement

Appendix B

Maximum Compressive Strains in Wall Toes

Table B.1 displays the maximum strains recorded in the compressive region in each of the walls presented in Chapter 4. The strains were calculated using the vertical potentiometers V1 and V9 on the West side of the wall, and potentiometers V5 and V14 on the East side of the wall, as displayed in Figure 4.4.

Table B.1: Maximum compressive strains in walls 1-6 (Chapter 4)

Wall	Maximum Drift (%)	Maximum Compressive Strain in Masonry
Wall 1	5	0.0722
Wall 2	5	0.0685
Wall 3	4	0.0546
Wall 4	2.9	0.1240
Wall 5	5	0.0358
Wall 6	5	0.0762